

DISSERTATION
SUBMITTED TO THE
COMBINED FACULTY OF
NATURAL SCIENCES AND MATHEMATICS
OF THE
RUPERTO-CAROLA-UNIVERSITY OF HEIDELBERG,
GERMANY
FOR THE DEGREE OF
DOCTOR OF NATURAL SCIENCES

PUT FORWARD BY

M. SC. JUAN C. IBÁÑEZ-MEJÍA
BORN IN: BOGOTÁ, COLOMBIA

ORAL EXAMINATION: 19 JULY 2016

FORMATION AND EVOLUTION OF MOLECULAR
CLOUDS IN A TURBULENT INTERSTELLAR MEDIUM

REFEREES:

PROF. DR. RALF S. KLESSEN

PROF. DR. HENRIK BEUTHER

para Laura, Mauro, Cristina, Jorge y Onix

Abstract

Stars form within molecular clouds in galaxies. Therefore, understanding the formation, evolution and collapse of molecular clouds is critical for understanding galactic evolution. We present a systematic series of numerical simulations of a kiloparsec-scale size, elongated box, with sub-parsec resolution, developed to study the dynamics of molecular clouds in a galactic environment. We explore the origin of empirically observed relations such as the velocity dispersion-size relation in molecular clouds (Chapter 4), where we find that supernova explosions appear to be inefficient at driving strong turbulent motions inside the clouds, where instead gravity appears to be the dominant process driving the observed fast motions. However, supernova explosions do play an important secondary role in the mass accretion histories of molecular clouds, simultaneously enhancing and suppressing inflow of gas onto the clouds by compressing and disrupting their mass reservoirs, (Chapter 5). We complete our analysis by studying the relative importance of magnetic fields in the evolution of molecular clouds and their envelopes. We find that, although we recover magnetic field strengths comparable to the observed values, they appear unable to prevent clouds from collapsing but capable of maintaining the diffuse envelopes supported, while restricting the gas flows in the diffuse ISM along field lines (Chapter 6). Together these results strongly support a picture of molecular clouds as highly dynamical objects that collapse quickly, and shortly after begin forming stars. However the subsequent evolution of these clouds must be strongly influenced by the newborn stars to avoid star formation efficiencies higher than those observed.

Zusammenfassung

Sterne entstehen in Molekülwolken innerhalb von Galaxien. Daher ist die Entstehung, Entwicklung und der Kollaps dieser Wolken sehr wichtig für das Verständnis der Entwicklung von Galaxien. In dieser Arbeit stellen wir eine systematische Studie numerischer Simulationen einer einige Kiloparsec großen, länglichen Box mit einer Auflösung kleiner einem Parsec vor, um die Dynamic von Molekülwolken innerhalb einer Galaxie zu erforschen. Wir untersuchen die Herkunft empirisch beobachteter Beziehungen wie der Geschwindigkeitsdispersion-Größe-Beziehung in Molekülwolken (Kapitel 4). Wir stellen fest, dass Supernova-Explosionen nur wenig Einfluss auf den Zuwachs stark turbulenter Bewegungen in den Wolken haben, und stattdessen die beobachteten schnellen Bewegungen vorrangig durch Gravitation hervorgerufen werden. Allerdings spielen Supernova-Explosionen eine Doppelrolle, da sie die Massenakkretionsrate der Molekülwolken gleichzeitig verstärken und unterdrücken, indem sie deren Massenreservoirs komprimieren und stören (Kapitel 5). Wir beenden die Arbeit mit einer Analyse der relativen Bedeutung von Magnetfeldern für die Entwicklung von Molekülwolken und ihren Hülle. Wir stellen fest, dass, obwohl wir Magnetfeldstärken vergleichbar mit den beobachteten Werten erzeugen, sie sind weder in der Lage den Kollaps zu verhindern noch die Massenakkretionsrate zu beschränken (Kapitel 6). Zusammen zeichnen diese Ergebnisse ein Bild von Molekülwolken als hochdynamischen Objekten, die sich schnell entwickeln und schon kurz nach dem Kollaps Sterne bilden. Doch die spätere Entwicklung diese Wolken muss stark von den neugeborenen Sternen beeinflusst werden, da ansonsten die Sternentstehungseffizienz die Beobachtungen übertreffen würde.

List of publications

The following publications are presented in this thesis

1. **Ibáñez-Mejía, J. C.**; Mac Low, M.-M.; Klessen, R. S., Baczynski, C.: Gravity vs SN explosions and the origin of the velocity dispersion-size relations in molecular clouds, 2016, *ApJ*, in Press.

The following publications were performed in collaborations

2. Gatto, A., Walch, S., Low, M.-M. M., Naab, T., Girichidis, P., Glover, S. C. O., Wünsch, R., Klessen, R. S., Clark, P. C., Baczynski, C., Peters, T., Ostriker, J. P., **Ibáñez-Mejía, J. C.**, Haid, S. 2015, *Monthly Notices of the Royal Astronomical Society*, 449, 1057

Contents

1	Introduction	1
1.1	Motivation	1
1.2	Overview	2
2	Theory	5
2.1	Observing the Interstellar Medium	5
2.1.1	Molecular Cloud Properties	8
2.1.2	Molecular Cloud Growth	11
2.1.3	Magnetic Fields in Molecular Clouds	13
2.2	Physical Processes in the ISM	15
2.3	Heating and Cooling	16
2.3.1	Heating Processes	16
2.3.2	Cooling Processes	18
2.3.3	Thermal Equilibrium and the Two Phases of the ISM	22
2.3.4	The Third Phase of the ISM	24
2.4	Gas Self-gravity	24
2.4.1	Gravitational Instability	24
2.4.2	Virial Theorem	26
2.5	Turbulence	28
2.5.1	Kolmogorov’s Theory of Turbulence	28
2.5.2	Turbulence in Molecular Clouds	29
3	Numerical Setup	33
3.1	The Stratified Box Setup	33
3.2	The FLASH Code	33
3.3	Physical Processes	35
3.3.1	Disk Gravitational Potential	35
3.3.2	Supernova Driving	36
3.3.3	Gas Heating and Cooling	39
3.3.4	High Resolution Zoom-in Regions	40
3.3.5	Gas Self-gravity	41

3.4	General Properties of the Simulation	41
3.4.1	Initial Conditions	42
3.4.2	Grid Structure	42
3.5	New Turbulent Initial Conditions	43
4	Gravity vs SN	49
4.1	Motivation	49
4.2	Methods and Simulations	50
4.2.1	Stratified Box Simulation	50
4.2.2	Cloud Identification	50
4.3	Results	54
4.3.1	Overview	54
4.3.2	Cloud Population	57
4.3.3	Virial Balance Evolution	57
4.3.4	Evolution of the Velocity Dispersion-Radius Relation	59
4.3.5	Quantifying Cloud Evolution	62
4.3.6	Comparison With Observations	63
4.3.7	Variable Column Densities	67
4.4	Discussion	69
4.5	Summary and Conclusions	73
5	Gravity vs Accretion	75
5.1	Motivation	75
5.2	Mass and Kinetic Energy Influx	76
5.2.1	Gravitationally Driven Accretion	76
5.2.2	Turbulence Driven Accretion	77
5.2.3	Energy Inflow in Accretion Flows	77
5.2.4	Accretion Turbulence Driving Efficiency	78
5.3	Numerical Model	79
5.4	Results	81
5.4.1	Overview	81
5.4.2	Cloud Population	83
5.4.3	High Resolution Clouds	84
5.5	Interpretation and Discussion	103
5.6	Conclusions	107
6	Gravity vs Magnetic Fields	109
6.1	Motivation	109
6.2	Methods	110
6.3	Analysis tools	110
6.3.1	Magnetic Field-Density Relation	111

6.3.2	Energetics	111
6.3.3	Characteristic Velocities	111
6.3.4	Relative Orientation of Velocity and Magnetic Field . .	112
6.3.5	Histogram of Relative Orientation	112
6.3.6	Relative Orientation of Gas Flows and the Density Structure	113
6.4	Results	113
6.4.1	B-n Relation	115
6.4.2	Energetics	118
6.4.3	Alfvénic and Sonic Mach Numbers	120
6.4.4	Velocity-Magnetic Field Relative Orientation	122
6.4.5	Histogram of Relative Orientation	123
6.4.6	Density Gradient-Velocity Relative Orientation	125
6.5	Conclusions	125
7	Summary and Outlook	129
7.1	Summary	129
7.2	Outlook	131

Chapter 1

Introduction

1.1 Motivation

Star formation determines the evolution of galaxies and the development of planetary systems. Understanding the process of star formation requires the joint efforts of theory, observations and laboratory experiments. It is very difficult to have an experimental astrophysics laboratory here on Earth. Unless it is concerned with the microphysics reactions in the interstellar medium, it is impossible to recreate the conditions of the interstellar medium in a laboratory. Observations provide the basic knowledge of the gas and stars in ours and other galaxies, however our vision of the interstellar medium and the stars and planets in it, is quite limited, as light rays, almost our sole form of receiving information, have to go through a series of emission and transfer processes prior to reaching us.

Numerical simulations provide test beds for modeling and analyzing different physical processes involved in star and planet formation and galactic evolution. Furthermore, in these simulations I can “turn on and off” physical processes at will, allowing me to quantify their individual and relative influence in complex systems. Such simulations can recreate the three-dimensional structure of a system and follow its evolution for hundreds, or even thousands of megayears. These two capabilities, commonly absent in projected observations over human timescales, constitute an important element in developing our understanding of the processes involved.

Only in very special cases is the evolution of an astronomical system observed on timescales comparable to an astronomer’s lifetime. When we have been able to observe this evolution, better constraints could be inferred on the dominant physical processes of the system, and better modeling could be performed (e.g. [Reipurth & Bally, 2001](#); [De Pree et al., 2014](#); [Carrasco-](#)

González et al., 2015). It is important to also note that numerical simulations have significant limitations, not only due to resolution but also due to the methods and assumptions implemented. It is for this reason that it is important to continuously improve on the current methods, and develop new codes (Springel, 2010; Hopkins, 2014; Clarke & Whitworth, 2015), such that we can test and compare our results.

This thesis is my attempt to put together many of the physical processes influencing the dynamics of the interstellar medium, regulating the star formation process in the Galaxy. At each point in this project I try to compare the results obtained from simulations with observations in order to constrain and validate the simulations.

1.2 Overview

Understanding what controls the rate of star formation in Galaxies is fundamental for understanding galactic evolution, and for this we need to understand how molecular clouds form and how fast they evolve.

The gas in the Galaxy goes through a cycle as it condenses into dense structures capable of cooling down, quickly forming molecules, commonly known as Molecular Clouds (MC). These MCs have dynamic and exciting lives as the non-linear interaction of several physical processes contribute to their properties and determine their evolution. Resistance to the gas self-gravity comes from magnetic fields, thermal pressure, and turbulence, either coming from outside the cloud, or generated inside the cloud by stellar feedback. Understanding how MC properties evolve and what processes dominate at different stages of evolution is critical for determining how cloud formation and collapse regulates the star-formation process.

In this work I study the formation, evolution and collapse of MCs in numerical simulations of a turbulent interstellar medium (ISM). For this I implement three-dimensional, magnetohydrodynamic (MHD), numerical simulations of a section of a disk galaxy, capturing the dynamics of the gas from kiloparsec down to sub-pc scales. This allows for a self-consistent model of the formation and evolution of molecular clouds in a turbulent ISM. I focus on understanding the dynamical importance of gas self-gravity with respect to three of the commonly acknowledged processes acting against gravitational collapse in order to gain a clearer picture on how these interact to ultimately determine the fate of MCs in the Galaxy.

In Chapter 2 I begin with an introduction of the general observational properties of molecular gas and MCs, followed by a review of the dominant physical processes in the ISM, how the gas divides into multiple phases, the

main effects of turbulence, and the importance of gas self-gravity.

Chapter 3 contains a detailed explanation of all the ingredients necessary to model a multi-phase ISM in a galactic environment and details of the implementation of these ingredients in the “Stratified Box” simulations presented here. I also discuss the initial evolution of these simulations and the generation of a new set of turbulent initial conditions to be used in the following chapters.

Chapter 4 explores the properties of a cloud population formed in a turbulent environment and the interplay between gas self-gravity and supernova (SN) explosions in the clouds’ dynamics. I investigate this relative influence in the light of known observational properties of molecular clouds.

Chapter 5 studies the interplay between gravitational collapse and accretion driven turbulence due to the mass-growth process of these clouds. I compare the relative importance of the different physical processes driving accretion flows into the clouds and quantify the amount of kinetic energy deposited by this accretion onto the cloud.

Chapter 6 investigates the dynamical effects of magnetic fields on cloud morphology and environment. I compare the relative orientation of magnetic fields with respect to the density structure and velocity of the gas in the cloud and its environment, in order to understand what physical process regulates the dynamics of gas in different environments, and compare with observations of magnetic field strengths and orientation.

Finally, in Chapter 7 I present a summary of the most important results obtained in this thesis and an outlook on what can be expected in the future.

Chapter 2

Theory

2.1 Observing the Interstellar Medium

After the first detection of molecules in the interstellar medium (ISM) from emission lines of NH_3 (Cheung et al., 1968) and CO (Wilson et al., 1970), astronomers opened the doors to the vast library of information offered by the molecular gas. It quickly became clear that there are large amounts of molecular gas all around us in the Galaxy, containing a wide variety of molecules, revealing different information about the structure and history of different environments. All sky maps (Dame et al., 1987) and targeted observations of bright molecular regions (see references in Larson, 1981) were performed, revealing the the complex distribution and dynamics of molecular gas. Fig-

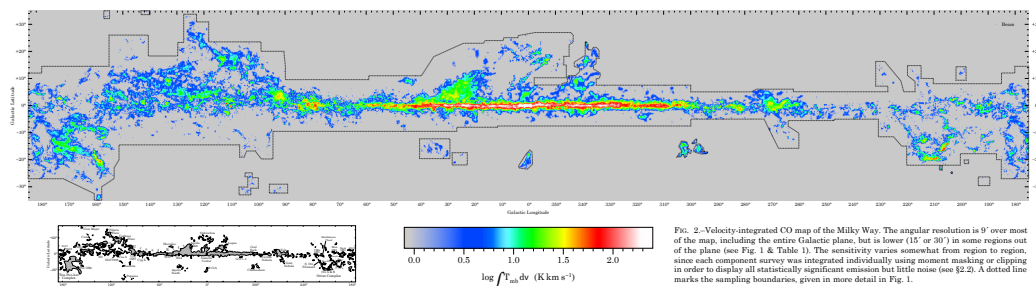


Figure 2.1: Velocity-integrated CO map of the Milky Way. The map covers the entire Galactic plane with a vertical extent up to $\pm 35^\circ$. This is Figure 2 from Dame et al. (2001).

ure 2.1 shows a composite CO survey of the entire Galaxy (Dame et al., 2001). This map displays the main features of the distribution of molecular gas in the Galaxy, showing that giant molecular clouds (GMCs) are strongly concentrated towards the plane of the galaxy. The spectral information also

available from these observations provides detailed information on the dynamics of the molecular gas in the Galaxy, revealing features such as the Galactic center and the molecular ring.

Targeted observations towards molecular clouds revealed that these clouds have internal velocity dispersions far larger than expected from thermal motions (Zuckerman & Palmer, 1974). These fast turbulent motions were first interpreted as signatures of gravitational collapse by Goldreich & Kwan (1974). However, if all the observed GMCs were collapsing with their individual free-fall times, the expected star formation rate would be one to two orders of magnitude larger than the observed (Zuckerman & Palmer, 1974). This “star formation catastrophe” has been one of the most debated problems in the context of the star formation theory, and it is still subject to debate, as we do not yet have a good explanation of how the Galactic star formation rate is regulated. Several theories have tried to reconcile this discrepancy. One of the most prominent ones, capturing most of the field’s attention between the 1970s and the late 1990s, suggests that long-lived molecular clouds, with typical lifetimes $\tau \sim 100$ Myr, supported by magnetic fields (Mestel & Spitzer, 1956; Mouschovias & Spitzer, 1976), and a star formation rate regulated by ambipolar diffusion (ion-neutral drift Shu, 1977). It is now believed that this is not the main channel for star formation to proceed, as many criticisms of this theory have emerged. Two of the most important flaws of this model are that molecular clouds are seen to be chemically young (Bergin et al., 1997; Bergin & Langer, 1997), and magnetic field measurements towards molecular clouds show field strengths somewhat too weak to prevent them from collapsing (Crutcher, 1999; Crutcher et al., 2010b; Crutcher, 2012).

Currently the most accepted theory for explaining the star formation process is gravo-turbulent star formation. In this theory, star formation is controlled by the interplay between supersonic turbulence and self-gravity (Mac Low & Klessen, 2004). Although not mentioned explicitly in its name, magnetic fields do still play an important role in the gravo-turbulent theory, as they provide one of the competing forces opposing gravitational collapse, in combination with stellar feedback and thermal pressure. The non-linear interplay between self-gravity, which tries to bring gas together, and the competing forces trying to prevent its collapse, regulate the formation and evolution of molecular clouds and thus ultimately modulate the star formation process.

Figure 2.2 shows a composite figure of data targeted towards the Taurus molecular cloud. Panel (a) shows a combination of three bands observed by the *Herschel Space Telescope* in the far infrared, revealing the complex

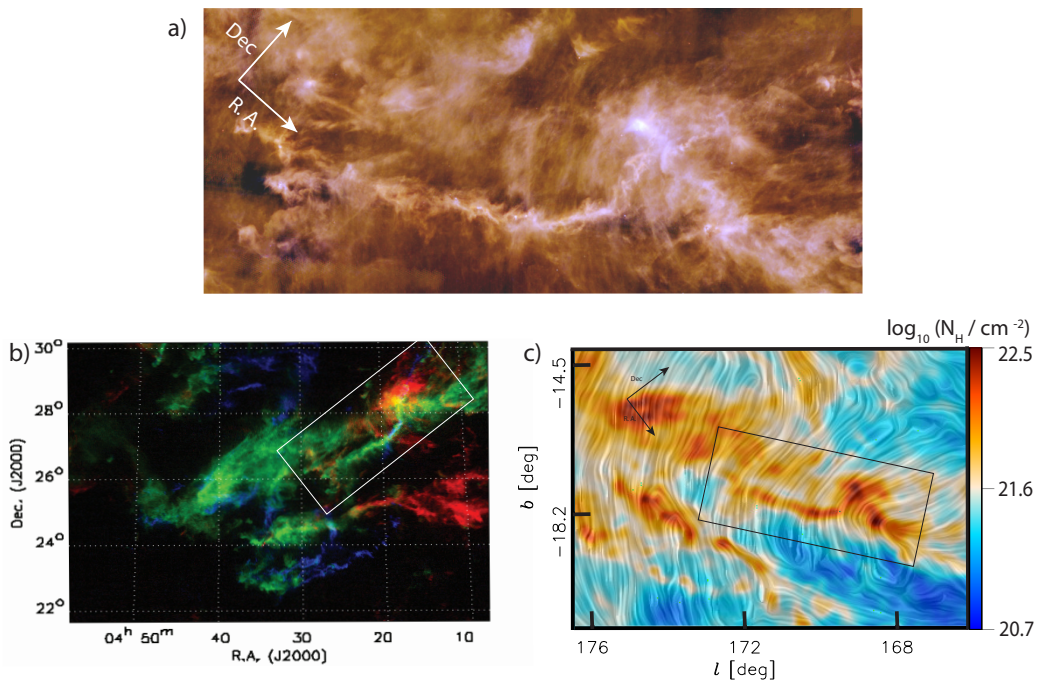


Figure 2.2: Composite figure of the Taurus molecular cloud. (a) Three-color image combining *Herschel* bands at $160 \mu\text{m}$ (blue), $250 \mu\text{m}$ (green) and $500 \mu\text{m}$ (red). (Adapted from data presented by [Palmeirim et al. 2013](#)) (b) Intensity of ^{13}CO observations divided into three velocity channels, (blue) $v < 5.5 \text{ km s}^{-1}$, (green) $5.5 \text{ km s}^{-1} < v < 7.55 \text{ km s}^{-1}$ and (red) $7.5 \text{ km s}^{-1} < v$, with the box showing the region visualized in panel (a) ([Narayanan et al., 2008](#)) (c) Color map corresponds to the column density, while the ripple mask corresponds to the magnetic field orientation inferred from dust polarization from observations with the *Planck* satellite, with the box again showing the region from panel (a). (Adapted from [Ade et al. 2016](#).)

distribution of gas in the cloud with predominantly filamentary structures at all scales. Panel (b) shows a velocity colored image of the same cloud for three velocity bands. This figure reveals the complex velocity structure of the molecular gas in the cloud, with both large-scale and small-scale velocity gradients. Finally, panel (c) shows data from [Ade et al. \(2016\)](#), with the magnetic field orientation inferred from dust polarization observations, revealing the interplay of the magnetic field orientation and the density structure of this cloud. In summary, the Taurus molecular cloud is an example of the complex interplay between the density distribution, similarly complex velocity structure, and the magnetic field determining the development of this one molecular cloud. We expect this complex interplay, including the invis-

ible action of gas self-gravity, to occur throughout the interstellar medium and to be a fundamental characteristic to be found at the interior of all molecular clouds.

2.1.1 Molecular Cloud Properties

A seminal work in the understanding of molecular cloud properties was that of [Larson \(1981\)](#), who proposed two scaling relations, also known as ‘‘Larson’s laws’’. These laws relate the volume density, size, and velocity dispersion of molecular clouds, providing a fundamental insight into cloud dynamics. They have been extensively re-examined and are now believed to have the form ([Solomon et al., 1987](#); [Heyer et al., 2009](#); [Falgarone et al., 2009](#)):

$$\sigma \propto R^{0.5} \tag{2.1}$$

$$\Sigma \propto R^{0.1}. \tag{2.2}$$

[Figure 2.3](#) shows the original plots from [Larson \(1981\)](#) corresponding to the compilation of most of the molecular line observations towards molecular clouds at the time of publication. The first equation states that clouds are structures whose velocity dispersion scales proportionally to the square root of cloud size. This is often interpreted as occurring due to a Kolmogorov-like cascade for supersonic turbulent motions ([Larson, 1981](#); [Kritsuk et al., 2013](#); [Gnedin et al., 2015](#); [Padoan et al., 2016](#)), an interpretation that results in [Chapter §4](#) call into question. The second equation suggests that clouds have constant column densities for the covered range of cloud sizes. Together these relations combine to suggest that clouds are close to being in a state of equilibrium between the gravitational attraction and turbulence, $\alpha_{vir} \approx 1$.

However later multi-tracer studies of molecular clouds gave access to denser regions and revealed previously unexplored environments within molecular clouds. [Figure 2.4](#) shows the $\sigma - R$ relation for observations of molecular clouds, massive cores, and infrared dark clouds (IRDCs) using multiple tracers. It was first noted in massive core observations by [Caselli & Myers \(1995\)](#) in ^{13}CO and C^{18}O that these structures show a shallower velocity dispersion-size relation than molecular cloud observations, with an offset in the normalization as well. Subsequent observations of CS emission in high density regions by [Plume et al. \(1997\)](#) and [Shirley et al. \(2003\)](#) also showed significant deviations from the expected Larson’s laws in both slope and normalization. Finally, IRDC observations in CS emission by [Gibson et al. \(2009\)](#); [Wu et al. \(2010\)](#), and NH_3 in emission by [Bühr et al. \(2015\)](#) consistently find shallower velocity dispersion-size relations and higher normalizations than ^{12}CO observations of molecular clouds. These deviations from the canonical scaling

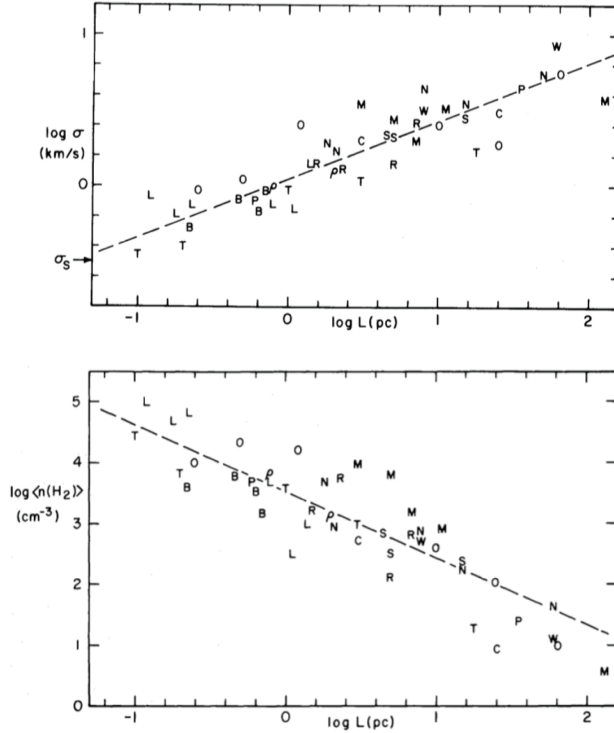


Figure 2.3: (top) three-dimensional velocity dispersion versus size for molecular clouds and condensations. (bottom) average volume density versus size for MCs and condensations. Figures 3 and 5 from [Larson \(1981\)](#).

relations led [Heyer et al. \(2009\)](#) and [Ballesteros-Paredes et al. \(2011\)](#) to suggest that multi-tracer observations give access to a broader range in column densities, in contradiction to Larson’s second law (Eq. 2.2). Including the variation of the surface density in the $\sigma - R$ relations suggests that the critical coefficients relevant to the dynamics of molecular clouds are

$$\sigma^2 \propto R\Sigma. \quad (2.3)$$

This new relation is not surprising as these are the same dependences found in the virial equation (see section 2.4.2 for more details) which relates the interplay of turbulence and self-gravity of a system, or in free-fall collapse, with the two differing only by a factor of $\sqrt{2}$ in the constant of proportionality.

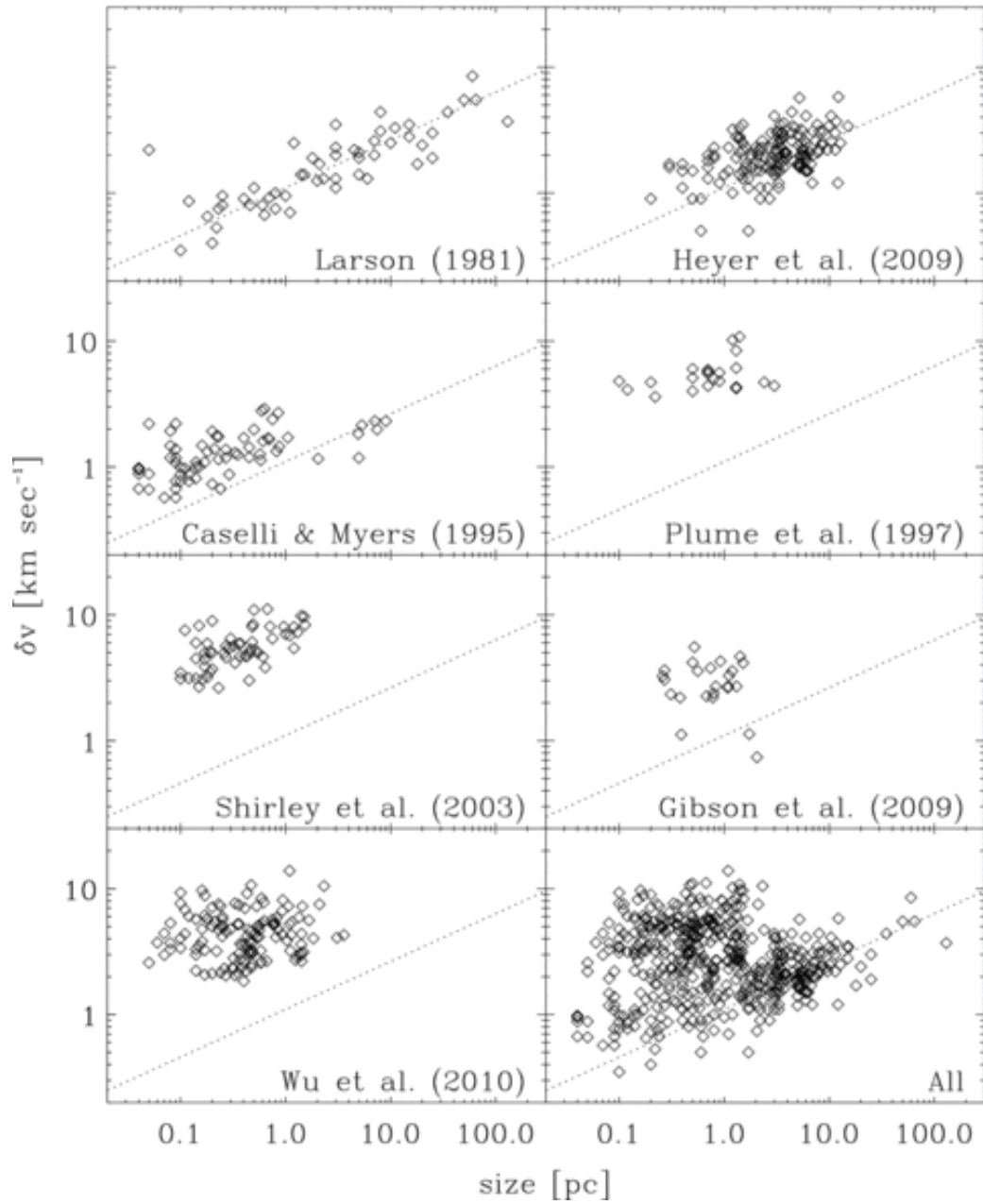


Figure 2.4: Relationship between velocity dispersion and size for molecular clouds, infrared dark clouds, and massive cores traced with a variety of molecules emitting in different density ranges. Data from Caselli & Myers (1995); Plume et al. (1997); Shirley et al. (2003); Gibson et al. (2009); Heyer et al. (2009); Wu et al. (2010). Figure 1 from Ballesteros-Paredes et al. (2011).

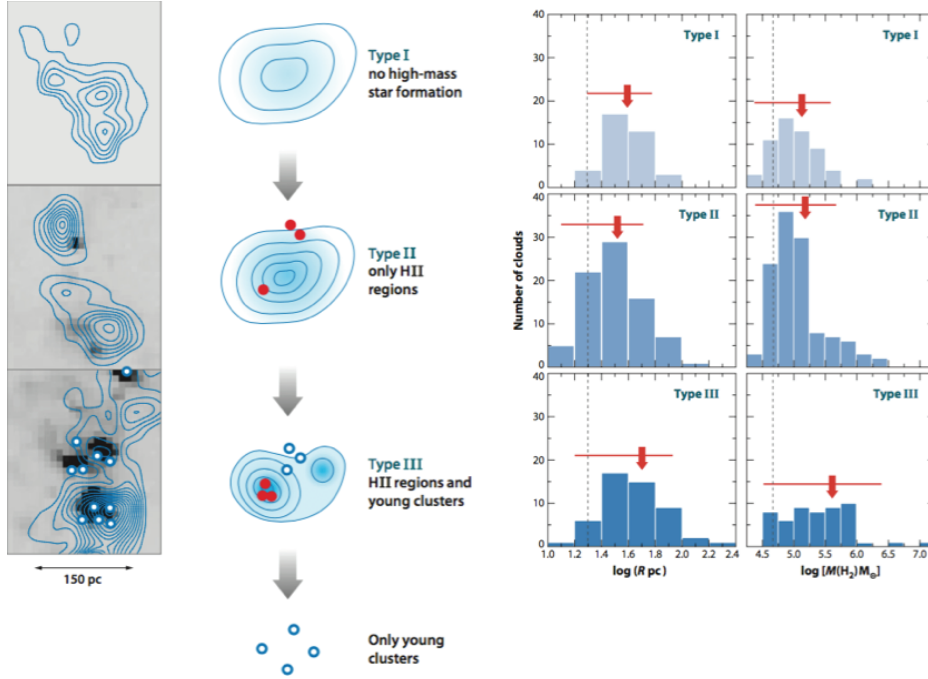


Figure 2.5: (left) Evolutionary sequence of GMCs in the LMC, type I, II and III respectively, along with a cartoon representation for each evolutionary stage. (right) histograms of the radius and mass of GMCs observed in the LMC, type I, II and III respectively. A vertical dashed line shows the completeness limit for the size (20 pc) and mass ($5 \times 10^4 M_\odot$), the red arrow indicates the average for each histogram. Figures 6 and 7 from Fukui & Kawamura (2010).

2.1.2 Molecular Cloud Growth

When discussing what controls the observed properties of molecular clouds one must consider how these clouds form, grow in mass, and how their other properties evolve. Although it is impossible to observe the growth of an individual molecular cloud in an astronomer’s lifetime, counting statistics can help us to constrain the behavior, growth, and lifetime of molecular clouds.

One of the best estimates of GMC lifetimes and growth rates is derived from observations of the Large Magellanic Cloud (LMC) by Fukui & Kawamura (2010). Using the NANTEN CO surveys (Fukui et al., 1999; Mizuno et al., 2001; Kawamura et al., 2009b), GMCs were classified into three types according to the level of observed internal star formation (Fukui et al., 1999; Yamaguchi et al., 2001). The different types were interpreted as different evo-

lutionary stages, instead of different GMC types, as shown in Figure 2.5. The first type corresponds to the starless phase, which is found to last ~ 6 Myr. This phase shows no embedded H II (ionized hydrogen) regions and is considered to have no associated massive star formation. The second type corresponds to the H II regions only phase, which lasts ~ 13 Myr. In this phase only embedded small H II regions are observed, but no exposed stellar clusters. The third and last type corresponds to the H II regions and stellar clusters phase, which lasts ~ 7 Myr. In this phase both stellar clusters and large H II regions are associated with the GMC. Finally, young clusters not associated with GMCs help constrain the time taken for stellar feedback to destroy a GMC, measured to be ~ 3 Myr. The right half of Figure 2.5 shows that as GMCs evolve from one phase to the other the mean mass of the cloud grows, suggesting that GMCs in the LMC accrete mass at an average rate of $\dot{M} \approx 5 \times 10^{-2} M_{\odot} \text{ yr}^{-1}$.

Using the PAWS survey of molecular gas in M51, (Schinnerer et al., 2013; Hughes et al., 2013; Colombo et al., 2014) a similar evolutionary sequence and growth rate of GMCs was derived by Meidt et al. (2015). Assuming GMCs form in spiral arms and then are left behind as the galaxy rotates, it is possible to quantify the age of a GMC by measuring the distance of the cloud relative to the spiral arm. Using counting statistics it is possible to quantify the lifetime and growth of GMCs depending on the number and size distribution of clouds at different distances from the spiral arm. These authors derive GMC lifetimes in the order of 25 Myr, consistent with the results of Fukui & Kawamura (2010).

Only recently have there been direct detections of gas accretion onto molecular clouds. Observations towards the Taurus molecular cloud, shown in Figure 2.2a, by Palmeirim et al. (2013), suggest a mass accretion rate along the filament of $\dot{M} \approx 27\text{--}50 M_{\odot} \text{ pc}^{-1} \text{ Myr}^{-1}$ with an infall velocity of $v_{inf} = 0.6\text{--}1 \text{ km s}^{-1}$. In their work, the authors compared the predicted and observed radial velocity gradient as a function of the distance to the spine of the filament. They found that the filament is contracting gravitationally while simultaneously accreting ambient material. Additionally, the authors analyzed the orientation of the striations in the column density map and compared them with the projected orientation of the magnetic field on the sky. They conclude that mass is accreting along the filament, flowing parallel to the magnetic field lines.

In that same year, Peretto et al. (2013) reported accretion rates onto the $M = 10^4 M_{\odot}$ IRDC SDC335. The mass accretion was observed as a self-absorption feature in the blue-shifted, optically thick, HCO^+ (1-0) molecular line. For an estimation of the formation time of the central object, the

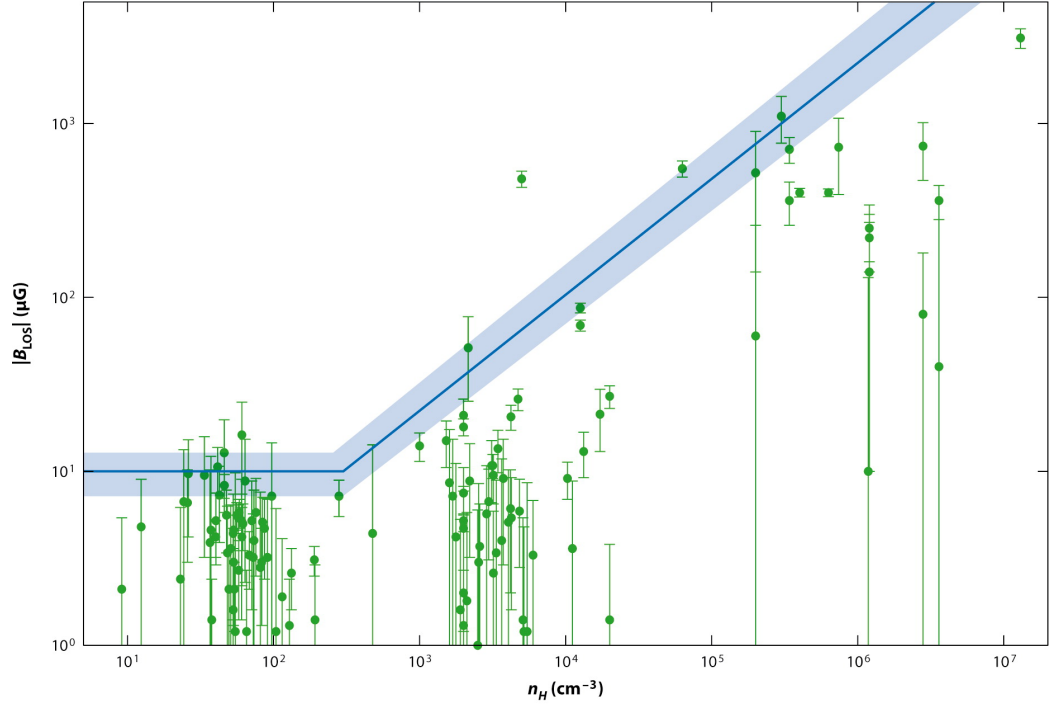
authors calculate the infall of material along the observed dense molecular filaments; the filaments have a cross section of ~ 0.30 pc, infall velocities of $v_{inf} = 0.5 - 0.9$ km s $^{-1}$, and an average volume density of $\rho_{fil} = 4 \pm 1 \times 10^4$ cm $^{-3}$. The resulting mass accretion rate onto the central object is $\dot{M} = 0.7 \pm 0.3 \times 10^{-3} M_{\odot} \text{ yr}^{-1}$. Therefore it would have taken $\sim 3 \times 10^5$ years for this core to grow to its current size, a timescale comparable to the free-fall time. In the case where the authors account not only for the infall of material along the filaments but also from the less dense material, the authors find an accretion rate of $\dot{M} = 2.5 \pm 1.0 \times 10^{-3} M_{\odot} \text{ yr}^{-1}$.

2.1.3 Magnetic Fields in Molecular Clouds

Magnetic fields are expected to play a critical role in the formation, evolution and collapse of dense molecular clouds. Our understanding and the relative importance we give magnetic fields in the dynamics of the ISM has changed significantly over the decades. From a strong-field model (Mouschovias, 1991), where molecular clouds are long lived in a state of quasi-static equilibrium, and their evolution is regulated by ambipolar diffusion, to a preferentially weak-field model (Padoan & Nordlund, 1999; Mac Low & Klessen, 2004), where the formation, evolution and collapse of molecular clouds is determined by supersonic turbulence, where magnetic fields may be dynamically important funneling the gas flows, but unable to prevent clouds from collapsing.

Direct observations of magnetic fields are necessary in order to directly test and compare these models, however, these are not only scarce, but also are somewhat complicated. One of the common methods implemented to infer the strength of magnetic fields is measuring through the Zeeman effect (Crutcher et al., 1993), which tells us the strength and direction of the field component along the line of sight, but has no information about the other orthogonal components. Another commonly used technique to explore magnetic fields corresponds to dust polarization observations. Non-spherical dust grains align with the local magnetic field producing a preferential direction for polarization of radiation. This polarization can be observed in their thermal emission, or in the absorption of background radiation. The efficiency of this alignment is very sensitive to the local temperature, torquing agents on the dust grain and the size and shape distribution of grains (Lazarian, 2007; Andersson et al., 2015). However, dust polarization depends only weakly on field strength, such that almost no information of magnetic field strength from polarization observations can be inferred.

Up to now, only three species for which we can observe Zeeman splitting in the diffuse and dense interstellar medium have been confirmed. These




 Crutcher RM. 2012.
Annu. Rev. Astron. Astrophys. 50:29–63

Figure 2.6: Zeeman measurements of the magnitude of the line of sight component of the magnetic field strength in diffuse and dense gas phases of the ISM, data is compiled in [Crutcher et al. \(2010b\)](#). The solid blue line corresponds to the upper envelope of the most probable distribution function of magnetic field strengths as a function of density, assuming the relation given by equation 2.4. Figure 6 from [Crutcher \(2012\)](#)

correspond to are H I, OH and CN, whose abundance is constrained to very narrow density ranges, where H I traces densities between $10 \text{ cm}^{-3} < n < 100 \text{ cm}^{-3}$, OH $10^3 \text{ cm}^{-3} < n < 10^4 \text{ cm}^{-3}$, and CN $10^{5.3} \text{ cm}^{-3} < n < 10^{6.3} \text{ cm}^{-3}$. Fortunately for us, these tracers are separated in density space, such that we can gain information of the magnetic field strengths in the diffuse and dense ISM as well as in very dense, collapsing cores.

Figure 2.6 shows a compilation of all the Zeeman splitting measurements reported in the literature as of 2010 (see [Crutcher et al., 2010b](#), and references therein), as well as the inferred relation of the most probable maximum value of the magnetic field strength along the line of sight as a function of density. [Crutcher et al. \(2010b\)](#) used Bayesian statistical analysis to infer the most probable distribution of all the measured Zeeman data points, also including

null measurements as upper limits. He assumed a generalized model of the form:

$$B_{max}(n, \theta) = \begin{cases} B_0, & n < n_0 \\ B_0 \left(\frac{n}{n_0}\right)^\alpha, & n > n_0 \end{cases} \quad (2.4)$$

which suggest that the upper envelope of the magnetic field strength probability distribution is constant, B_0 , below a density threshold, n_0 , and then scales proportional to the density to the power of α , above the aforementioned density threshold. In this work, [Crutcher et al. \(2010b\)](#) found $n_0 \approx 300 \text{ cm}^{-3}$, $B_0 \approx 10 \text{ } \mu\text{G}$ and $\alpha \approx 0.65$, and a flat probability distribution function for the field strength below the upper envelope. The transition from a flat field strength distribution to a power law, has been interpreted as a transition between the dominant process of the ISM as a function of density. While the diffuse gas is magnetically dominated, forcing the gas flows to be constrained along the field lines, at high density regions the gas becomes gravitationally dominated, such that gravitational contraction can compress field lines increasing the field strength proportional to the local density.

Recent observations of dust polarization with the Planck satellite is allowing us to connect the organized and turbulent component of the Galactic scale magnetic fields, along with the orientation of magnetic fields and the density structures of molecular clouds (see panel c) in [Figure 2.2](#). This multi-scale, multi-frequency dataset, combined with starlight polarization observations, Zeeman measurements of magnetic field strengths, numerical simulations of molecular cloud formation, analyzed using the newly developed techniques for the modeling of synthetic polarization observations ([Reissl et al., 2014](#)), are beginning to expose the morphology, strength and influence of magnetic fields in the dynamics of molecular clouds.

2.2 Physical Processes in the ISM

The formation and evolution of molecular clouds in the ISM is regulated by an interplay of multiple physical and chemical processes ([Mac Low & Klessen, 2004](#); [Klessen et al., 2011](#); [Klessen & Glover, 2014](#)). The non-linear combination of the gas self-gravity, always pulling gas together towards denser and denser structures, and a number of competing forces, such as turbulence, magnetic fields, thermal pressure, and stellar feedback, regulates the dynamics of the ISM and ultimately the formation of stars in galaxies.

2.3 Heating and Cooling

The interplay between the heating and cooling processes in the ISM is responsible for the development of multiple thermal phases. The heating and cooling of the gas occurs through a combination of large-scale and microscopic-scale processes influencing the physical and chemical properties of the ISM.

Large scale heating processes mostly correspond to adiabatic compression events such as cloud-cloud collisions, gas sweeping by shocks waves, or gravitational contraction. Large scale cooling occurs via adiabatic expansion, happening in the event of SN remnants interacting. We will now concentrate in the microscopic heating and cooling processes in the ISM. We will refer to the gas heating rate per unit volume by Γ and the cooling rate per unit volume squared by Λ .

2.3.1 Heating Processes

The basic action of heating at the microscopic scale occurs when an electron is knocked out of its parent ion, atom, molecule or dust grain (we will refer to them as “species” from now on, unless we refer to any one in particular). This electron then shares its energy excess with the gas through collisions. The energy excess depends on the difference between the energy of the ionizing photon and the work used to detach the electron from its parent species. Once the electron is kicked out, it is subject to collisions with the gas such that the electron’s velocity is reduced to the Maxwellian velocity distribution of the particles:

$$f(v)d^3v = \left(\frac{\mu}{2\pi k_B T}\right)^{3/2} \exp\left(-\frac{\mu v^2}{2k_B T}\right) dv_x dv_y dv_z, \quad (2.5)$$

where μ is the mean mass per particle, k_B is the Boltzmann constant, and T is the temperature, known as the kinetic temperature of the gas.

We now discuss the main heating processes in the ISM and give rough estimates of their efficiency.

Photo-ionization: In near star-forming regions, photo-ionization may be the dominant source of heating. Photo-ionization occurs when an energetic photon from a star ionizes an atom or an ion, X .



The excess energy of the ejected electron is given by the difference between the energy of the photon and the ionization potential of the parent atom or ion.

In star-forming regions, massive stars emit large numbers of energetic photons. Of particular interest are the photons with energies > 13.6 eV, as they are capable of ionizing hydrogen. Most of these photons are absorbed nearby, ionizing hydrogen in H II regions. These regions are therefore commonly used as tracers of star formation. We do not enter into much detail on the formation and evolution of H II regions, as this is out of the scope of this thesis, but we refer the reader to [Shields \(1990\)](#); [Churchwell \(2002\)](#); [Zinnecker & Yorke \(2007\)](#) for a more detailed discussion.

Some photons with energies above 13.6 eV travel far from their sources, further ionizing the warm and partially ionized diffuse gas. Photons with energies < 13.6 eV travel beyond H II regions into the neutral gas, where they ionize other elements, such as carbon, silicon, sulfur, or iron, that have ionization potentials < 13.6 eV. The electrons ejected from these ionizations contribute to gas heating and increase the electron fraction in mostly neutral regions. Given that the most energetic photons we expect in neutral regions have energies below 13.6 eV, the mean energy of the electrons released by ionization from a typical interstellar radiation field is of the order of ~ 1 eV.

Cosmic-ray heating: Another important heating source is provided by cosmic-ray ionization. Cosmic rays span a wide range of energies, from 100 MeV to more than 1 TeV. Their energy spectrum is very steep, so low energy cosmic rays are much more abundant than their high energy counterparts. Low energy cosmic rays, ~ 100 MeV, can remove an electron from an ion or a molecule, X , through a collision:



The amount of heat transferred to the gas per cosmic ray ionization depends upon the composition of the gas ([Dalgarno et al., 1999](#); [Glassgold et al., 2012](#)), but is typically around 10–20 eV. The released electron can also cause secondary ionizations, increasing the effective heating. The mean cosmic-ray ionization rate is ([Hartquist et al., 1978b,a](#); [Williams et al., 1998](#); [van der Tak & van Dishoeck, 2000](#)):

$$\zeta_H = 1 \times 10^{-17} \text{ s}^{-1}, \quad (2.8)$$

resulting in a mean heating rate by low energy CR of

$$\Gamma_{CR} = 3.2 \times 10^{-28} (\zeta_H / 10^{-17} \text{ s}^{-1}) \text{ erg s}^{-1} \quad (2.9)$$

Cosmic-rays may be an important source of heating in the interior of dense clouds where other sources of heating have been shielded by large column densities of gas and dust.

Photo-electric heating: The dominant heating process in neutral regions in the ISM is photo-electric heating from irradiating small dust grains (Bakes & Tielens, 1994). When a photon hits a dust grain, it can liberate a photo-electron with an excess of kinetic energy (Einstein, 1912). This excess is given by the difference between the energy of the incoming photon and the work function of the dust grain. The release of this photo-electron strongly depends on three parameters: 1) the strength of the interstellar radiation field, 2) the size distribution of grains and 3) the charge of the grains, as it is more difficult to free an electron from a positively charged grain than from a negatively charged grain. However, for a standard radiation field and dust distribution (Mathis et al., 1977), the average heating rate by photoelectric heating is:

$$\Gamma_{pe} = 1.3 \times 10^{-24} \varepsilon G_0 \text{ erg s}^{-1} \quad (2.10)$$

where ε is the heating efficiency and G_0 is the interstellar radiation field in Habing (1968) units. Although photo-electric heating dominates the heating rate in the atomic ISM, it is suppressed in the interior of dense clouds where the radiation field is attenuated due to the large column of gas and dust between the cloud interior and the environment (Bakes & Tielens, 1994; Wolfire et al., 2003).

Heating rate: The total heating rate corresponds to the combination of the heating processes described above. Each one of the processes depends on the gas density, species with electrons available for ejection, and an agent that can kick these electrons out. The effective heating rate is proportional to the sum of the local gas density times the individual heating process:

$$n(\Gamma_{pi} + \Gamma_{CR} + \Gamma_{pe}) = n\Gamma \quad (2.11)$$

2.3.2 Cooling Processes

Cooling of the ISM usually proceeds by the conversion of kinetic energy into radiation that can then escape the system, carrying the energy with it. This conversion of thermal energy into radiation usually occurs via collisional excitation followed by radiative decay. This process is sensitive to the composition of the gas. For the cooling to be efficient, the emitted photons

should be able to escape the system. This is possible when the decay occurs via forbidden transitions, as non-forbidden transitions will almost certainly be re-absorbed locally, thus not leaving the system and not taking energy away from the gas as a whole.

This is often understood in the context of the simple two-level system. For a detailed treatment of the two-level system we refer the reader to [Draine \(2011\)](#). Here we designate the ground state of a species (A) as i and the excited state as j . The collisional excitation rate from level i to j due to collisions with another species X , is given by:

$$\dot{n}_{ij} = n_X n_i(A) C_{ij}(T_k), \quad (2.12)$$

where $C_{ij}(T_k)$ is the collisional excitation coefficient, and T_k is the kinetic temperature.

If each collisional excitation is followed by radiative decay resulting in emission of a forbidden-line photon, the rate of energy loss is given by:

$$L_{ij} = \dot{n}_{ij} \Delta E_{ij} = n_X n_i(A) C_{ij}(T_k) \Delta E_{ij} \quad (2.13)$$

Where ΔE_{ij} is the energy defect of the decay. Cooling of gas at low temperatures is mostly due to fine structure excitation resulting from collisions with electrons. At high temperatures, cooling is mostly due to ion-ion collisions and excitation of resonant lines. In this section, we follow the analysis presented by [Dalgarno & McCray \(1972\)](#); [Sutherland & Dopita \(1993\)](#), and [Gnat & Ferland \(2012\)](#).

Line cooling: For temperatures below 10^4 K, most of the cooling in the ISM comes from fine structure excitations of ions. In these regions, most of the hydrogen is neutral but the carbon, silicon, iron, and sulfur remain ionized because of their low ionization potentials, and can be excited easily. Cooling efficiencies from collisions of these ions with electrons are ([Dalgarno & McCray, 1972](#)):

$$L_{\text{C}^+}(T) = 7.9 \times 10^{-20} T^{-1/2} \exp(-92 \text{ K}/T) \text{ erg cm}^{-3} \text{ s}^{-1}, \quad (2.14)$$

$$L_{\text{Si}^+}(T) = 1.9 \times 10^{-18} T^{-1/2} \exp(-413 \text{ K}/T) \text{ erg cm}^{-3} \text{ s}^{-1}, \quad (2.15)$$

$$L_{\text{Fe}^+}(T) = 1.1 \times 10^{-18} T^{-1/2} \times [\exp(-554 \text{ K}/T) + 1.3 \exp(961 \text{ K}/T)] \text{ erg cm}^{-3} \text{ s}^{-1}. \quad (2.16)$$

The individual contributions to the interstellar cooling by this and other ions are shown in [Figure 2.7](#). At low temperatures, cooling is mostly dominated by fine structure emission of C^+ . As temperatures rise, other species become important for cooling, like Fe^+ , O , or Si^+ .

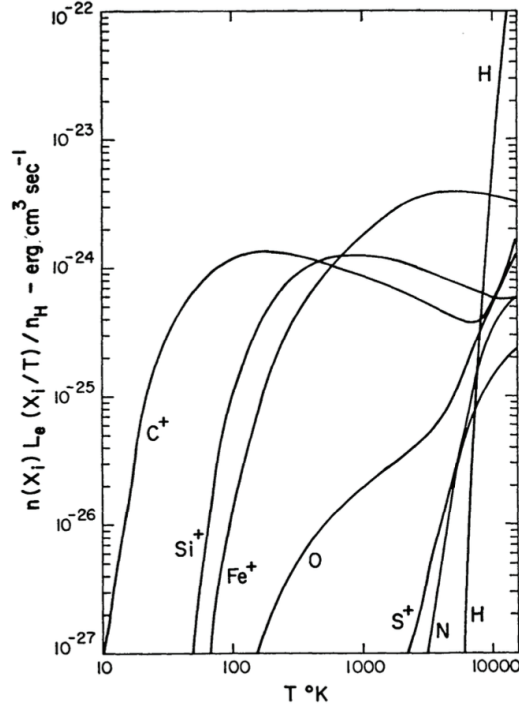


Figure 2.7: The individual contribution of the interstellar cooling ions $[n(X_i/n(H))]L_e(X_i/T)$ colliding with electrons. The contributions are computed using the relative abundance of the different ions in the Galactic ISM. Figure 1 from [Dalgarno & McCray \(1972\)](#).

For the temperature range $T < 10^4$ K, most of the cooling is mediated by collisions between ions and electrons, strongly depending on the ionization fraction of the gas. Collisions with neutral hydrogen, $L_H(X_i/T)$, can become important if the fractional ionization is low. Cooling from collisional excitation by neutral hydrogen exceeds cooling by electron collisions for regions with temperatures below ~ 70 K, and a fractional ionization of $n_e/n_H < \chi \approx 10^{-3}$. We can expect low fractional ionization inside cold, dense molecular clouds. However we also expect molecular cooling to dominate in this type of environment.

The resulting interstellar cooling function for gas below 10^4 K depends directly on the fractional ionization and the relative abundance of the ions with respect to hydrogen:

$$\Lambda(\chi, T) = \sum_i \frac{n(X_i)}{n(H)} [\chi L_e(X_i/T) + L_H(X_i/T)]. \quad (2.17)$$

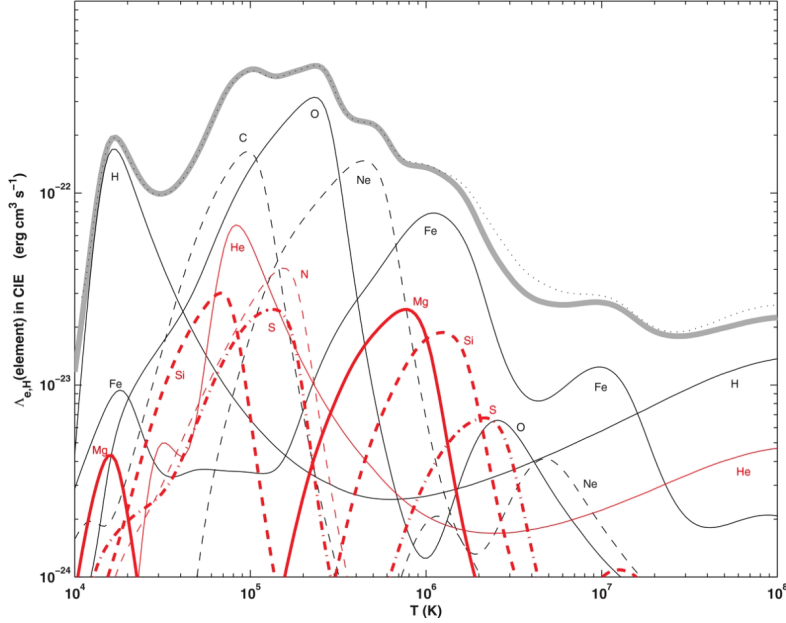


Figure 2.8: Element-by-element cooling efficiency assuming CIE for temperatures of 10^4 – 10^8 K. The total cooling efficiency contributed by all elements is shown as a thick gray line on top. Figure 3 from [Gnat & Ferland \(2012\)](#).

This cooling function is sensitive to elemental abundances, which vary at different locations in the interstellar medium and from galaxy to galaxy. Inside dense molecular clouds a large fraction of the carbon will be in the form of carbon monoxide, CO, and at even higher densities it may be mostly depleted onto dust grains. Similarly, iron is expected to be mostly depleted into dust grains, contributing less to the gas cooling than expected.

Resonant lines: For temperatures around 10^4 K, collisional excitation and ionization of hydrogen dominates. This is the origin of the steep increase in the cooling function above this temperature. At even higher temperatures, $T > 1.4 \times 10^4$ K, almost all hydrogen becomes collisionally ionized, so its cooling efficiency drops (see Figure 2.8). At this and higher temperatures, therefore, the collisional excitation of resonant metal lines completely dominates. Figure 2.8 shows the contribution of the different resonant lines for temperatures between 10^4 – 10^8 K.

The excitation of resonant lines occurs by ion-ion collisions. These regions are assumed to be in collisional ionization equilibrium (CIE), where the cooling timescales are long compared to the collisional ionization and radiative electron-ion recombination timescales.

Bremsstrahlung: free-free emission dominates the cooling of ionized gas for temperatures $T > 10^6$ K. It has a clear signature $\Lambda \propto T^{1/2}$.

Cooling rates: Note that cooling depends on collisional excitations, which is a two body process. This means that the gas cooling rate depends on the density of the cooling agents and the collisional partners, both of which can be expressed in terms of their relative abundance with respect to hydrogen.

For ions (X^i) as coolants

$$n(X^i) = n_{\text{H}} \frac{n(X^i)}{n_{\text{H}}} \quad (2.18)$$

where $n(X^i)/n_{\text{H}}$ is given by the local abundance of metals in the ISM.

For collisions with electrons the cooling rate is given by:

$$n(X^i)n_e\Lambda(T) = \chi \frac{n(X^i)}{n_{\text{H}}} n_{\text{H}}^2 \Lambda(T) \quad (2.19)$$

2.3.3 Thermal Equilibrium and the Two Phases of the ISM

Probably one of the most fundamental understandings in the study of the ISM is the description of its multi-phase thermal structure. The different phases coexist in a state of pressure and thermal equilibrium, (Field et al., 1969).

For this calculation we introduce the **net cooling L**:

$$L(n, T) = n_{\text{H}}^2 \Lambda(T) - n_{\text{H}} \Gamma. \quad (2.20)$$

The condition for thermal equilibrium is that the heating and the cooling balance each other, such that $L(n, T) = 0$.

Knowing the cooling rate as a function of temperature as shown in Figure 2.7, and knowing the heating rate of the diffuse heating processes (Eq. 2.11), we can calculate the equilibrium temperature as a function of the density. Given that pressure, temperature, and density are related via the equation of state, we can translate this equilibrium temperature-density relation into a pressure-density relation.

Figure 2.9 shows the interplay between the different ingredients for the development of thermal equilibrium and the two phases of the ISM. Panel (a) shows the behavior of the thermal pressure equilibrium curve, $L(n, T) = 0$,

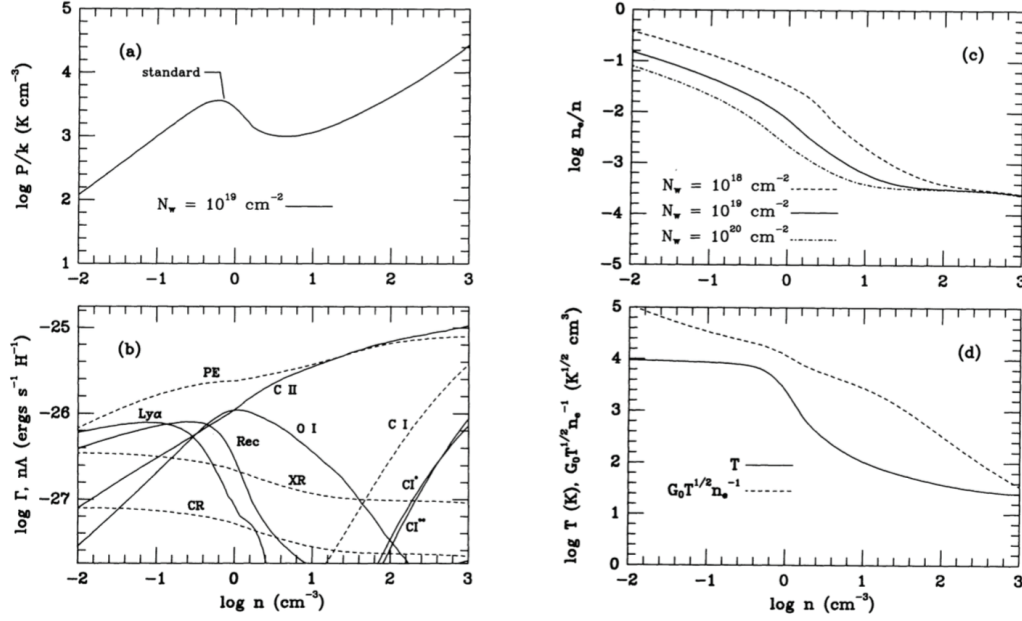


Figure 2.9: (a) Thermal pressure equilibrium curve as a function of hydrogen density, n . (b) Heating (dashed lines) and cooling (solid lines) rate per hydrogen nuclei as a function of hydrogen density for typical warm interstellar medium conditions. (c) fractional ionization as a function of hydrogen density. (d) gas temperature (solid) and ionization parameter (dashed) as a function of hydrogen density. Figure 3 from [Wolfire et al. \(1995\)](#).

as a function of density. On this curve, gas is *thermally stable* if the pressure increase for increasing density,

$$\frac{d \log(P)}{d \log(n)} > 0.$$

This condition is fulfilled for number densities $n < 0.4 \text{ cm}^{-3}$ and $n > 10 \text{ cm}^{-3}$. The gas is *thermally unstable* if the pressure decreases with increasing density,

$$\frac{d \log(P)}{d \log(n)} < 0.$$

In this case, the density will continue moving rising until it reaches a stable equilibrium again.

Another important aspect of Figure 2.9(a) is that there is only a narrow range of pressures, $900 \text{ K cm}^{-3} < P/k < 3600 \text{ K cm}^{-3}$, in which the gas can be at two densities and remain in pressure equilibrium. Pressures below $P/k = 900 \text{ K cm}^{-3}$ will contain only warm, diffuse gas, while pressures above $P/k = 3600 \text{ K cm}^{-3}$ will contain only cold, dense gas.

2.3.4 The Third Phase of the ISM

Shortly after the two-phase ISM model was suggested, large amounts of hot, diffuse gas were observed in the disk of the Galaxy (Jenkins & Meloy, 1974; York, 1974; Burstein et al., 1977). This observations led McKee & Ostriker (1977) to suggest that there is a third phase of the ISM that is regulated by SN explosions. Following the work by Cox & Smith (1974), who studied the expansion of SN explosions in a uniform medium and the generation of a hot network of tunnels, McKee & Ostriker (1977) studied the expansion of SN explosions in an inhomogeneous medium. They found that SN explosions generate large volumes of diffuse, hot gas that remains hot for timescales longer than the time between SN explosions, so that they can maintain the heating of this component of the ISM.

This hot gas is not actually in thermal equilibrium, as its net cooling is not zero, but its cooling timescale of up to tens of Gyr is sufficiently long such that the gas can be treated as being in approximate thermal equilibrium. This phase permeates the galactic midplane, in a series of interconnected tunnels, carved into the warm and cold medium, and extend up to 5–10 kpc filling the Galactic halo. It is also in rough pressure equilibrium with the other two phases, so that it serves as a confining environment to the other two phases of the ISM, maintaining the delicate stability of the multi-phase ISM.

2.4 Gas Self-gravity

Gravity is a multi-scale force responsible for pulling gas together, forcing it into self-gravitating structures such as stars, molecular clouds and galaxies. Self-gravity has to continuously battle against a number of competing forces such as thermal pressure, turbulence, magnetic fields, radiation pressure, and shear. The interplay between gravity and the competing forces is what determines the formation and collapse of structure and ultimately leads to the formation of stars.

2.4.1 Gravitational Instability

The response of a region of interstellar gas to gravitational compression was analyzed by Jeans (1902). Let us consider the simplest case of a stationary, inviscid, unmagnetized, homogeneous gas; the evolution of this gas is determined by the conservation of mass and momentum, supplemented by the

definition of the gravitational potential:

$$\frac{\partial \rho}{\partial t} + \nabla \cdot (\rho \vec{v}) = 0, \quad (2.21)$$

$$\frac{\partial \vec{v}}{\partial t} + (\vec{v} \cdot \nabla) \vec{v} = -\frac{1}{\rho} \nabla p + \nabla \phi, \quad (2.22)$$

$$\nabla^2 \phi = 4\pi G \rho. \quad (2.23)$$

Supposing the gas is in equilibrium, in a steady-state solution such that $v = v_0 = 0$, $\rho = \rho_0$, $p = p_0$ and $\phi = \phi_0$, the system does not evolve in time. Therefore $\partial p_0 / \partial t = \partial \rho_0 / \partial t = \partial v_0 / \partial t = \partial \phi_0 / \partial t = 0$, satisfying the hydrostatic equations

$$\nabla p_0 = -\rho_0 \nabla \phi_0 \quad (2.24)$$

$$\nabla^2 \phi_0 = 4\pi G \rho_0. \quad (2.25)$$

Performing a linear perturbation analysis, we examine the response of the system to small perturbations:

$$\vec{v} = \vec{v}_0 + \delta \vec{v}, \quad (2.26)$$

$$\rho = \rho_0 + \delta \rho, \quad (2.27)$$

$$p = p_0 + \delta p, \quad (2.28)$$

$$\phi = \phi_0 + \delta \phi. \quad (2.29)$$

We also assume that the perturbation evolution timescale is much shorter than the heat conduction timescale, fulfilling the adiabatic condition, so that the pressure and density perturbations are linearly related by

$$\delta p = c_s^2 \delta \rho. \quad (2.30)$$

Because the perturbations are small, (e.g., $\delta \rho \ll \rho$) we can drop the quadratic terms in the perturbed quantities in equations 2.21, 2.22, 2.23, simplifying the continuity equation to

$$\frac{\partial \delta \rho}{\partial t} + \rho_0 \nabla \cdot \delta \vec{v} = 0, \quad (2.31)$$

the conservation of momentum to

$$\rho_0 \frac{\partial \delta \vec{v}}{\partial t} = -c_s^2 \nabla \delta \rho - \rho_0 \nabla \delta \phi, \quad (2.32)$$

and for the Poisson equation, subtracting the hydrostatic equilibrium solution 2.25, we obtain:

$$\nabla^2 \delta \phi = 4\pi G \delta \rho. \quad (2.33)$$

We are then left with three equations for three perturbed quantities $\delta\rho$, δv and $\delta\phi$. We can decompose the growth of the perturbations into Fourier components. Assuming a solution of the form:

$$\rho = \rho_0 e^{i(\vec{k}\cdot\vec{x}-\omega t)}, \quad (2.34)$$

$$\vec{v} = \vec{v}_0 e^{i(\vec{k}\cdot\vec{x}-\omega t)}, \quad (2.35)$$

$$\phi = \phi_0 e^{i(\vec{k}\cdot\vec{x}-\omega t)}, \quad (2.36)$$

$$(2.37)$$

we obtain:

$$-\omega\delta\rho + \rho_0\vec{k} \cdot \delta\vec{v} = 0, \quad (2.38)$$

$$-\rho_0\omega\delta\vec{v} = -c_s^2\vec{k}\delta\rho - \rho_0\vec{k}\delta\phi, \quad (2.39)$$

$$-k^2\delta\phi = 4\pi G\delta\rho. \quad (2.40)$$

Combining these three equations, we find a dispersion relation for the perturbations

$$\omega^2 = c_s^2(k^2 - k_j^2), \quad (2.41)$$

where

$$k_j^2 = \frac{4\phi G\rho_0}{c_s^2}. \quad (2.42)$$

When $k < k_j$, ω is imaginary, which according to equation 2.34 means that the system is unstable. This corresponds to the case where the enhanced self-gravity from the compression cannot be smoothed away by the thermal pressure and the system collapses. We can calculate the amount of unstable mass contained within a sphere of uniform density ρ_0 and radius λ_j , also known as the Jeans length, related to the critical wavenumber via $\lambda_j = 2\pi/k_j$.

$$M_j = \frac{4}{3}\pi\rho_0\lambda_j^3 \quad (2.43)$$

This mass is known as the Jeans mass, which we can express in terms of the gas density and sound speed:

$$M_j = \frac{4}{3}\pi^{5/2}c_s^{3/2}\frac{1}{\rho_0^{1/2}}. \quad (2.44)$$

2.4.2 Virial Theorem

It is not always possible to determine the evolution of a system explicitly from the differential equations of self-gravitating MHD. However, knowing

the global conditions of a system, we can estimate its general state. [Clausius \(1870\)](#) suggested that the total kinetic energy of a system is related to an integral on the force at its surface. This has come to be known as the *virial theorem*.

The virial theorem in its simplest form, neglecting surface terms and other forms of energy, states that the temporal average of the kinetic energy of a system is related to the total gravitational potential energy of that system (The fully developed theorem is derived by [McKee & Zweibel 1992](#)). This theorem is currently one of our best tools to determine the masses of molecular clouds ([Larson, 1981](#); [Myers & Goodman, 1988](#); [Dib et al., 2007](#)), and also their dynamical state ([Kauffmann et al., 2013](#)).

A detailed derivation of the virial theorem for magnetized molecular clouds was first performed by [Chandrasekhar & Fermi \(1953b\)](#), where they assumed a Lagrangian reference frame, and concentrated on the role of magnetic fields in these clouds. Later, the new derivation of the virial theorem performed by [McKee & Zweibel \(1992\)](#) also included the effects of turbulence on the cloud, including both internal turbulence and ram pressure on the surface.

The virial theorem is evaluated from the second derivative of the inertia tensor I_L , here given in symbolic form as

$$\frac{1}{2}\ddot{I}_L = 2(K - K_S) + M + W \quad (2.45)$$

where K is the total kinetic energy, due to both thermal and gas motions, K_S is the external surface pressure, M is the magnetic energy and W is the gravitational energy. Most applications of the virial theorem assume that the cloud is in a state of virial equilibrium, such that the variation of the inertia tensor is small enough to be neglected, $\ddot{I}_L = 0$.

This approximation allows us to express the relative importance of the kinetic energy of a cloud, with respect to its gravitational energy ([Bertoldi & McKee, 1992](#))

$$\alpha_{vir} = a \frac{2K}{|W|} = \frac{5\sigma^2 R}{GM} \quad (2.46)$$

where the dimensionless parameter a is of order unity, and contains the information of the shape and distribution of mass in the cloud, $a = 1$ for a spherical, uniform-density cloud, and σ is the velocity dispersion of the cloud.

The simplified version of the virial parameter given by equation 2.46 is often used to calculate the virial mass of a cloud, given the one-dimensional velocity dispersion evaluated from the Gaussian profile of an observed line. If the mass of the cloud is known, the virial parameter can be used to estimate

the dynamical state of that cloud. If $\alpha_{vir} < 1$, the gravitational energy exceeds the kinetic energy, suggesting that the cloud will collapse. On the other hand if $\alpha_{vir} > 1$, the kinetic energy dominates over the gravitational energy, so the cloud must be bound by external pressure or it will expand due to this excess of kinetic energy.

2.5 Turbulence

2.5.1 Kolmogorov's Theory of Turbulence

Turbulence is ubiquitous in most fluids. In a turbulent flow, fluid velocities vary chaotically in space and time, so a deterministic theory of their dynamics cannot be developed. Turbulence is characterized by correlated fluctuations of the density, pressure and velocity of the gas, leading to an enhanced mixing and to an energy cascade down to the dissipation scale. The flow of a fluid is determined by the Navier-Stokes equation

$$\frac{\partial \vec{v}}{\partial t} + (\vec{v} \cdot \nabla) \vec{v} = -\frac{1}{\rho} \nabla p + \nu \nabla^2 \vec{v} + \vec{F}, \quad (2.47)$$

where \vec{v} is the velocity field, ρ the local density, p the pressure, ν is the kinematic viscosity, and \vec{F} contains other external forces affecting the fluid, such as gravity or magnetic fields. Turbulence is expected to arise if the non-linear advection term, $(\vec{v} \cdot \nabla) \vec{v}$, is much larger than the dissipation term, $\nu \nabla^2 \vec{v}$. The ratio of these two terms in dimensional form is known as the Reynolds number

$$Re = \frac{\ell v}{\nu}. \quad (2.48)$$

where ℓ and v are the characteristic length-scale and velocity of the system.

The pioneering work by [Kolmogorov \(1941\)](#) suggested that turbulence can be thought of as a collection of eddies of different sizes. Energy is fed into the system on the largest scales L , and energy is transferred downwards to the smaller scales through a turbulent cascade at a constant rate ϵ . At each stage of the cascade all the information we have is the characteristic size and velocity of the eddies ℓ , and v . The rate at which energy is transferred is ([Kolmogorov, 1941](#))

$$\epsilon \sim \frac{v^3}{\ell}, \quad (2.49)$$

so the characteristic velocity

$$v \sim (\epsilon \ell)^{1/3}. \quad (2.50)$$

If we now express this in terms of wavenumber $k \sim 1/\ell$, we obtain the relation

$$v \sim \epsilon^{1/3} k^{-1/3}, \quad (2.51)$$

so the kinetic energy $\propto v^2$ associated with an eddy of a particular size is

$$v^2 \sim \epsilon^{2/3} k^{-2/3}. \quad (2.52)$$

Finally, we can determine the energy spectrum for such a turbulent cascade knowing that $E(k)dk \sim v^2$, which we can approximate as $E(k)k$, to obtain:

$$E(k) \sim \epsilon^{2/3} k^{-5/3}. \quad (2.53)$$

Eventually, the eddies will reach a small enough size that their product with the velocity will be comparable to the kinematic viscosity,

$$\ell_d v_d \sim \nu, \quad (2.54)$$

which is the scale where the energy in these eddies will dissipate. The range of sizes between the injection scale L and the dissipation scale, ℓ_d is known as the inertial range.

Kolmogorov's theory is valid for incompressible turbulence only, the most commonly encountered case in terrestrial application. However turbulence in molecular clouds is mostly supersonic and highly compressible.

2.5.2 Turbulence in Molecular Clouds

Within molecular clouds, Reynolds numbers are expected to be of the order of 10^{5-10} , so turbulence is always expected to arise if there are available energy sources to drive it. Furthermore, turbulence in molecular clouds is commonly supersonic, with Mach numbers of $M = 5 - 50$. Turbulence seems to play a key role in the formation of structure, both preventing and promoting gravitational collapse.

The energy source for interstellar turbulence remains an open question. [Mac Low & Klessen \(2004\)](#) suggested that SN explosions are the main candidate driving turbulence in the diffuse ISM. They inject their energy at scales of the order of 100 pc, setting a turbulent cascade down to the dissipation scale. [Klessen & Hennebelle \(2010\)](#), on the other hand, suggested that accretion processes at different scales carry enough energy to drive the observed turbulent motions in the ISM.

It is observed that MCs have fast, non-thermal, turbulent motions fed at the largest scales of the system ([Ossenkopf & Mac Low, 2002](#); [Brunt,](#)

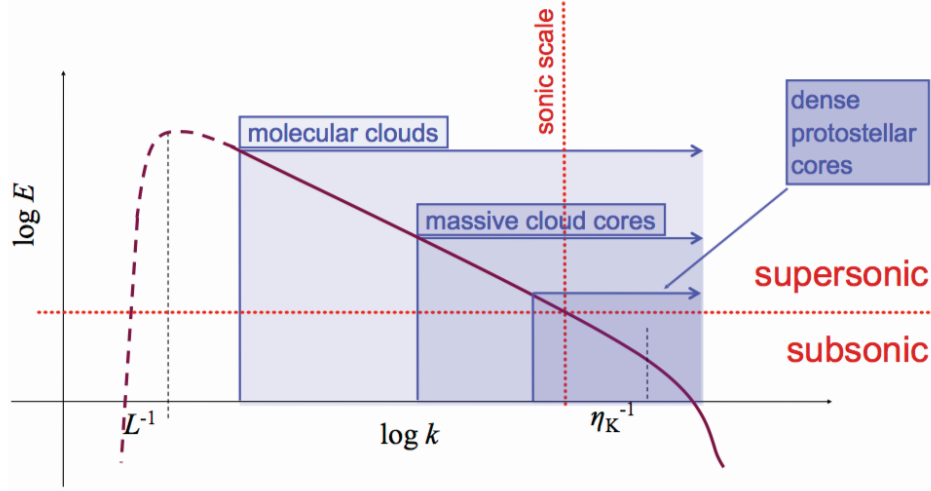


Figure 2.10: Cartoon representation of the turbulent energy spectrum as a function of wavenumber. In the background, various molecular cloud structures are shown and their relevant scales compared to the turbulent energy spectrum. Turbulence is injected at large scales, L , larger than the cloud scale and dissipates at small scales η_K . Figure 2 from [Klessen \(2011\)](#).

2003; [Brunt et al., 2009](#)). Figure 2.10 shows a cartoon representation of the turbulent energy spectrum in relation with the structure of molecular clouds. Turbulence permeates every scale of molecular clouds and appears to play a key role influencing the density distribution at all scales. For example, in a typical cloud with an average density of 100 cm^{-3} , having internal, non-thermal, turbulent motions with a Mach number of $M = 30$, the densities reached in shock compressed regions can be as high as 10^5 cm^{-3} . These density contrasts may be sufficiently large to trigger gravitational instability leading to gravitational collapse.

Turbulence can also provide support against gravitational collapse. We now follow the micro-turbulence approximation developed by [Chandrasekhar \(1951\)](#) and [Von Weizsäcker \(1951a,b\)](#) due to its intuitive power, showing how turbulence can provide a global support against collapse. This approximation assumes that the energy containing scale of the turbulence is much smaller than the characteristic scale of the system. In that case, the approximation can be made that the turbulence can be represented by an isotropic pressure term, so we can add its contribution to the thermal pressure, to find an effective sound speed

$$c_{s,eff}^2 = c_s^2 + \frac{\langle v^2 \rangle}{3} \quad (2.55)$$

where $\langle v^2 \rangle$ is the mean value of the three-dimensional velocity dispersion. For an isothermal gas, the post-shock density scales proportional to the Mach number squared:

$$\rho_s = \rho M^2. \quad (2.56)$$

If we follow [Mac Low & Klessen \(2004\)](#) in substituting these two relations into Equation [2.44](#) for the Jeans mass, we find

$$M_j = \left(\frac{\pi}{G} \right)^{3/2} \rho_s^{-1/2} c_{s,eff}^3 \propto \langle v^2 \rangle. \quad (2.57)$$

This relation implies that turbulence can provide a global support against perturbations by increasing the Jeans mass, proportional to the turbulent energy, even though it can locally cause collapse by increasing the local density.

Chapter 3

Numerical Setup

3.1 The Stratified Box Setup

This thesis presents results from a series of numerical simulations of a vertical column of the stratified ISM, including the effects of supernova explosions, magnetic fields, self-gravity, and the other physical effects detailed in the previous chapter. The vertically extended grid allows simulation of both the distribution of the gas at the midplane, as well as its vertical stratification and the circulation of gas at high altitudes. These models represent an extension of the models developed by [Joung & Mac Low \(2006\)](#); [Joung et al. \(2009\)](#), and [Hill et al. \(2012\)](#). The updates presented in this thesis, including gas self-gravity and focused adaptive mesh refinement (AMR), allow me to reach up to thirty times higher resolution than the cited previous work, down to a resolution of $\Delta x = 0.06$ pc.

Figure 3.1, shows a cartoon representation of the simulated volume with respect to a disk galaxy. The elongated box contains parts of the galactic disk and the vertical stratification up to the galactic halo. The simulations presented in the following chapters, ran from tens to hundreds of megayears reaching resolutions from a few parsecs down to a few hundredths of a parsec. In the following sections we explain the different physical ingredients and some general properties of the simulations.

3.2 The FLASH Code

We use FLASH v4.0 and v4.2 to run the simulations presented in this work. FLASH is a modular, Eulerian, three-dimensional, astrophysical, MHD, adaptive mesh refinement (AMR) code on a Cartesian grid ([Fryxell et al., 2000](#)). The code solves the ideal MHD equations, including gas self-gravity and the

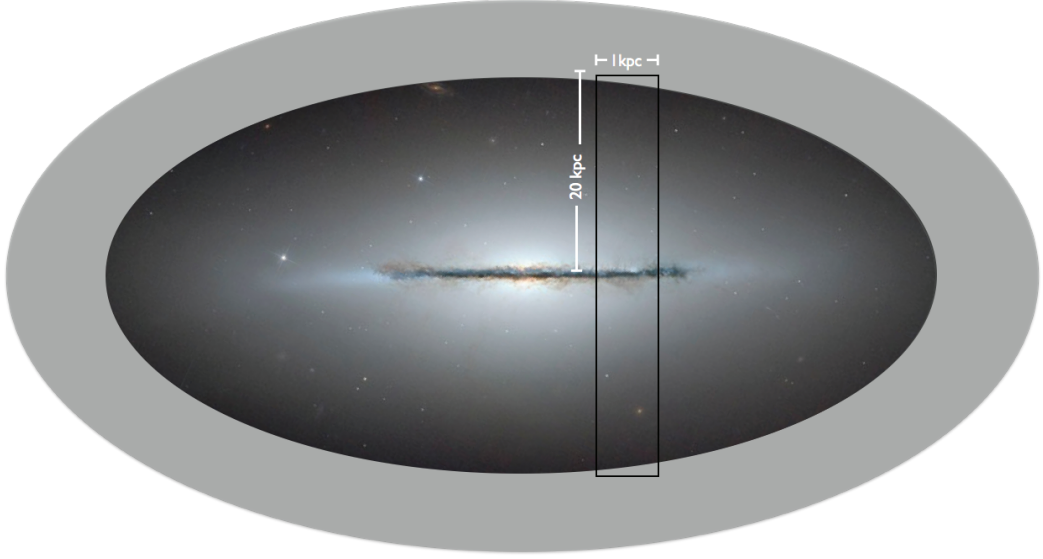


Figure 3.1: Cartoon representation of the position and relative size of the simulated volume with respect to the Galaxy. The simulated volume is an elongated box with 1 kpc^2 footprint and 40 kpc height. The Galactic plane cuts the box in half, and the vertical elongation captures the gas stratification and the circulation of gas at high altitudes up to $\pm 20 \text{ kpc}$. The total density in the box is scaled to match the surface density in the Solar neighbourhood.

injection of discrete bursts of energy, here given in conservative form:

$$\frac{\partial}{\partial t} \rho + \nabla \cdot (\rho \mathbf{v}) = 0 \quad (3.1)$$

$$\frac{\partial}{\partial t} \mathbf{v} + (\mathbf{v} \cdot \nabla) \mathbf{v} = -\frac{1}{\rho} \nabla P + \nabla \left(\frac{\mathbf{B}\mathbf{B}}{4\pi} - \frac{|\mathbf{B}^2|}{8\pi} + g(z) - \nabla \phi \right) \quad (3.2)$$

$$\frac{\partial}{\partial t} E + \nabla \cdot \left[\left(E + \frac{|\mathbf{B}^2|}{8\pi} + P \right) \mathbf{v} - \frac{(\mathbf{B} \cdot \mathbf{v}) \mathbf{B}}{4\pi} \right] = n\Gamma - n^2 \Lambda + S(x, t) \quad (3.3)$$

$$\frac{\partial}{\partial t} \mathbf{B} - \nabla \times (\mathbf{v} \times \mathbf{B}) = 0 \quad (3.4)$$

Equations (3.1) to (3.4) express conservation of mass, momentum, and energy, and the induction of the magnetic field. The magnetic field \mathbf{B} is additionally constrained to fulfil $\nabla \cdot \mathbf{B} = 0$ everywhere at all times. The thermal

pressure is related to the gas temperature, T , and density, n , via an equation of state $P = \gamma \mu n k_B T$ with an adiabatic index of $\gamma = 5/3$, where k_B is the Boltzmann constant. We use a mean mass per particle of $\mu = 1.3017 m_H$ throughout the paper, assuming neutral, atomic gas with a helium fraction of 0.097 and the remaining 0.3% in metals.

Gravity is included using two terms representing a static background mass distribution provided by old stars and dark matter with a gravitational acceleration $g(z)$ (see discussion in §3.3.1), and a gravitational potential ϕ derived from the gas density field, constantly updated to account for the dynamical evolution of the gas. The gas gravitational potential is derived from the Poisson equation,

$$\nabla^2 \phi = 4\pi G \rho. \quad (3.5)$$

The energy density is given by

$$E = \frac{\rho \mathbf{v}^2}{2} + \frac{P}{\gamma - 1} + \frac{|\mathbf{B}^2|}{8\pi}. \quad (3.6)$$

The diffuse heating $n\Gamma$ corresponds to the photoelectric heating rate. The cooling rate $n^2\Lambda$ is given by the interstellar cooling curve, as described in more detail in §2.3.2. Equation 3.3 accounts for the localized injection of discrete SN explosions $S(x, t)$, discussed in detail in §3.3.2.

3.3 Physical Processes

3.3.1 Disk Gravitational Potential

A static disk gravitational potential represents the gravitational influence of dark matter and a thin and thick stellar disk. Near the midplane, the potential follows a modified version of the solar neighborhood potential derived by Kuijken & Gilmore (1989), transitioning to the inner halo potential of Dehnen & Binney (1998) at $|z| \geq 4$ kpc. At heights above $|z| \geq 7.5$ kpc, there is a smooth transition to an outer halo potential (Navarro et al., 1996, hereafter NFW). The resulting gravitational acceleration has the form:

$$g(z) = \begin{cases} -\frac{a_1 z}{\sqrt{z^2 + z_0^2}} - a_2 z + a_3 z |z|, & |z| \leq 7.5 \text{ kpc} \\ -\frac{4}{3} G \pi \rho_h z, & |z| > 7.5 \text{ kpc}, \end{cases} \quad (3.7)$$

where $a_1 = 1.42 \times 10^{-3} \text{ kpc Myr}^{-2}$, $a_2 = 5.49 \times 10^{-4} \text{ Myr}^{-2}$, $a_3 = 5 \times 10^{-5} \text{ kpc}^{-1} \text{ Myr}^{-2}$ and $z_0 = 0.18 \text{ kpc}$. The NFW potential, ρ_h , is given by

$$\rho_h = \rho_s \frac{r_s}{|z|} \left(1 + \frac{|z|}{r_s} \right)^{-2}, \quad (3.8)$$

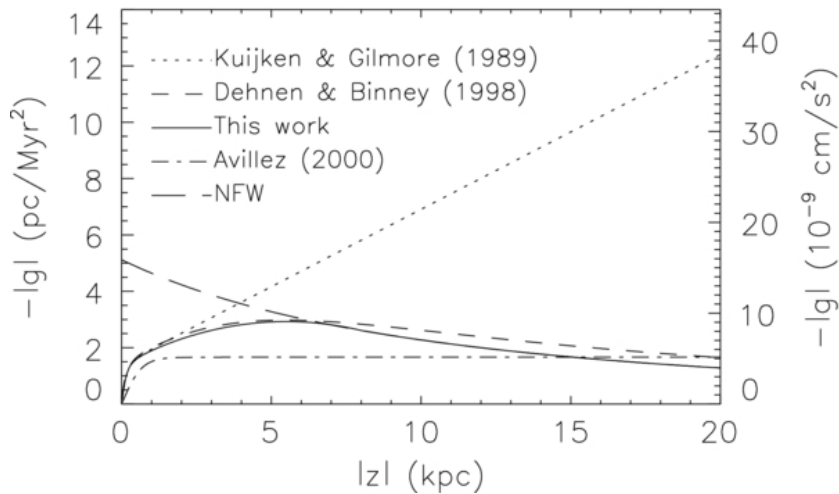


Figure 3.2: Static gravitational acceleration used in the stratified box simulation (solid line). It is a combination of the [Kuijken & Gilmore \(1989\)](#), dotted line) acceleration function near the midplane, with a transition to the [Dehnen & Binney \(1998\)](#), dashed line) function at intermediate scales and finally an NFW (long dashed line) halo above $|z| = 8$ kpc. Figure taken from [Hill et al. \(2012\)](#).

with a scale radius of $r_s = 20$ kpc and a core density of $\rho_s = 9.2053 \times 10^{-25} \text{ g cm}^{-3}$. Figure 3.2 shows the vertical variation of the gravitational acceleration for the static potential.

3.3.2 Supernova Driving

Discrete SN explosions drive the turbulence in the simulation. SN rates are normalized to the galactic SN rate ([Tammann et al., 1994](#)): Type Ia and core-collapse SN have rates of 6.58 and $27.4 \text{ Myr}^{-1} \text{ kpc}^{-2}$, respectively. The positions of the SN explosions are randomly located in the simulation box with a peak in the probability distribution at the midplane and an exponential decay proportional to the distance to the midplane. Vertical scale heights of 90 pc for core-collapse SNe and 325 pc for Type Ia SNe are assumed ([Heiles, 1987](#); [Miller & Scalo, 1979](#)).

SN explosions are treated as in [Joung & Mac Low \(2006\)](#) and [Hill et al. \(2012\)](#): where 10^{51} erg of energy ([McKee & Ostriker, 1977](#); [Ostriker & McKee, 1988](#)) are injected into a sphere enclosing $60 M_\odot$ centered at the SN position. The mass in this sphere is not added by the SN routine, but gathered from the existing mass in the simulation. For this reason, injected SN explosions have varying radius, depending on the local density. No gas mass is added

to the SN explosion, although the density is redistributed uniformly through the sphere. Clustered SNe are taken into account by assuming that 60% of the core-collapse SN are correlated in space and time, forming superbubbles. The remaining 40% of core-collapse SN correspond to runaway stars.

The total SN rate as a function of time has a constant increase in the number of SN explosions during the first 50 Myr of evolution as the SB population is built (see §3.3.2). After the initial 50 Myr the SN rate reaches a plateau and the rate at which SN explosions occur in the box is relatively constant, because superbubble particles are disappearing as fast as they are being created.

Figure 3.3 shows the locations of the Type Ia and runaway core-collapse SNe that have exploded over 250 Myr of evolution. SNe are concentrated in the midplane and equally distributed across it.

Superbubbles

In order to model the dynamics of moving OB associations, we include superbubble particles, containing a population of massive stars that will explode as SN. The SN population in a superbubble is drawn from a random distribution $dN_{\text{SB}} \propto n_*^{-2} dn_*$ with lower and upper cut offs of $n_{*,\text{min}} = 7$ SN and $n_{*,\text{max}} = 40$ SN (McKee & Williams, 1997). Superbubbles have a fixed lifetime of $t_{\text{SB}} = 40$ Myr. SN explosions in a superbubble are uniformly distributed over the superbubble lifetime, $t_{\text{SB}}/dN_{\text{SB}}$.

Superbubble formation sites are drawn from a random distribution with a peak in the probability at the midplane and an exponential decay in the vertical direction, with a vertical scale height of 90 pc, equal to that of core-collapse SNe. Superbubble particles are treated as massless particles moving in a straight line with a velocity given by the bulk velocity of the gas at their birthplace. We impose a maximum velocity of 20 km s^{-1} for these particles. The dynamics of these particles are not affected by any force as they represent only a container for SNs, providing the position information when a SN blows up. Most of the superbubble population moves at the maximum velocity allowed, 20 km s^{-1} . This is because we are drawing random locations for the superbubble particles locations, and there is a higher probability that particles are formed in fast moving, hot-diffuse gas, due to its large volume filling fraction, see §3.5. A more realistic distribution of superbubble locations initially associated with dense gas would yield a lower velocity dispersion for the superbubble particles. However, we expect the superbubbles to expand even faster than 20 km s^{-1} , and thus for this to have little practical consequence.

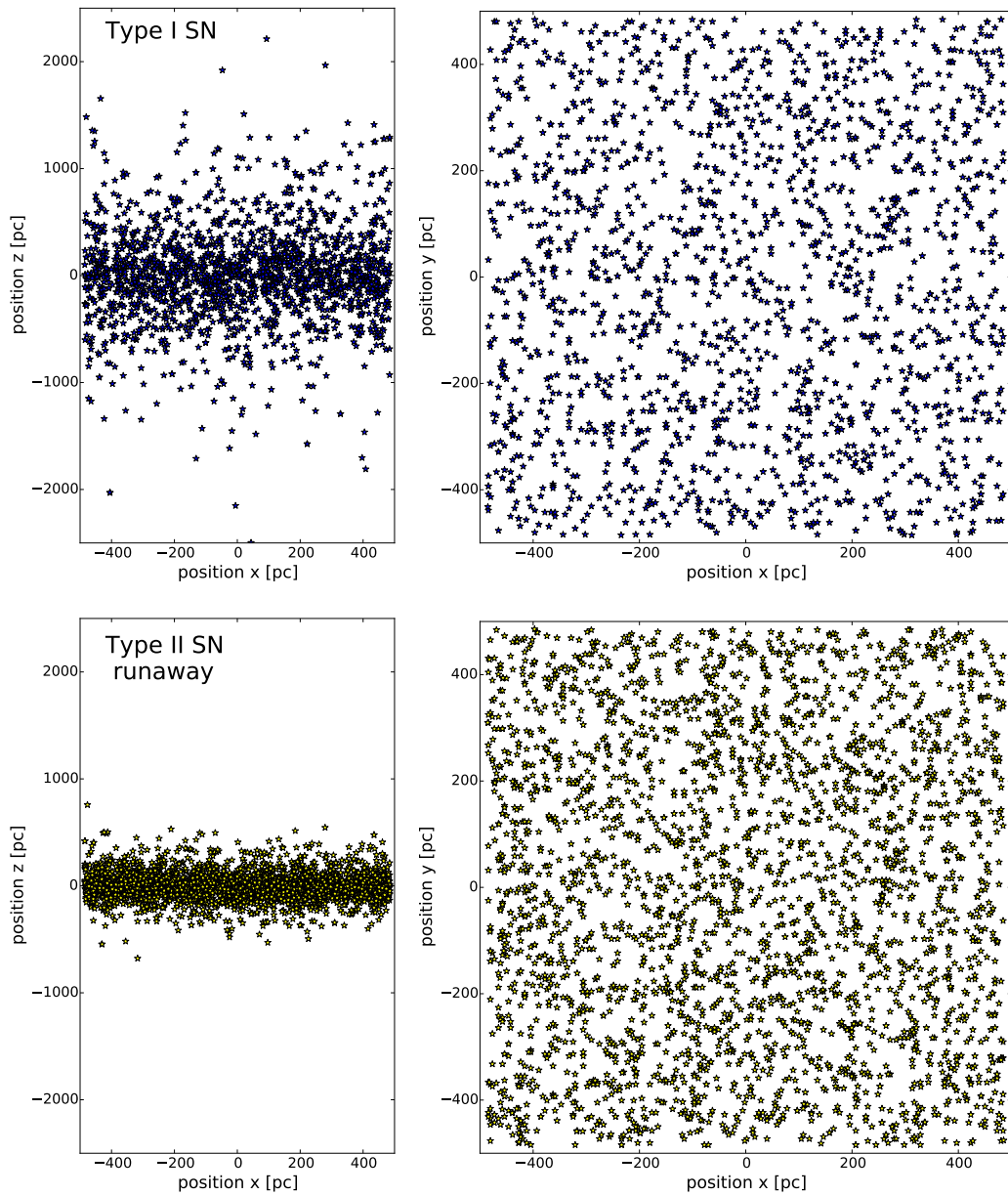


Figure 3.3: (left) Vertical and (right) horizontal projection of the spatial distribution of (top) Type Ia and (bottom) core-collapse runaway SN explosions after 250 Myr of evolution, during which 1,878 Type Ia and 3,065 core-collapse, runaway SNe have exploded. Type Ia SNe have a much larger scale height and explode at altitudes of up to 2.5 kpc, while core-collapse runaway stars are more concentrated near the midplane.

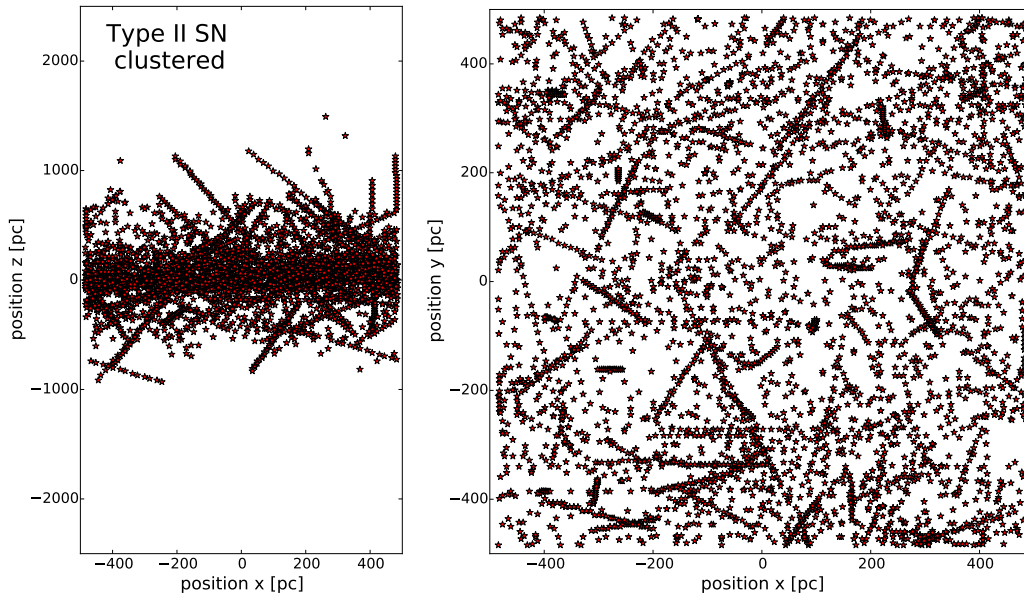


Figure 3.4: Spatial distribution of the 4,137 clustered SN explosions in the simulation during 250 Myr of evolution. The footprint of superbubble particles is clearly seen as straight tracks of SN events in both the (left) vertical distribution and (right) horizontal distribution.

3.3.3 Gas Heating and Cooling

In order to develop a multi-phase ISM, gas is allowed to be heated by a diffuse heating rate, Γ and cooled down, Λ , by the dominant cooling mechanisms depending on the local temperature and density of the gas (see section §2.3.2). Radiative cooling is included corresponding to an optically thin plasma with Solar metallicity. The cooling curve is a piecewise power law, as shown in Figure 3.5, with an electron fraction of $n_e/n_H = 10^{-2}$ for temperatures $T \leq 2 \times 10^4$ K. At higher temperatures, cooling is dominated by resonant lines (Sutherland & Dopita, 1993; Gnat & Ferland, 2012).

The diffuse heating rate is dominated by photoelectric heating from irradiated dust grains (Bakes & Tielens, 1994). It is the dominant heating process in the cold and warm neutral phase of the ISM (Wolfire et al., 1995), but is completely inefficient for collisionally ionized gas. The photoelectric heating rate Γ_{pe} is therefore only applied to gas with temperatures $T < 2 \times 10^4$ K, and is given by:

$$\Gamma_{pe} = \epsilon G_0 e^{\frac{|z|}{h_{pe}}} \text{ erg s}^{-1}, \quad (3.9)$$

where we use a heating efficiency of $\epsilon = 0.05$ and an incident interstellar far-

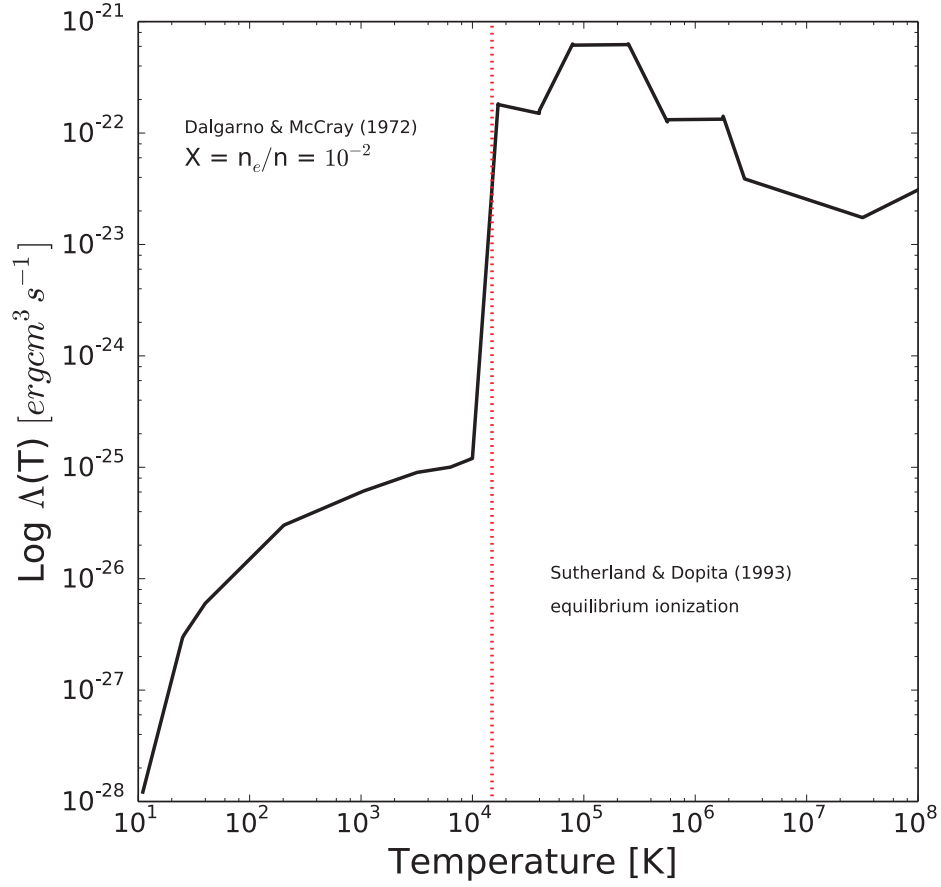


Figure 3.5: Piecewise power law reconstruction of the interstellar cooling curve as a function of temperature implemented in the simulations of the stratified box. For temperatures below 1.5×10^4 K, the cooling function follows [Dalgarno & McCray \(1972\)](#) with an electron fraction of $n_e/n_H = 10^{-2}$. For temperatures above 1.5×10^4 K, the cooling curve follows [Sutherland & Dopita \(1993\)](#), assuming collisional ionization equilibrium.

ultraviolet radiation field normalized to the ([Habing, 1968](#)) field $G_0 = 1.7$ ([Draine, 1978](#)). The heating rate decays exponentially, with a vertical scale height of $h_{pe} = 300$ pc, and is assumed to be independent of the gas density.

3.3.4 High Resolution Zoom-in Regions

An extra layer of AMR is included in the simulation so that we can zoom-in on specific targets in the simulation. This module allows for the mesh inside the box to be refined up to the maximum specified refinement level, while maintaining the grid structure outside the box static.

The module has two algorithms to increase grid refinement. In the first, the resolution inside the volume is uniformly increased up to the maximum desired resolution and is held static at this high resolution level. In the second, the grid is only refined in Jeans unstable regions when self-gravity is included, or regions that would formally be Jeans unstable in the absence of self-gravity. In either case, the [Truelove et al. \(1997\)](#) criterion of four zones per Jeans length is maintained until the maximum resolution is reached.

The interface between the resolution in the zoom-in box and its environment has a buffer zone of a few cells, with a characteristic step-by-step refinement. This ensures that the turbulent gas motions coming from outside the box, are systematically refined as they enter the zoom-in region.

3.3.5 Gas Self-gravity

Most of the simulations presented here include gas self-gravity. The computation of the gas self-gravity is performed by computing the potential $\phi(\vec{x})$ for an arbitrary distribution of gas $\rho(\vec{x})$ at each timestep. We use the hybrid solver available in FLASH originally written by [Ricker \(2008\)](#). This solver combines a multigrid solver with a parallel fast Fourier transform (FFT) on the root grid, which improves performance and accuracy for AMR grids and scales well up to thousands of processors.

The multigrid solver solves the Poisson equation first at the coarsest grid level and then climbs up the grid hierarchy to higher resolution grids, computing the residual between the source term and the approximated solution of the coarse grid. Of particular importance is the communication of the coarse and fine grid solutions between refinement levels, where interpolation or prolongation of the solution is implemented depending on the boundary. The implementation of the parallel FFT allows for faster computation of the solution, as some of the coarse grid level calculations can now be omitted, as they are communicated between processors.

Computation of the gas potential is the most computationally demanding physical process in these simulations. This process represents the limiting factor for the resolution levels and physical times reached in the simulations presented in this thesis.

3.4 General Properties of the Simulation

In this section we discuss some of the general properties of the evolution of the simulation before self-gravity is turned on, and the development of the new turbulent initial conditions.

3.4.1 Initial Conditions

The initial density distribution corresponds to a quasi-hydrostatic equilibrium between the pull of the static galactic gravitational potential and the stratification of an isothermal gas given by

$$\rho_i(z) = \rho_i(0) \exp \left[\left(-a_1(z^2 + a_3^2)^{1/2} - \frac{1}{2}a_2z^2 + \frac{1}{3}a_4z^3 + a_1a_3 \right) \frac{\rho_i(0)}{p_i(0)} \right], \quad (3.10)$$

where the density, temperature and pressure of the ISM at the midplane are $\rho_i(0) = 3.41 \times 10^{-24} \text{ g cm}^{-3}$, $T_i = 1.15 \times 10^4 \text{ K}$, and $p_i(0) = 2.48 \times 10^{-12} \text{ g cm}^{-1} \text{ s}^{-2}$.

A uniform intergalactic medium representative of a hot outer halo with density $\rho_g = 1.72 \times 10^{-31} \text{ g cm}^{-3}$, temperature $T_g = 1.15 \times 10^6 \text{ K}$ and pressure $p_g = 1.28 \times 10^{-17} \text{ g cm}^{-1} \text{ s}^{-2}$ is included above the altitude where the ISM density derived from hydrostatic equilibrium $\rho_i(z) < \rho_g$. The total amount of gas in the simulation is scaled so that the projected surface density along the vertical direction \hat{z} is equal to the gas surface density in the solar neighborhood $\Sigma_\odot = 13.7 M_\odot$ (van der Kruit, 1988; Olling & Merrifield, 2001).

We include a uniform magnetic field along the horizontal \hat{x} direction that decays exponentially with height, so that the initial plasma beta parameter $\beta = p/8\pi B^2 = 2.5$ everywhere. The magnetic field naturally evolves in the simulation being advected by the fluid and getting tangled thanks to the SN turbulence, maintained by the small scale turbulent dynamo induced by SN turbulence (Balsara et al., 2004; Meinecke et al., 2014). However, Hill et al. (2012) showed that because no galactic shear is included in our simulations the large-scale dynamo necessary to maintain a strong, organized magnetic field is not active. Thus our simulations tend to underestimate the effects of organized large scale magnetic fields.

3.4.2 Grid Structure

The background stratified box has a volume of $1 \times 1 \times 40 \text{ kpc}^3$, and uses nested mesh refinement, concentrating high resolution in the midplane and lower resolution at altitudes. Resolution decreases by a factor of two at $|z| = 300 \text{ pc}$, 1 kpc , 3 kpc and 10 kpc . This refinement is static and does not react to strong shocks or gas condensations, which ensures that the bulk of the computational effort is concentrated on following the gas dynamics at the midplane.

We set the initial maximum resolution at the midplane to be 3.80 pc and run the simulation for 200 Myr , including SN feedback, heating and

cooling, static galactic gravitational potential, and magnetic fields, but no gas self-gravity. This establishes the turbulence in the midplane as well as the vertical profile of the galactic fountain at modest computational cost. We then refine the grid step by step in order to develop a full turbulent cascade in our highest resolution regions. At 200 Myr we increase the refinement level by one everywhere in the box, bringing the maximum resolution in the midplane to 1.90 pc. We then continue running the simulation for 20 Myr. At 220 Myr we include a first zoom-in box covering the entire midplane in the horizontal directions and up to ± 50 pc in the vertical direction, increasing the maximum available refinement by one extra level to 0.95 pc. However, we only refine within this box on structures that would formally be Jeans unstable if self-gravity were included. We run for 10 Myr longer, to make sure that we populate the small scales in the turbulent cascade at the new resolution. Finally, at $t = 230$ Myr, we turn on gas self-gravity for the first time, and follow the subsequent evolution for 10 Myr. We analyze the evolution of the cloud population during this run in chapter 4.

However, we also want to study the formation and evolution of individual clouds in more detail. To do this we first identify clouds of interest as follows. At $t = 230$ Myr, we increase the maximum refinement level in the zoom-in box by one further level and then run without self-gravity for 10 Myr. At this point, $t = 240$ Myr, we identify cloud structures that have recently formed in the turbulent ISM and target them for high-resolution, zoom-in re-simulations, starting again at $t = 230$ Myr. When a cloud is targeted for re-simulation, a high-resolution zoom-in box is constrained to a region of 100 pc^3 around the target cloud, while the rest of the environment is forced back to the nested grid refinement with 1.9 pc resolution at the midplane and correspondingly lower resolution at higher altitudes.

We selected three clouds as targets for the high resolution, zoom-in simulations. We set the maximum resolution in the box around the first cloud to 0.47 pc, around the second cloud to 0.12 pc, and around the third cloud to 0.06 pc. We do not include sink particles in any of these simulations but instead merely allow gas to collapse to the grid scale without any additional refinement.

3.5 New Turbulent Initial Conditions

During the initial 230 Myr period without self-gravity, SN explosions inject energy to the ISM, providing the velocity dispersion necessary to support the midplane against collapse, and establishing the disk scale height (Ostriker et al., 2010; Shetty & Ostriker, 2012; Hill et al., 2012; Kim et al., 2013;

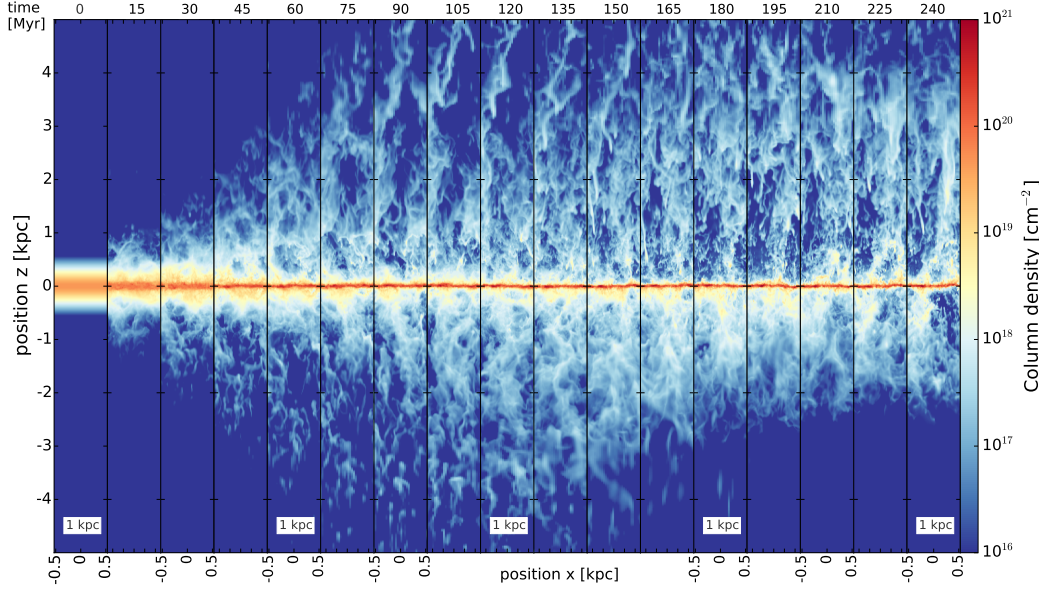


Figure 3.6: Time development of the stratified box during 240 Myr of evolution, in snapshots of 15 Myr. Each panel shows the column density projected parallel to the galactic midplane for the inner $1 \text{ kpc} \times 10 \text{ kpc}$ of the simulated volume. SN explosions drive a wind and establish the vertical circulation of the gas in a Galactic fountain. Condensation of gas at altitude is observed, as it falls back to the midplane.

Walch et al., 2015; Girichidis et al., 2016a,b), as well as forming dense clouds in converging flows. SN explosions occur during the entire evolution of the simulation. Initially, clouds form from convergent flows driven by SN blast waves. During the non-self-gravitating evolution of the simulation, clouds can not gravitationally collapse but are continuously shocked and deformed by larger flows. The gas forms a multiphase ISM with most of the mass concentrated in the cold, dense phase while most of the volume is filled by warm and hot diffuse gas, as shown by Hill et al. (2012).

Figure 3.6 shows the evolution of the gas above and below the midplane during the full 240 Myr that we have run non-self-gravitating models. The last three slices show the improved resolution stages. Although we start with idealized initial conditions, SN explosions rapidly perturb this state, heating and compressing the gas, driving fast shocks, ejecting gas to high altitudes, and developing the multiphase structure at the midplane. The continuing injection of SN energy maintains the stratification and the circulation of gas at altitude while simultaneously driving large amounts of turbulence in the

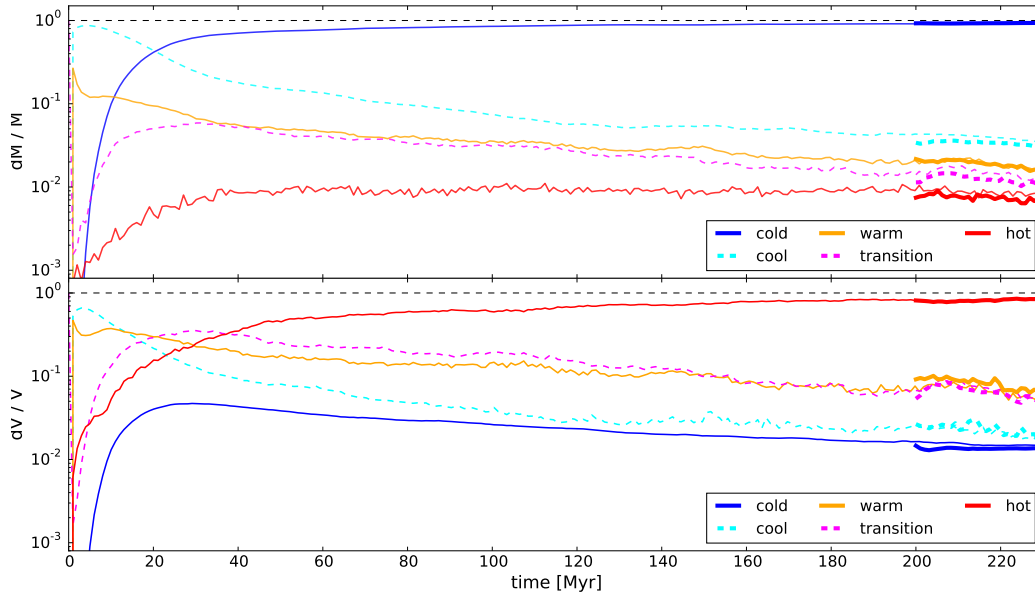


Figure 3.7: Time evolution of the mass fraction (top) and volume filling fraction (bottom) of different phases of the ISM for the innermost ± 500 pc of the simulation. Thin lines correspond to the 3.8 pc resolution simulations, thick lines to the 1.9 pc resolution simulations. Gas phases are defined by the gas temperature as cold, $T < 200$ K, cool, $200 \text{ K} < T < 5000$ K, warm, $5000 \text{ K} < T < 10000$ K, transition, $10000 \text{ K} < T < 12000$ K, and hot, $T > 12000$ K.

midplane. The large scale atmospheric oscillations predicted by [Cox & Smith \(1974\)](#) are seen here, as in [Hill et al. \(2012\)](#).

The evolution of the gas is dominated by a combination of infall towards the midplane, due to the galactic gravitational potential, and discrete injection of energy by SN explosions providing the vertical support against collapse. Thanks to the interplay between these two processes in addition to the heating and cooling processes, the gas naturally separates into multiple phases. Figure 3.7 shows the mass fraction and volume filling fraction of the different gas phases as a function of time. While most of the mass is concentrated in the cold phase, up to $\sim 92\%$, it fills only a small fraction of the volume. With the complete opposite behavior the hot phase fills most of the volume while it contains only the lowest amount of mass. During the first ~ 50 Myr of evolution, the mass and volume filling fractions of the different phases change drastically with time as the idealized initial conditions are perturbed. The gas quickly forgets this ideal stage and adjusts to a new dynamical equilibrium regulated by the interplay between the physi-

cal processes included in the simulation. After ~ 120 Myr of evolution, the simulation has reached a dynamical equilibrium, where the amount of mass and the volume of the different phases does not change much over time.

These simulations over-produce cold gas compared to the observed cold gas fraction in the Galaxy, $\sim 50\%$ [Ferriere \(2001\)](#). We strongly suspect this is because we don't include self-consistent star formation or SNe and other stellar feedback correlated with the density, therefore allowing a lot of mass to concentrate in long-lived clouds ([Gatto et al., 2015](#)).

Figure 3.8 shows the distribution of the gas density and temperature, along with the thermal, magnetic and kinetic energy densities along two lines of sight, parallel and perpendicular to the midplane. It is clear that most of the gas is concentrated around the midplane, distributed in cold, dense filamentary clouds embedded in warm envelopes and surrounded by hot-diffuse gas. The density of the gas quickly decreases with altitude while the temperature increases, giving rise to the hot, diffuse halo of the Galaxy. The midplane has a roughly constant pressure, with variations above and below the mean in expanding SN remnants or rapidly cooling gas. The thermal pressure is largest in and around the midplane, as this is the region with the deepest gravitational potential and highest SN rate. Thanks to the vertical stratification, hot buoyant bubbles rise ([de Avillez & Mac Low, 2002](#)) as can be seen from the Figure. The magnetic energy density is small compared to the other energy densities almost everywhere. However as the magnetic field is frozen to the gas, it concentrates in dense structures where it can reach magnitudes comparable to both the thermal and kinetic energy densities. Finally the Kinetic energy density is seen to have large fluctuations on short length scales. Fast turbulent motions driven by SN explosions produce a series of shocks, generating the distribution of kinetic energy seen at the midplane. These fast turbulent motions are stronger near the midplane, where they provide support against collapse.

After 230 Myr of evolution, we are left with a vertically stratified, structured, multi-phase ISM, which constitutes a useful, turbulent initial condition to study the evolution of the dense structures formed at the midplane. This improves on past efforts that assumed only idealized environments or isolated SN explosions (e.g. [Hennebelle & Iffrig, 2014](#)).

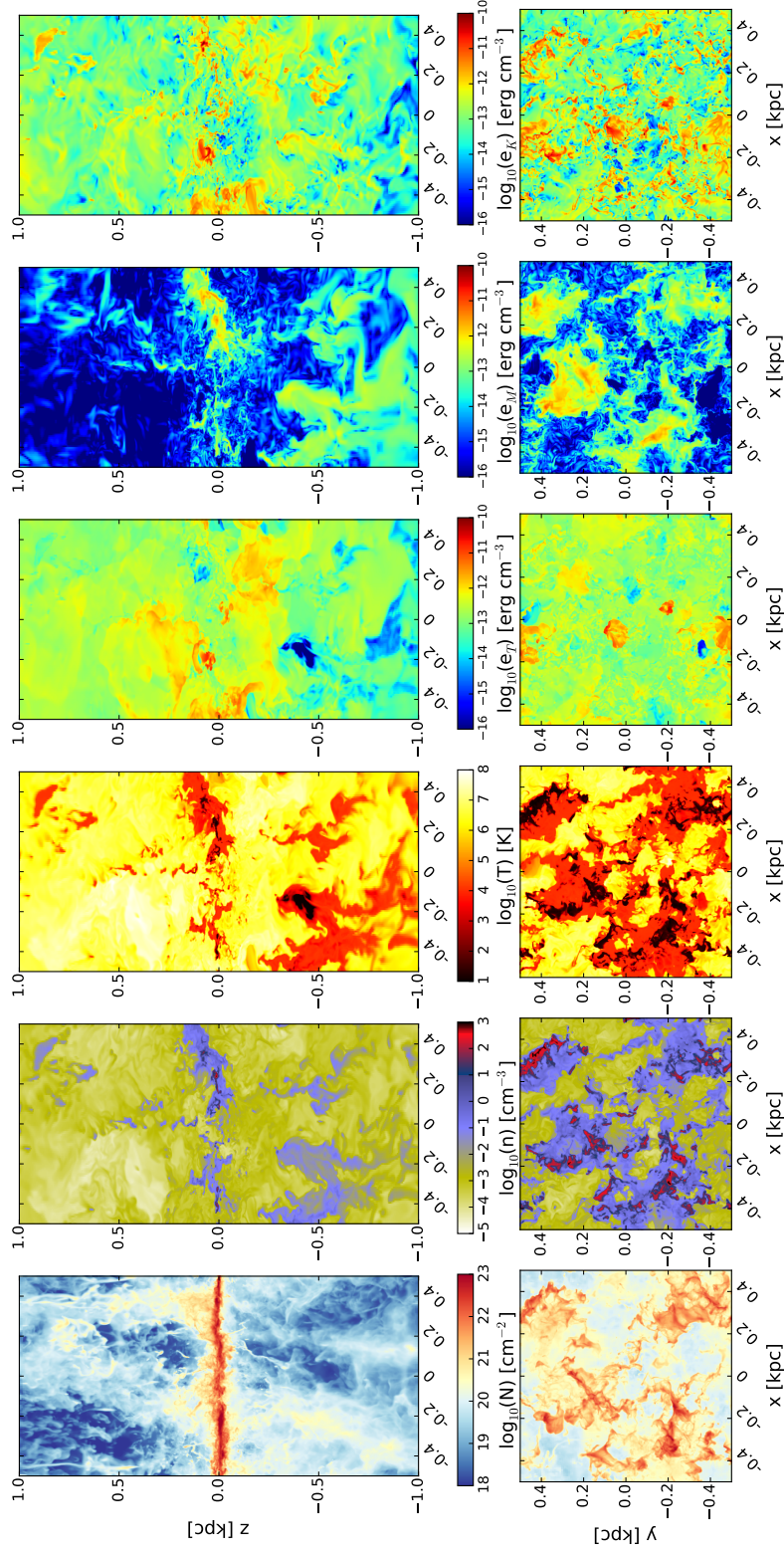


Figure 3-8: Composite figure of the (left to right) projected column density, volume density, temperature and thermal, e_T , magnetic, e_M and kinetic, e_K , energy densities of the gas in the stratified box at $t = 230$ Myr, prior to the onset of self-gravity. In all cases the top panel shows the $1 \text{ kpc} \times 2 \text{ kpc}$ region around the midplane viewed parallel to the Galactic midplane, with the slices taken at $y = 0$ pc and the bottom panel shows the 1 kpc^2 cross-section of the box, viewed perpendicular to the Galactic midplane, with the slices taken at $z = 0$ pc. Note that the energy slices are all on the same color scale, allowing direct comparison.

Chapter 4

Gravitational Contraction vs. Supernova Explosions

The co-authors of this study are Mordecai-Mark Mac Low, Ralf S. Klessen and Christian Baczynski ([Ibáñez-Mejía et al., 2016](#)).

4.1 Motivation

Understanding what regulates molecular cloud (MC) properties is key to understanding their evolution and role in the star formation process. Four decades ago, molecular line observations of dense interstellar clouds revealed that clouds have internal velocity gradients far larger than expected from thermal velocities ([Zuckerman & Palmer, 1974](#)). These fast turbulent motions were first interpreted as signatures of gravitational collapse ([Goldreich & Kwan, 1974](#)). However if the observed MCs were collapsing in a free-fall time, the expected star formation rate would be an order of magnitude larger than the observed rate ([Zuckerman & Palmer, 1974](#)). In reality the star formation process is controlled by a non-linear combination of self-gravity, turbulence, magnetic fields, radiation, and gas heating and cooling (e.g. [Mac Low & Klessen, 2004](#); [Gnedin et al., 2015](#)). How these processes come together to regulate the formation, evolution, and collapse of MCs remains a subject of active research ([Dobbs et al., 2014](#), and references therein). Idealized simulations of artificially driven turbulence in isolated MCs has provided the foundations for present analytical star formation models ([Krumholz & McKee, 2005](#); [Padoan et al., 2012](#); [Federrath & Klessen, 2012](#)). However it remains unclear if these simulations accurately capture the processes dominating real MC properties, and therefore represent real star formation relations. It is of critical importance to understand the interaction between

self-gravity and turbulence for a realistic setup. In this chapter we present the study of a simulated cloud population formed in a kiloparsec-scale, magnetized, supernova (SN) driven, turbulent, interstellar medium (ISM), and compare the properties of the simulated clouds with the properties of observed MCs in the Galaxy.

4.2 Methods and Simulations

4.2.1 Stratified Box Simulation

We present and analyze results from three-dimensional numerical simulations of self-gravitating, magnetized, SN-driven turbulence in the ISM, introduced in chapter §3.

We use the turbulent initial conditions developed after 230 Myr of evolution of the stratified box simulations. During this period, SN explosions inject energy to the ISM, providing the energy to support the midplane from collapsing, and establishing the disk scale height (Ostriker et al., 2010; Shetty & Ostriker, 2012; Hill et al., 2012; Kim et al., 2013; Walch et al., 2015; Girichidis et al., 2016a,b), as well as forming dense clouds in converging flows. SN explosions are present during the entire evolution of the simulation. Initially, clouds form from convergent flows driven by SN shock fronts. During the non-self-gravitating evolution of the simulation, clouds can not gravitationally collapse but are continuously shocked and pushed around by large-scale flows. The gas naturally forms a multiphase ISM with most of the mass concentrated in the cold, dense phase while most of the volume is filled by warm and hot diffuse gas, as discussed in Hill et al. (2012).

At this time we turn on gas self-gravity and follow the evolution of the cloud population as it evolves in this turbulent ISM, while continuously driving turbulence with SN explosions. Table 5.1 shows the final state of the grid refinement at the moment we turn on self-gravity. We do not include sink particles in these simulations but allow gas to collapse to the grid scale without any additional refinement in self-gravitating clouds.

4.2.2 Cloud Identification

In order to investigate the properties of individual giant MCs, we need to extract them from our simulations. Ideally a comparison between simulations and observations would include chemistry and radiative transport in order to capture the non-equilibrium abundance of molecules and model the excitation and attenuation of molecular lines. This is however out of the

resolution [pc]	height	ref. type
0.95	$z \leq 50 $ pc	AMR
1.90	$z \leq 300 $ pc	static
3.80	$ 300 $ pc $< z < 1 $ kpc	static
7.60	$ 1 $ kpc $< z < 3 $ kpc	static
15.2	$ 3 $ kpc $< z < 10 $ kpc	static
30.4	$ 10 $ kpc $< z < 20 $ kpc	static

Table 4.1: Final grid refinement at 230 Myr of evolution, the moment at which we turn on gas self-gravity in the simulation. Nested static layers of grid refinement with an additional level of AMR ensure the bulk of the computational effort focuses on dense clouds in the midplane.

scope of this thesis, so we do not include a model for chemistry, and identify clouds instead by a density threshold. This still allows us to investigate the dynamical properties of the clouds in our simulations. We define our clouds as connected structures above a volume density threshold of $n_{th} = 100 \text{ cm}^{-3}$, chosen to roughly follow the region containing the observable tracer molecule CO. In order to investigate the variation of the velocity dispersion with the size and surface density, we perform our analyses for two different density ranges within the clouds, inspired by the different density ranges traced by commonly observed molecules such as CO, CS, NH_3 , N_2H^+ or HCO^+ (Shirley, 2015).

The low density range covers number densities between $100 \text{ cm}^{-3} \leq n_{\text{low}} \leq 5000 \text{ cm}^{-3}$. This approximately represents the gas densities at which CO is abundant in the gas phase, and its emission is excited (Draine, 2011; Klessen & Glover, 2014). Although ^{12}CO lines quickly saturate for typical column densities encountered in gas at number densities $\sim 200 \text{ cm}^{-3}$, velocity gradients within the cloud reduce line overlap allowing more CO line photons to escape and be observed Shetty et al. (2011), up to number densities of $\leq 5 \times 10^3 \text{ cm}^{-3}$ making it a good tracer for the dynamics of molecular cloud envelopes. Hereafter, we refer to the structures captured by this density range as “clouds”. The high density range corresponds to number densities between $5 \times 10^3 \text{ cm}^{-3} \leq n_{\text{high}} \leq 10^5 \text{ cm}^{-3}$. This density range roughly correspond to the volume densities where (1-0) transitions from CS, NH_3 , N_2H^+ or HCO^+ are observed (Evans II, 1999; Shirley, 2015). Hereafter, we call the structures captured by the high density tracer “clumps”.

As an example of the need for proxies of different molecular tracers, it has been suggested that the MCs envelopes contain most of the observed CO, and

that these envelopes evolve more slowly than the dense cores where stars form (Elmegreen, 2007). Given that we perform our analysis on mass weighted quantities, if we included all the gas above a volume density threshold of $n_{thr} \geq 100 \text{ cm}^{-3}$, our results would be dominated by these dense, quickly evolving cores, and thus could not be directly compared to CO observations.

We identify our clouds and clumps in three-dimensional Position-Position-Position (PPP) space rather than in the projected Position-Position-Velocity (PPV) as done in the observations. However, previous studies of turbulent boxes show that the results for $\sigma - R$ power law relations do not vary significantly between PPP and PPV analysis (Ballesteros-Paredes & Mac Low, 2002; Shetty et al., 2010; Beaumont et al., 2013). A recent study by Pan et al. (2015) also compared the properties of GMCs in PPP and PPV space in galactic disk simulations, again concluding that both techniques seem to identify the same structures.

We compute the mass for each structure by integrating the total amount of mass within each density range, $M_\rho = \sum \rho_i \Delta x_i^3$, given the volume density ρ_i and the cell volume Δx_i^3 for all cells N belonging to a cloud, excluding clumps within, or to a clump. We calculate the size as the radius of a sphere equal to the volume encompassed by the lower threshold of a given density range, $R_\rho = (3V_\rho/4\pi)^{1/3}$.

In order to resolve the turbulent motions above the numerical dissipation scale, a minimum resolution of 10 cells is necessary (Kritsuk et al., 2006, noting that Konstandin et al. (2014) already reports some numerical dissipation of turbulent modes resolved with less than 50 cells) We consider resolved structures those with an effective diameter of $2R_\rho = 10\Delta x$, to ensure that their internal turbulent velocities are not significantly suppressed by numerical diffusion. In this work, this condition corresponds to a minimum radius¹ of our clouds and clumps $R_\rho \geq 4.8 \text{ pc}$.

When self-gravity is included the relevant length scale is the Jeans length,

$$\lambda_j(n, T) = \left(\frac{15k_B T}{4\pi G \mu^2 n} \right)^{1/2} = 3.31 \text{ pc} \left(\frac{n}{100 \text{ cm}^{-3}} \right)^{-1/2} \left(\frac{T}{20 \text{ K}} \right)^{1/2}, \quad (4.1)$$

where k_B is the Boltzmann constant, G is the gravitational constant and $\mu = 1.3017m_H$ is the mean mass per particle assuming neutral, atomic gas with a helium fraction of 0.097 and the remaining 0.3% in metals. We resolve this length with at least 3.5 cells in the low density range gas. This is marginally below the four cell resolution required by the Truelove et al. (1997) criterion in order to avoid numerical fragmentation in a differentially rotating

¹We use the cloud radius in this study because most observational re-examinations of Larson's relation in the literature use this variable.

disk. Therefore the peak densities and fragmentation within our clouds and, particularly, our clumps are underestimated. Nevertheless, we recover useful information on the velocity dispersion driven by gas self-gravity. Detailed analysis of cloud and clump sub-structure requires higher resolution, so we defer that analysis to chapter §5 describing zoom-in simulations.

To obtain a velocity dispersion-size relation, we calculate the mass-weighted, one-dimensional, velocity dispersion for each density range using the three-dimensional velocity components v_x, v_y and v_z , as well as the density ρ . For any observed cloud, denser gas contributes more to the observed linewidths. The summation is done over all N zones within the desired density range to give

$$\sigma_{\rho,1D}^2 = \frac{1}{3} \frac{\sum_i^N \rho_i (\vec{v}_i - \bar{\vec{v}})^2}{\sum \rho_i}, \quad (4.2)$$

where $\bar{\vec{v}}$ is the average, mass-weighted velocity summed over all zones in the cloud. Since $\sigma_{\rho,1D}$ corresponds only to the non-thermal, turbulent velocities for a given density tracer, we compute the total velocity dispersion including the average mass-weighted sound speed, \bar{c}_s ,

$$\sigma_{\rho,tot}^2 = \sigma_{\rho,1D}^2 + \bar{c}_s^2. \quad (4.3)$$

In order to quantify the evolution of each cloud when self-gravity is included, we define the individual free-fall time for each cloud as the free-fall for the equivalent, spherically symmetric distribution of gas

$$t_{ff} = (3\pi/32G\bar{\rho})^{1/2}, \quad (4.4)$$

where $\bar{\rho}$ is the average density accounting for all the mass in the cloud or clump. Finally we compute the surface density for a given density range, as the projection of the mass on the area of a circle given by:

$$\Sigma_\rho = \frac{M_\rho}{\pi R_\rho^2}, \quad (4.5)$$

where M_ρ is the mass within a given density range and R_ρ is the radius computed from the volume enclosed by the lower threshold of the density range.

We are also interested in the evolution of these structures in time. To follow this, we include tracer particles in our simulation, injecting 5 million particles around the midplane in the region $|z| \leq 50$ pc, at $t_{SG} = 0$. We extract a cloud population at each snapshot and identify the tracer particles inside each cloud. Finally, clouds are linked through time using the known trajectories of the tracer particles, building cloud evolutionary histories.

4.3 Results

4.3.1 Overview

We use the stratified box simulation at time $t = 230$ Myr as a turbulent initial condition for our self-gravitating model, starting with a maximum resolution of 0.95 pc. At this point, 7,515 SNe have exploded, so the idealized initial conditions of the simulation have long since been erased. The multiphase ISM has reached a dynamical steady state, where the mass and volume filling fractions of the different ISM phases remain constant in time (Hill et al., 2012). After we turn on self-gravity, we evolve the simulation for another 6 Myr. We stop the simulation at that time because we expect that stellar feedback, particularly ionizing radiation, from the stars formed in the gravitationally collapsing regions will dominate the subsequent evolution (e.g. Dale et al., 2005, 2012, 2013a,b; Walch et al., 2012).

Figure 4.1 shows our simulation at the moment when self-gravity is turned on, $t_{SG} = 0$, and at $t_{SG} = 3$ Myr. At $t_{SG} = 0$, the gas morphology shows strong stratification, with a dense midplane, and a complex atmosphere. Above the midplane, outflows produced by SN explosions and inflows arising from cooling and disk gravity drive gas circulation in a fountain-like manner (Shapiro & Field, 1976; Bregman, 1980). The face-on and close-up views show the multiphase structure of the ISM with dense, irregularly shaped clouds that contain most of the mass lying near the midplane.

This cloud population shows a generally filamentary structure, but with filaments that on close examination are broad and diffuse. Once self-gravity becomes active, these clouds begin to collapse inward along their shortest dimensions to form far denser and thinner structures. As these filaments continue to collapse, they begin fragmenting along their lengths, forming dense clumps. Altogether, we find a complex network of coherent filaments that twist and bend and intersect each other, reaching lengths up to ~ 200 pc.

Figure 4.2 shows slices parallel to the midplane through the cloud shown in detail in the previous figure at $t_{SG} = 0$ and 3 Myr. The number density shows a steep gradient at the cloud surface, where a difference of about two to three orders of magnitude occurs between the cloud and the diffuse ISM (Banerjee et al., 2009). At later times, this gradient becomes steeper as the cloud collapses. A similarly sharp gradient is present in the temperature, where a transition between the cold (~ 30 K) cloud and the warm ($\sim 10^4$ K) ISM occurs.

It is important to remember that we have neglected two important cloud destruction processes that will limit their masses and sizes: galactic rotation and stellar feedback. Galactic rotation induces shear that will stretch

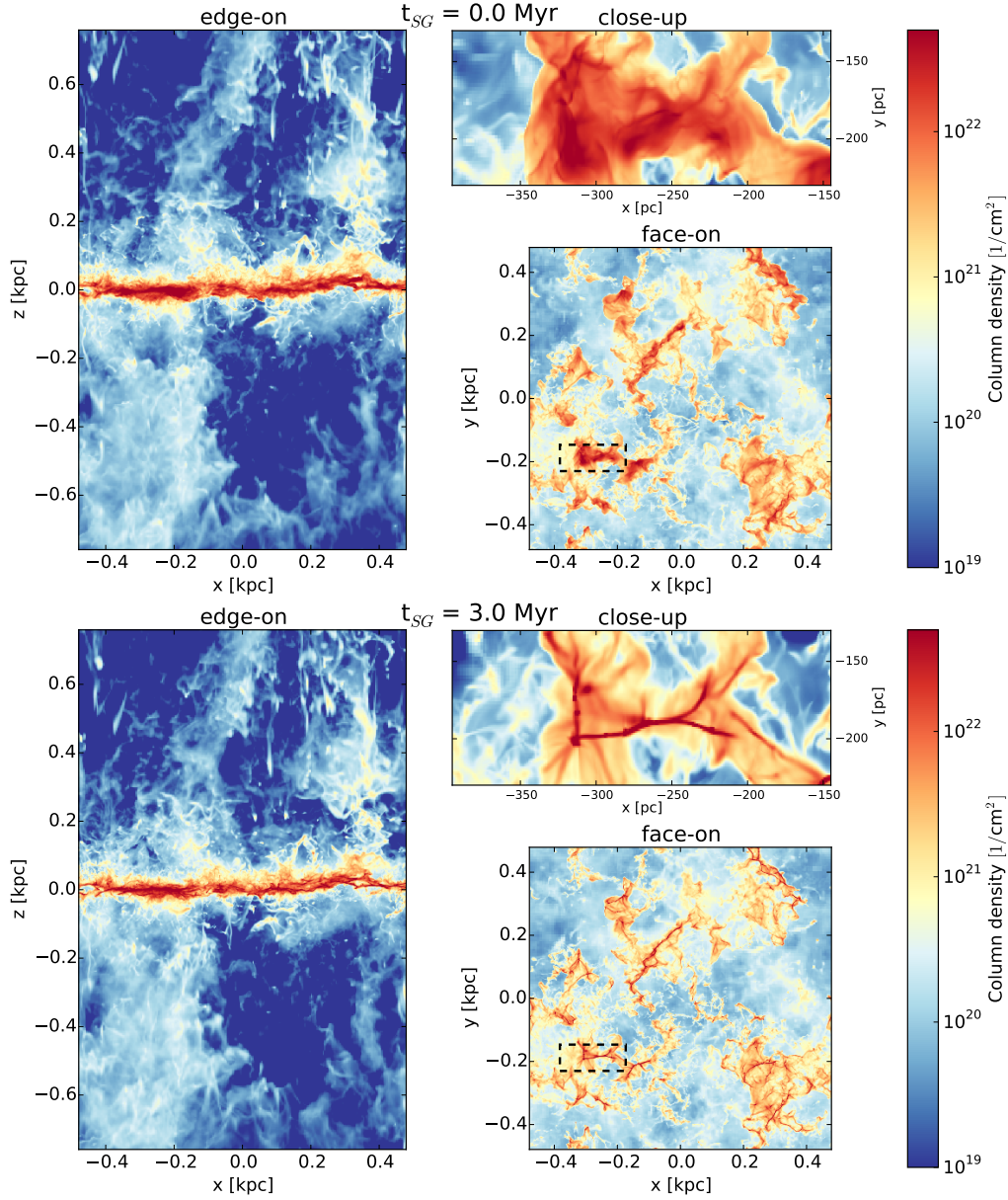


Figure 4.1: Column density projections at times before and after self-gravity is turned on $t_{SG} = 0$ and 3 Myr. Each panel shows (left) an edge-on projection of the inner $1 \text{ kpc} \times 1.5 \text{ kpc}$ of the simulated volume; (bottom right) a face-on projection of the simulated volume, with a 1 kpc^2 footprint; and (top right) a close-up of the structured, irregular, dense cloud shown with a dashed box in the bottom right panel. An animation of the self-gravitating evolution of the simulation during the time $t_{SG} = 0\text{--}6 \text{ Myr}$ is available online.

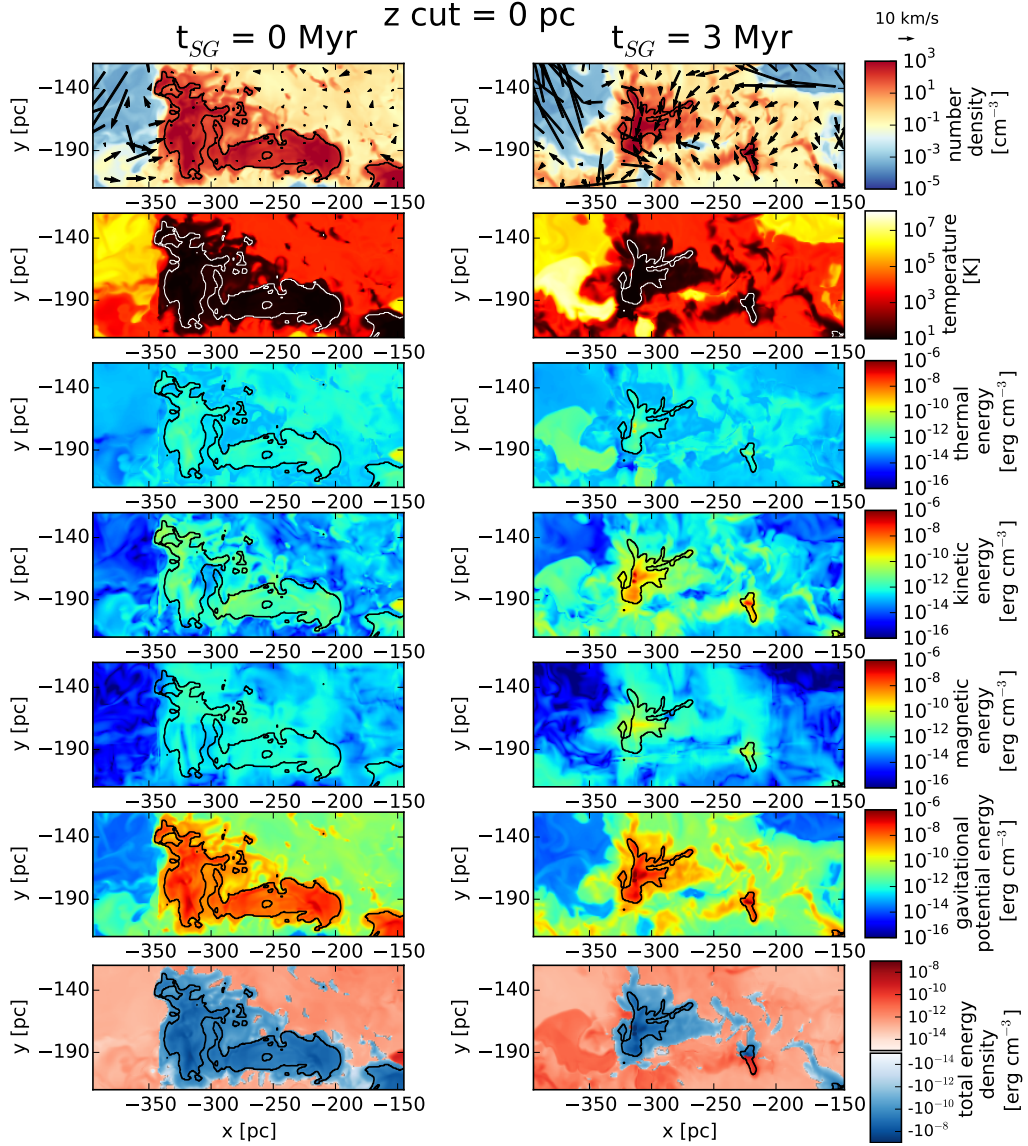


Figure 4.2: Slice plots of number density, temperature, thermal energy density, kinetic energy density, magnetic energy density, gravitational potential energy and the total energy density are shown. For the closeup cloud seen in projection in Figure 4.1 at times before (left) $t_{SG} = 0$ and after (right) $t_{SG} = 3$ Myr self-gravity. The slice lies in the x - y plane, at the midplane $z = 0$. A black contour denotes the cloud boundary in each slice. Velocity vectors in the x - y plane are included to the number density slice in the first row. An animation slicing through this region every parsec for altitudes $|z| \leq 50$ pc is available online. Note that the projection plot of Figure 4.1 captures features at multiple altitudes that do not all appear in any single slice.

the filaments and tear apart the largest clouds. Star formation and the resulting stellar feedback will likely destroy the parent clouds on a timescale comparable to the crossing time. Because of the lack of either of these effects in our simulations, the clouds live far longer than a crossing time during the non-self-gravitating evolution, allowing clouds to accumulate mass and grow substantially larger than would be possible otherwise (see discussion in [Girichidis et al., 2016b](#))

4.3.2 Cloud Population

We now follow the formation, fragmentation, and collapse of dense structures formed in our simulations, extracting approximately 40 resolved clouds and 2–4 clumps at each snapshot. We track the evolution of these structures from one snapshot to the next using tracer particles. We compute the mass M_ρ , radius R_ρ , and velocity dispersion $\sigma_{\rho,tot}$, of the clouds and clumps at each time in the evolution. The initial population is first extracted at the moment self-gravity is turned on, $t_{SG} = 0$, corresponding to a global evolutionary time of $t = 230$ Myr. [Figure 4.3](#) shows the basic properties of our initial cloud population. The simulated clouds span a wide range in radii $4.8 \text{ pc} < R < 40 \text{ pc}$, masses $1.3 \times 10^3 M_\odot < M < 2 \times 10^6 M_\odot$, and mean densities $10^2 \text{ cm}^{-3} < n < 3 \times 10^3 \text{ cm}^{-3}$, corresponding to a range of free fall times of $2 \text{ Myr} < t_{ff} < 4 \text{ Myr}$. The simulated cloud mass function is consistent for different resolutions $\Delta x = 0.47, 0.95, 1.9, \text{ and } 3.8 \text{ pc}$, and for different global evolutionary times, $t = 100, 150, \text{ and } 300 \text{ Myr}$. Most of our clouds are located at distances $|z| < 50 \text{ pc}$ from the midplane, in rough agreement with the observed scale height of the molecular gas in the Galaxy ([Clemens et al., 1988](#)). We focus our presentation on results from our simulations with $\Delta x = 0.95 \text{ pc}$ resolution. We also show resolution studies that reveal numerical effects on the measurement of the velocity dispersion in our simulations.

4.3.3 Virial Balance Evolution

The evolution of molecular clouds is determined by the interplay between thermal energy, turbulence, magnetic fields and gas self-gravity. Rows 3 - 7 in [Figure 4.2](#) show slices of the different energy densities that govern the dynamics of the cloud. Snapshots at two evolutionary times are shown, left, at the moment self-gravity is turned on, $t_{SG} = 0$, and right, at 3 Myr after self-gravity has been active. The thermal energy is roughly uniform throughout the cloud and its environment. The highest variation observed in this slice corresponds to an expanding SN remnant outside the cloud reaching thermal energies three to four orders of magnitude higher than its surroundings. The

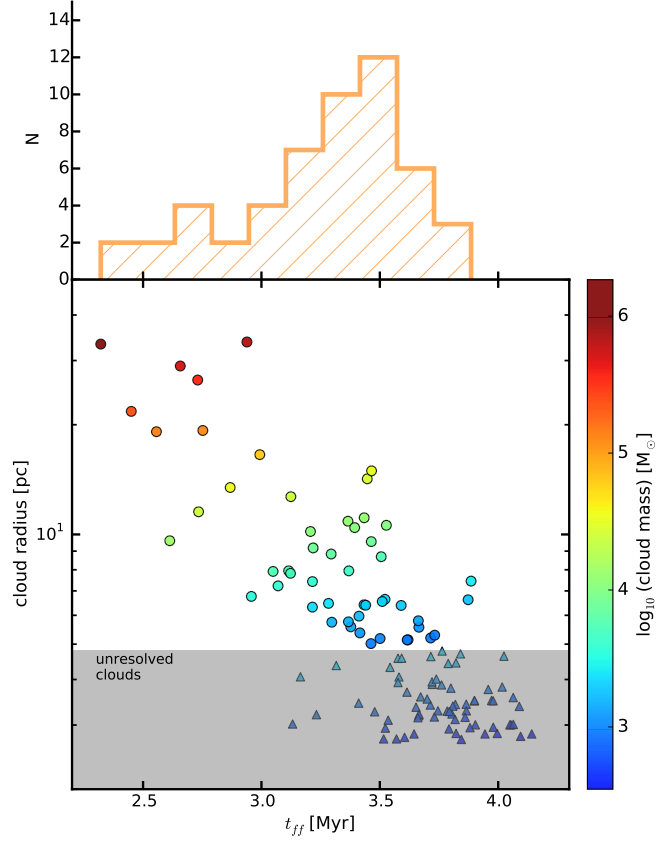


Figure 4.3: Radius R , free fall time t_{ff} , and mass, M_{low} , (shown in color) of the simulated cloud population extracted at the time when self-gravity is turned on $t_{SG} = 0$. The shaded region in the radius– t_{ff} plot lies below the resolution limit for clouds in the simulation, $R < 5\Delta x$. On top a histogram of t_{ff} including only the resolved clouds.

overall contribution of the thermal energy compared to the other components is very low. Although the turbulent velocities inside the cloud are slower than expected (see discussion in section 4.3.4), the kinetic energy inside the cloud exceeds that of the background because of the high densities in the cloud. A significant increase in the kinetic energy is observed at later times as gas falls towards local centers of gravitational collapse throughout the cloud. The magnetic energy shows little variation between the cloud interior and its surroundings at $t_{SG} = 0$. At later times a significant increase in the magnetic energy is observed as the cloud contracts and the magnetic

field is compressed, but the magnetic energy remains subdominant. The gravitational potential energy dominates the overall energy budget of the cloud everywhere, most significant in regions where the density is highest. As the cloud contracts, some of the gravitational potential energy is converted into kinetic and magnetic energy, but the gravitational potential energy also deepens at the centers of collapse. The bottom row of Figure 4.2 shows the sum of the volume energy densities contributing to the cloud energetics, neglecting the surface terms (McKee & Zweibel, 1992) something that we will examine in the future. It is clear that for both snapshots the cloud and its environment is dominated by the gravitational potential energy. This leads to gravitational collapse of the cloud.

We argue that the clouds are in a constant state of gravitational collapse. In order to further explore this idea we examine the behavior of the simplified virial parameter often used in studies of molecular cloud dynamics (Bertoldi & McKee, 1992; Ballesteros-Paredes, 2006; Kauffmann et al., 2013), given by

$$\alpha_{vir} = \frac{5\sigma_{\rho,tot}^2 R_\rho}{GM_\rho}, \quad (4.6)$$

for spherically symmetric clouds, where $\sigma_{\rho,tot}$ is the total velocity dispersion for a given density range, R_ρ the radius and M_ρ is the mass within that same density range. Figure 4.4 shows the virial parameter for the simulated cloud population, revealed by our low density tracer, at $t_{SG} = 0$, and for the evolved cloud population, $t_{evol} > 1$ (see Equation 4.7). Nearly all our clouds are bound and unstable, with $\alpha_{vir} < 2$, particularly before self-gravity has begun to affect the cloud dynamics. At later times, when self-gravity has driven fast, chaotic motions, virial parameters are much higher, though only a few of them reach the marginally stable regime, $1 \leq \alpha_{vir} \leq 2$.

4.3.4 Evolution of the Velocity Dispersion-Radius Relation

Figure 4.5 shows the evolution of the total velocity dispersion, σ_{tot} , vs. the cloud radius, R , for the different density ranges at successive times, t_{SG} , after self-gravity is turned on. At $t_{SG} = 0$ the clouds captured by the low density tracers disagree with Larson's relations in both slope and normalization. At this time, clouds have very low velocity dispersions, $0.35 \text{ km s}^{-1} < \sigma < 0.6 \text{ km s}^{-1}$ that show no correlation with their radius. There is a complete absence of dense and compact structures traced by the high density tracer at $t_{SG} = 0$.

As self-gravity acts, clouds quickly react to this new force, with radius shrinking and internal motions increasing. Figure 4.3 showed that larger

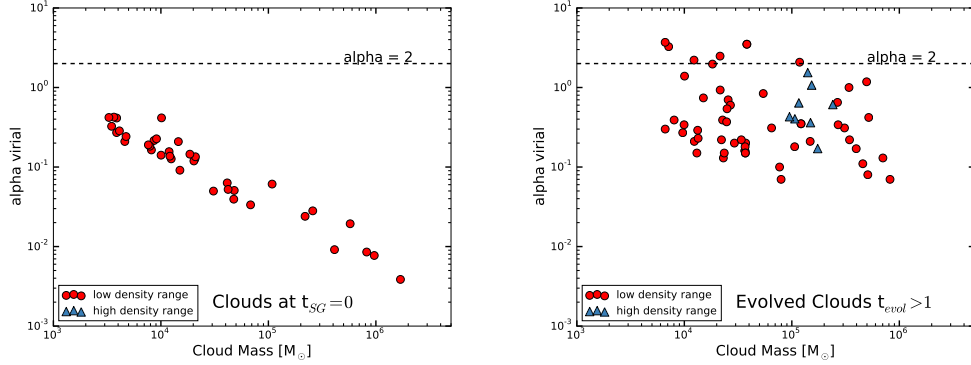


Figure 4.4: Virial parameter vs mass plot for the (left) cloud population extracted at $t_{SG} = 0$ and (right) evolved simulated cloud population $t_{evol} > 1$. (both panels) Black dashed line corresponds to $\alpha_{virial} = 2$ equivalent to a system in virial equilibrium $|E_k| = 2|E_g|$.

clouds are more massive and have shorter free fall times, because they tend to have larger average densities. Consequently these clouds react most strongly to self-gravity, which increases their velocity dispersions. As the simulation including self-gravity evolves, the clouds contract and the gas within them begins flowing towards higher and higher densities while at the same time the clouds continue growing in mass through accretion of ambient material. This processes drives high velocity dispersions that after several megayears begin to show a correlation with the cloud size in agreement with Larson’s relations. Clumps, captured by the high density tracer, increase their velocity dispersions, overshooting Larson’s relations, in agreement with observations of high density tracers (Caselli & Myers, 1995; Plume et al., 1997; Gibson et al., 2009). They collapse faster than their surrounding envelopes, suggesting a hierarchical state of collapse (Elmegreen, 2007). By $t_{SG} = 6$ Myr, clouds and clumps have significantly modified their internal velocity dispersions. The structures captured by the low density range, show a velocity dispersion–radius relation similar to Larson’s fit (see Section 4.3.6 for quantitative discussion).

Resolution Study

The results presented in Figure 4.5 suggest that SN-driven turbulence in the diffuse ISM *can not* drive fast turbulent motions in dense clouds. However many of the clouds presented here are only resolved by 10–20 cells in diameter (a few thousand cells in volume). In order to explore the effects of numerical

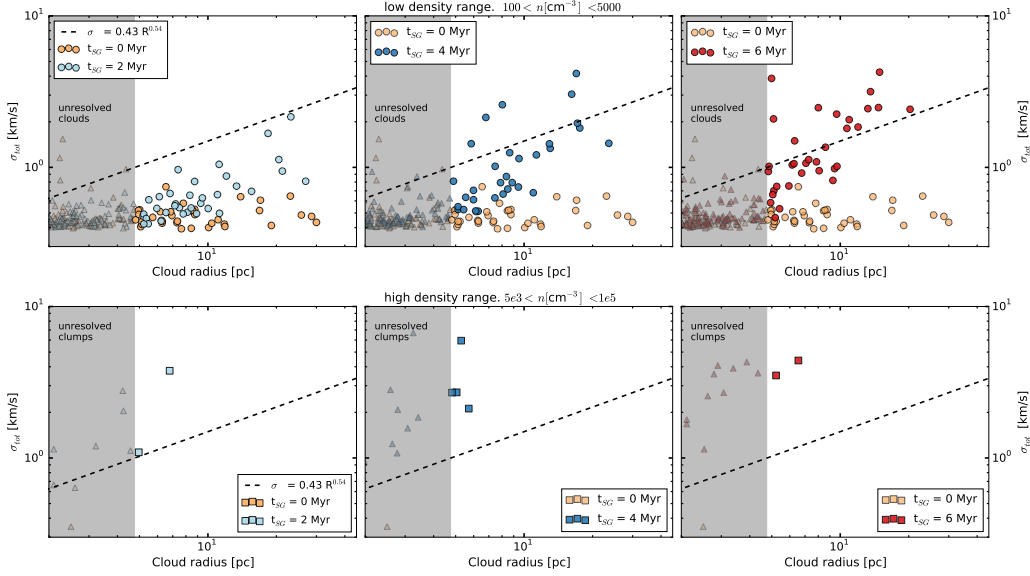


Figure 4.5: Velocity dispersion-radius relation for different density ranges, at different times after self-gravity is turned on in the simulations. For all plots: dashed line corresponds to our best fit to the GRS data of the velocity dispersion-radius relation $\sigma_{tot} = 0.43(R/1 \text{ pc})^{0.54} \text{ km s}^{-1}$, the shaded gray region distinguishing unresolved from resolved objects. Columns show (left to right) evolutionary time $t_{SG} = 2, 4,$ and 6 Myr , while rows show different density tracers (top to bottom) $100 \text{ cm}^{-3} < n_{\text{low}} < 5000 \text{ cm}^{-3}$ and $5 \times 10^3 \text{ cm}^{-3} < n_{\text{int}} < 1 \times 10^5 \text{ cm}^{-3}$. All plots contain the objects extracted at that same density range prior to the action of self-gravity ($t_{SG} = 0$) in orange.

resolution in our results, we run a series of resolution tests. Starting at $t = 230 \text{ Myr}$, we run our simulations forward *without* self-gravity for 10 Myr at resolutions, $\Delta x = 0.47, 0.95,$ and 1.9 pc .

We extract and analyze a cloud population at the final snapshot of each of these simulations. Figure 4.6 shows the $\sigma_{tot} - R$ relation for this cloud population at each resolution. Within the three simulations, the clouds identified have radii in the range $2.5 \text{ pc} < R < 60 \text{ pc}$. At all three resolutions, clouds have low velocity dispersions uncorrelated with radius.

As discussed by Banerjee et al. (2009), as clouds grow, they are unresolved during the initial stages of their formation, but later become resolved as they reach sufficiently large sizes. The high resolution simulation, with $\Delta x = 0.47 \text{ pc}$, resolves small objects at early stages of cloud formation and evolution, so we see more variation of the velocity dispersion in small clouds

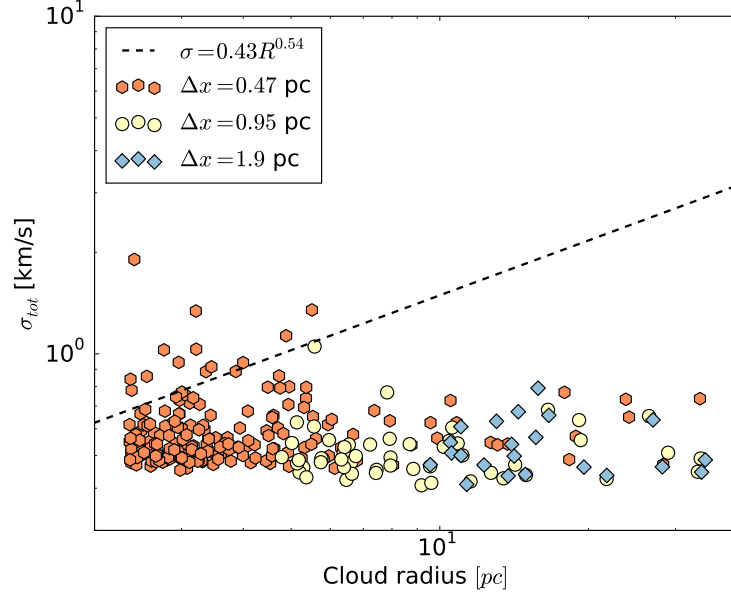


Figure 4.6: Relation between velocity dispersion and radius for the cloud population absent self-gravity at resolutions $\Delta x = 0.47$ pc (orange hexagons), 0.95 pc (yellow circles) and 1.9 pc (blue diamonds). A minimum resolution threshold for the cloud radius of $R \geq 5\Delta x$ is imposed on all three populations. The dashed line corresponds to our fit to the velocity dispersion-radius relation in the GRS data $\sigma = 0.43R^{0.54} \text{ km s}^{-1}$.

for the $\Delta x = 0.47$ pc resolution simulations, compared to the 0.95 pc and 1.9 pc resolution simulations shown in Figure 4.6.

Because of the absence of internal feedback that might destroy the clouds in our simulations, they live long lives. Long lived clouds have enough time for their internal turbulence to decay (Mac Low et al., 1998; Stone et al., 1998). These structures then maintain low internal velocity dispersions while ambient SN-driven turbulence cannot drive strong turbulent motions inside the dense clouds.

4.3.5 Quantifying Cloud Evolution

We want to extract a cloud population that can be directly compared with observations, but we believe that the quiescent clouds at $t_{SG} = 0$ are unrealistic because of their long lives and low velocity dispersions. The gravitationally evolved clouds, on the other hand, appear more physical. Therefore, we wish

to distinguish the evolving clouds and compare only them to the observations. To do this, we follow the evolution of individual clouds through time and quantify their evolution, in order to classify them as quiescent or evolved. For this, we introduce the normalized evolutionary timescale, the ratio of the time self-gravity has been active to the cloud's initial free fall time

$$t_{evol} = t_{SG} / t_{ff}(t_{SG} = 0). \quad (4.7)$$

Most of our clouds are indeed present when self-gravity is turned on, and have initial properties taken at that time. However we also identify a number of clouds formed during the self-gravitating period of the simulation. These clouds are extracted separately. Their initial properties are taken at the time they were first identified as resolved clouds.

We combine all the clouds identified at times $t_{SG} = 0, 1, 2, 3, 4, 5$, and 6 Myr in order to have a mixed population of clouds at different evolutionary stages. Figure 4.7 shows the compilation of these clouds traced by the low density range tracer. The evolutionary timescale t_{evol} allows us to differentiate clouds at different stages of their evolution. A clear distinction can be seen between clouds that have evolved to $t_{evol} > 1$ and those that have not yet reached that point. Clouds that have $t_{evol} > 1$ show higher velocity dispersions and lie close to the expected velocity dispersion-radius relation. Clouds with $t_{evol} < 1$, on the other hand, show low velocity dispersions remaining from their quiescent evolution during the non-self-gravitating period.

From Figure 4.7, it is clear that gravity can increase the internal velocity dispersion of a cloud in a free fall time. The right panel of Figure 4.7 shows clouds formed during the self-gravitating period of the simulations. These clouds still preserve some turbulence left over from their formation and show internal velocity dispersions systematically higher than those of the long-lived, quiescent clouds formed during the non-self-gravitating evolution of the simulation. We use only the population of clouds with $t_{evol} \geq 1$ and the clouds first formed during the self-gravitating period of the simulations to compare with the observations.

4.3.6 Comparison With Observations

The Boston University FCRAO Galactic Ring Survey (GRS) is a molecular line survey of the inner Galaxy. It offers excellent sensitivity (< 0.4 K), high spectral resolution (0.2 km s^{-1}), angular resolution of $46''$ and sampling of $22''$ (Sanders et al., 1986; Clemens et al., 1986; Jackson et al., 2006; Roman-Duval et al., 2010). This survey uses $^{13}\text{CO}(1 - 0)$, which is more suitable for studying dynamics than the commonly used ^{12}CO in previous studies of

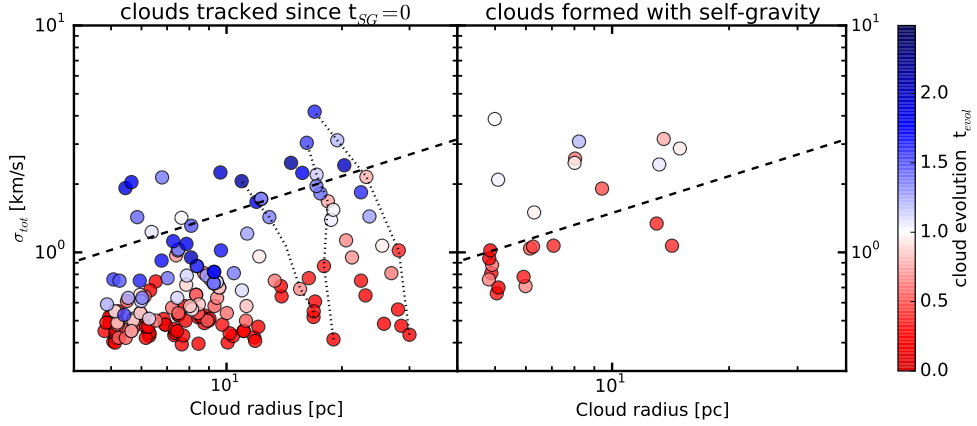


Figure 4.7: Velocity dispersion as a function of cloud radius for clouds tracked during the self-gravitating evolution of the simulation, (left) clouds present at $t_{SG} = 0$, and (right) clouds formed after self-gravity was turned on, $t_{SG} > 0$. Clouds are identified in snapshots at $t_{SG} = 0, 1, 2, 3, 4, 5$, and 6 Myr, and are colored by the evolutionary timescale $t_{evol} = t_{SG}/t_{ff}$. For three cases, dotted lines track the evolution of specific clouds through all snapshots. The dashed line corresponds to our fit to the GRS data $\sigma = 0.43R^{0.54} \text{ km s}^{-1}$.

the Larson’s relations (Larson, 1981; Solomon et al., 1987). This is because ^{13}CO is some 30–70 times less abundant than ^{12}CO (Langer & Penzias, 1990), so it remains optically thin on parsec scales. Therefore ^{13}CO observations have a higher dynamic range of gas column densities than ^{12}CO . We use a subset of the GRS survey here, similar to the data used by Heyer et al. (2009), corresponding to the same clouds observed by Solomon et al. (1987) in their examination of the Larson relations. We perform a Bayesian parameter estimation of the velocity dispersion-size relation to this data. We obtain a posterior distribution for the intercepts with a 2σ high density interval (HDI) of [0.20, 0.82] and a distribution of slopes with a 2σ -HDI [0.31, 0.81]. We take the posterior median slope, 0.54, and median intercept, 0.43, as the canonical $\sigma - R$ relation in all of our plots.

Figure 4.8 shows the $\sigma_{tot} - R$ relation for the GRS clouds and the evolved cloud population from the simulations. The evolved population of simulated clouds have increased their velocity dispersions exhibiting a correlation with the cloud size, now closely resembling the observed GRS cloud population. We emphasize that the lack of correlation in the model without self-gravity is at least as important to our understanding of the dominant physics as the correlation seen in the self-gravitating model.

Figure 4.9 shows the simulated cloud population along with the power

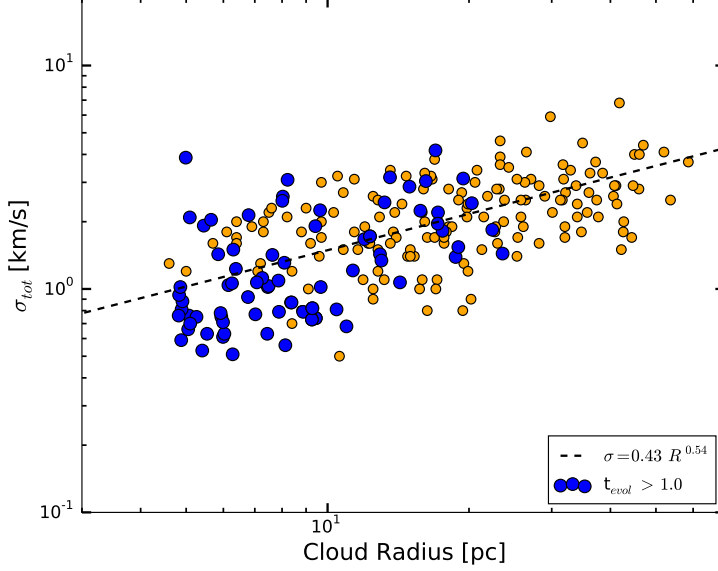


Figure 4.8: Velocity dispersion-radius relation for the subset of the observed GRS cloud catalog used by [Heyer et al. \(2009\)](#) compared to the simulated, resolved, *evolved* clouds with $t_{evol} \geq 1$ as well as the clouds formed at $t_{SG} > 0$. The dashed line corresponds to our best fit of the GRS data $\sigma = 0.43R^{0.54} \text{ km s}^{-1}$.

law regression model, $\sigma = KR_{pc}^\alpha$, applied to that population. We obtain an intercept and a slope of $K = 0.32 \pm 0.11$ and $\alpha = 0.62 \pm 0.12$ respectively, in close agreement to the parameters estimated for the GRS clouds and those derived from other observations ([Solomon et al., 1987](#); [Falgarone et al., 2009](#)). What is notable in our cloud population is that all of our clouds are collapsing gravitationally. This means that including self-gravity to the SN driven cloud population, was enough to produce velocity dispersions consistent with the observations, suggesting that it is the clouds' gravitational collapse that drives the observed non-thermal linewidths ([Lee et al., 2015](#); [Burkhart et al., 2015](#)).

We recover a normalization for the simulated cloud population of $\sigma_{tot}/R_{pc}^{1/2} = 0.32 \pm 0.11$, lower than the historical values of 1.1 reported by L81 or 1.0 by [Solomon et al. \(1987\)](#), but more consistent to the re-examined values, 0.3 for molecular clouds in the outer Galaxy ([Heyer et al., 2001](#)), 0.43 for our parameter estimation of the GRS data or 0.42 found in numerical simulations by [Padoan et al. \(2016\)](#). Sources of uncertainty in our results include

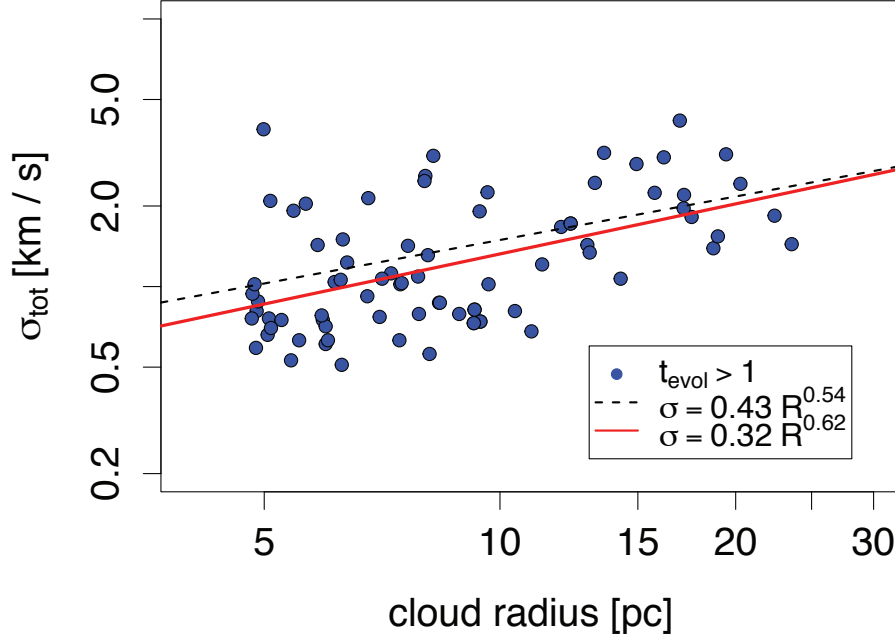


Figure 4.9: Velocity dispersion-radius relation for the simulated cloud population. The red line corresponds to the slope and intercept for our cloud population $\sigma_{tot} = (0.32 \text{ km s}^{-1}) R_{pc}^{0.62}$. For reference, the black dashed line is our fit to the GRS data $\sigma_{tot} = (0.43 \text{ km s}^{-1}) R_{pc}^{0.54}$.

underestimation of the velocity dispersion and overestimation of the clouds sizes and surface densities, as the Jeans length in the clouds is marginally resolved. One should be careful when comparing the normalization of the velocity dispersion-radius relation between simulations and observations, because of four factors that directly affect this quantity: First, it has been shown by [Shetty et al. \(2010\)](#) that the effects of projection have an effect on the measured normalization, but not on the slope of the $\sigma_{tot} - R$ relation. Second, analyses of numerical simulations assume truly optically thin emission for the gas, unless a proper treatment of radiative transfer is applied during post-processing, overestimating the amount of emitting material. Third, most simulations do not follow the non-equilibrium chemical evolution of the ISM, and so do not predict the real abundances of the various emitting molecules. And fourth, as pointed out by [Heyer et al. \(2009\)](#), the velocity dispersion depends not only on the cloud sizes but also on the clouds' surface

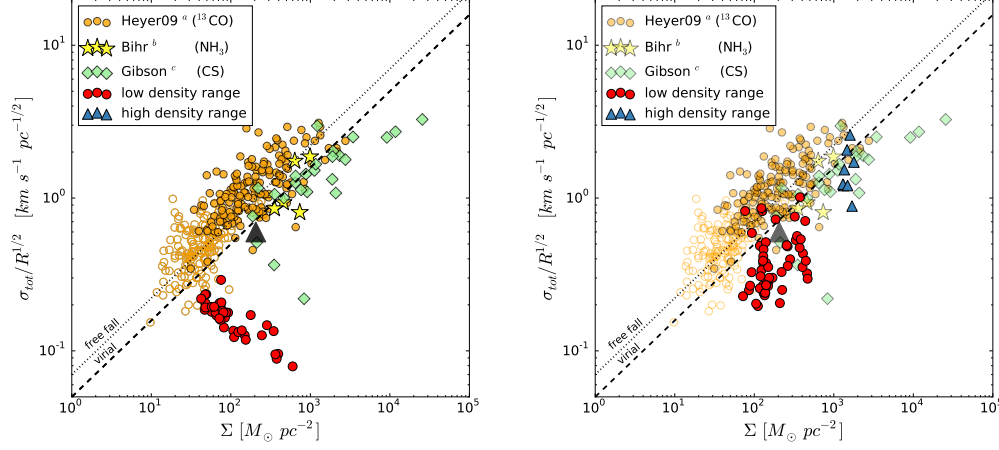


Figure 4.10: Velocity dispersion-radius-surface density ($\sigma - R - \Sigma$) scaling relation for observations and simulations of MCs, clumps, and cores in the Galaxy. Both plots show (orange open and filled circles) observations in ^{13}CO reported by Heyer et al. (2009); (light green diamonds) Galactic infrared-dark clouds observed in CS (Gibson et al., 2009); and (yellow stars) infrared dark clouds observed with NH_3 (Bihr et al., 2015). The black triangle shows the constant value of the column density reported by Solomon et al. (1987) in their size-density relation. Both plots show the simulated objects captured by the low (red circles) and high (blue triangles) density ranges at (left) $t_{SG} = 0$, and (right) after evolution. Clumps are denoted with triangles because they are lower limits for the velocity dispersion, and upper limits for the cloud radius and surface density. The dashed and dotted lines correspond to the relation $\sigma/R^{1/2} \propto \Sigma^{1/2}$, where the dashed line corresponds to the velocity dispersion for a uniform spherical cloud in virial equilibrium and the dotted line the apparent velocity dispersion for a cloud in free-fall collapse.

density, so variation in the analyzed density range can give rise to variation in the normalization.

4.3.7 Variable Column Densities

Since the early studies of the scaling relations in clouds using ^{12}CO , new observations with a variety of tracer molecules sensitive to different density regimes have revealed that the scaling of the velocity dispersion not only depends on the radius of the cloud, $\sigma \propto R^{1/2}$, but also varies systematically with the surface density of the cloud, $\sigma \propto R^{1/2}\Sigma^{1/2}$ (Heyer et al., 2009;

Ballesteros-Paredes et al., 2011). L81 and Solomon et al. (1987) were limited to observations of ^{12}CO , exposing only low to intermediate density molecular gas, as discussed in Section 4.2.2. Because the column density traced by ^{12}CO reaches the same maximum value in all but the smallest clouds, MCs traced by this species appear to all have almost the same column density, when in fact this is purely a radiative transfer effect (e.g. Ballesteros-Paredes & Mac Low, 2002)

Multitracer observations follow the dynamics of gas for a wide range of densities down to dense cores (Caselli & Myers, 1995; Gibson et al., 2009; Roman-Duval et al., 2011; Bihr et al., 2015). Heyer et al. (2009) re-examined the $\sigma - R$ relation for a subset of the ^{13}CO GRS catalog, corresponding to the same clouds analyzed earlier in ^{12}CO by Solomon et al. (1987). The new column densities and masses are directly calculated assuming local thermodynamical equilibrium (LTE), but without assumptions about the virial mass. Given the higher resolution of the data and the usage of a more transparent tracer, ^{13}CO , it is also possible to analyze denser cloud sub-structure.

Figure 4.10 compares observations of velocity dispersion at widely varying cloud surface density and radius including GRS clouds (Heyer et al., 2009), and infrared dark clouds (Gibson et al., 2009; Bihr et al., 2015), to our resolved cloud population at $t_{SG} = 0$ and to our evolved cloud population. As a reference, a black triangle indicates the median values of Solomon et al. (1987) of $\sigma/R_{pc}^{1/2} = 0.72$ corresponding to a uniform surface density of $\Sigma = 206 \text{ M}_{\odot} \text{ pc}^{-2}$.

The simulated cloud population at $t_{SG} = 0$ exhibits low values of $\sigma/R^{1/2}$ and an anti-correlation with the cloud's mean surface density. This happens because clouds formed during the non-self-gravitating evolution period of the simulations have very low velocity dispersions with respect to their masses and sizes. The lack of correlation with $\sigma/R^{1/2}$ indicates that clouds formed in a non-self-gravitating, multi-phase, turbulent ISM have properties clearly inconsistent with observed MCs.

On the other hand the evolved cloud and clump population is located near the expected region in the $\sigma - R - \Sigma$ parameter space, and has a slope consistent with the observed correlation, although the simulated clouds are systematically shifted to slightly lower values of $\sigma/R^{1/2}$ or higher values of Σ . The clumps show velocity dispersions, radii and surface densities similar to those predicted by Heyer et al. (2009) relation. We caution that the properties of our evolved clump population do not fully resolve fragmentation, so they should be considered as upper limits on the cloud size and surface density. Nevertheless, the clear correlation with the observations after self-gravity has been turned on, and not before, strongly suggests that it is gravitational contraction that dominates the observed velocity dispersions,

rather than supernova driving alone.

4.4 Discussion

The balance between turbulent support and gravitational collapse has been argued to determine the formation and evolution of MCs (Mac Low & Klessen, 2004). Simulations of isothermal turbulence continuously driven from large scales show that such turbulence can delay and inhibit star formation (Klessen et al., 2000; Heitsch et al., 2001a; Vázquez-Semadeni et al., 2005; Federrath, 2013). The observed velocity dispersion-size relation has been suggested to originate from the inertial turbulent cascade with no dependence on the gas self-gravity (Kritsuk et al., 2013; Padoan et al., 2016). Observations show that the observed turbulent motions are dominated by the largest-scale modes (Mac Low & Ossenkopf, 2000; Brunt, 2003; Brunt et al., 2009). However, no mechanism has yet been positively identified to continuously drive such large-scale turbulence in MCs.

The most viable candidate for maintaining diffuse ISM turbulence appears to be a combination of field SN explosions and superbubbles (Mac Low & Klessen, 2004; Tamburro et al., 2009; Padoan et al., 2016) and accretion onto the galactic disk (Klessen & Hennebelle, 2010; Klessen & Glover, 2014). However the results we have presented in section 4.3.4 show that SN explosions seem unable to drive turbulence within dense clouds and thus appear unlikely to be responsible for the observed velocity dispersion-size relation in MCs.

In our simulations prior to the onset of self-gravity, clouds form at the stagnation points of convergent flows driven by SN remnant and superbubble expansion. Because of radiative cooling during their formation, this leaves them at lower temperatures and higher densities than their surroundings. During this non-self-gravitating evolution the simulated clouds live very long lives, lasting tens to hundreds of megayears, enough time for the internal turbulence to decay, $t_{decay} \sim R/\sigma$ (Mac Low et al., 1998; Stone et al., 1998; Mac Low, 1999). Although the clouds are constantly being deformed by SN explosions, these do not drive substantial internal turbulence. While SN continue to explode in the diffuse ISM, the clouds maintain low velocity dispersions, which appears to be all that can be driven by the external turbulence.

A possible explanation for this behavior is that turbulence in the diffuse ISM has to climb up a gradient of several orders of magnitude in density to drive turbulent motions in the MC. Momentum is conserved, though the energy drops due to radiative cooling. As a result of momentum conservation,

the velocity drops as the density increases, so that the turbulent motions in the resolved dense interior of the MCs remain well below a kilometer per second, more than an order of magnitude below the tens of kilometer per second driving flows. During the self-gravitating evolution of the simulation, clouds also seem to accrete material from their environment. We do not distinguish here between accretion driven turbulence and contraction.

Results presented here are in direct contradiction with the argument of Padoan et al. (2016, hereafter P16) who suggest that SN explosions alone are responsible for the fast turbulent motions inside dense clouds, and also with the argument of Kritsuk et al. (2013, hereafter K13), who suggest that internal turbulent motions in molecular clouds originate by a supersonic turbulent cascade whether or not self-gravity is included.

It is difficult to directly compare the simulations presented in this work and those analyzed by both P16 and K13, as they differ in several critical characteristics. P16 simulate a 250 pc³ cubic, periodic, unstratified box with a minimum resolution $\Delta x = 0.24$ pc, as opposed to our stratified box, with a minimum resolution of $\Delta x = 0.95$ pc. They show neither a $\sigma - R$ relation plot before self-gravity is turned on, nor the structure function of the same cloud before and after self-gravity. Thus it remains unclear whether their suggestion that supernova driving dominates over self-gravity is well supported.

It is possible that numerical dissipation in our lower resolution models suppresses velocity dispersion at small scales. However, we demonstrated in Section 4.3.4 that the velocity dispersions for clouds larger than 4.8 pc do not change for resolution down to $\Delta x = 0.47$ pc.

In addition, close inspection of Figure 3 of P16 supports our interpretation of gravitational contraction driving turbulent motions in dense gas with $n > 100$ cm⁻³. Before the onset of self-gravity at 45 Myr, the mean kinetic energy is roughly constant, with irregular peaks probably corresponding to the formation of dense structures in convergent flows, that quickly decay after ~ 1 Myr. After the onset of self-gravity, it appears that the mean kinetic energy increases as a function of time. This behaviour can also be observed in their Figure 4, where before self-gravity is active, the mean velocity dispersion is on average 5–6 km s⁻¹. However after the onset of self-gravity, the mean velocity dispersion clearly increases with time up to an average value of 15–16 km s⁻¹. We believe this is at least in part due to gravitational collapse and not solely to SN explosions.

K13 use a suite of periodic-box simulations to argue for a supersonic-turbulence origin of Larson’s laws. In all of the K13 simulations, turbulence is driven by large scale forcing and the analysis is performed once a steady state is reached. This is a crucial difference between our setup and that of

K13, as large scale forcing acts as a volume force term instead of the surface force that one expects from SN-driven or accretion-driven turbulence. Only one of K13's simulations allows for turbulence to decay and includes gas self gravity (HD3, Kritsuk et al. (2011)). This simulation is evolved only for a fraction of a free fall time in the presence of self-gravity, $0.43t_{\text{ff}}$, which also corresponds to a small fraction of the dynamical crossing time, $0.23t_{\text{dyn}}$. Thus, too little time has elapsed for the kinetic energy of the steady state to decay and for self-gravity to affect the velocity structure of the clouds.

For the simulations presented in this work, when self-gravity is turned on, all the clouds begin to collapse simultaneously. This scenario is, of course, only a crude approximation for the evolution of MCs in the Galaxy, as gas self-gravity is always present during the formation and evolution of the clouds, while stellar feedback quickly sets in, preventing long-lived quiescent clouds from occurring. Thus, we do not actually expect that clouds go through a phase of low velocity dispersion, as observed in our clouds at $t_{SG} = 0$, but rather expect the ensemble of observable clouds to always have velocity dispersions consistent with Larson's relation. It is also important to take into account the time it takes to build a sufficient amount of CO to be detectable in a cloud. Colliding flow simulations including non-equilibrium chemistry show that there is a long (up to 10 Myr) phase during which the cloud is held together by ram pressure. During this phase the cloud has enough density to form H_2 , but not enough dust extinction to form CO. Once the cloud becomes Jeans unstable and begins contracting due to its own self-gravity, it reaches column densities sufficient for CO to be shielded and abundant enough to be observed (Clark et al., 2012; Clark & Glover, 2014). This suggests that clouds observed with CO emission are always in a state of gravitational contraction, giving rise to Larson's relations.

As clouds form and turbulent velocities decay, the clouds become more and more self-gravitating. Localized centers of gravitational collapse accelerate the gas, producing a chaotic set of supersonic motions easily interpreted as being due to supersonic turbulence. Given the high Reynolds numbers prevalent in this system, the motions likely are indeed turbulent, but driven primarily by hierarchical gravitational collapse.

The results presented here strongly contradict the hypothesis that SN explosions alone can drive turbulence in MCs that reproduces the velocity dispersion-radius relation or its surface density dependent corollary. Only when self-gravity is included do the velocity dispersions in the simulated clouds increase to values in agreement with observations, as proposed by Ballesteros-Paredes et al. (2011), and agreeing with the more general proposal by Klessen & Hennebelle (2010).

Supernova-driven turbulence remains essential in driving the non-linear

density fluctuations that provide the seeds for hierarchical collapse to proceed. This is seen in Figure 4.1 where the close-up image clearly shows that MCs are far from uniform spheres, but rather have complex, filamentary shapes and density distributions. In this cloud, gravitational collapse does not proceed uniformly but rather hierarchically, depending on the local density distribution. Our results thus support the hypothesis that global collapse of hierarchically structured clouds drives the non-thermal motions observed inside MCs.

Our simulations neglect any explicit correlation between the location of SN explosions and the position of the parent clouds of clusters. Simulations of SN feedback in periodic boxes, have shown that the ISM structure is strongly dependent on the location of the SN explosions, whether explosions are correlated with density peaks, randomly distributed, or something in between (Gatto et al., 2015; Li et al., 2015). However observations demonstrate that only 25% of identified SN remnants are superposed on detectable molecular hydrogen emission (Froebrich et al., 2015), while only 15% show direct maser evidence of interaction with molecular gas (Hewitt et al., 2009). Furthermore, studies of molecular cloud disruption suggest that ionizing radiation has substantially greater effect than winds or SNe (Rogers & Pittard, 2013; Dale et al., 2014; Walch & Naab, 2015). For a more realistic study of the correlation of the SN explosions with respect to the parent cloud, though, models of self-consistent star formation and feedback from massive stars will be required, which we are currently pursuing.

When self-gravity is activated in our simulations, clouds quickly begin to collapse. This means that the clouds in our simulations are not supported by magnetic, thermal, or turbulent pressure. Collapsing clouds increase their internal velocity dispersion as gravitational potential energy is converted to kinetic energy. After a free fall time, clouds approximate equipartition, $|E_g| \sim E_k$ and evolve in that state from there on. However, it needs to be emphasized that equipartition does not imply virial equilibrium, but instead just means that the cloud is converting potential into kinetic energy as it collapses, so that both should be comparable (Ballesteros-Paredes, 2006). Equipartition velocity dispersions are similar to those predicted for clouds in equilibrium, as clouds in equilibrium should also have kinetic energies comparable to the cloud's gravitational potential energy. It is for this reason that it is so difficult to differentiate between collapsing clouds and clouds in equilibrium.

The collapse of a hierarchically structured cloud will proceed at different speeds in different parts of the cloud, since higher density cores have shorter free fall times than their envelopes (Elmegreen, 2007). This idea corresponds to the scenario outlined by Heyer et al. (2009), and Ballesteros-Paredes

et al. (2011) where they discuss the dependence of the velocity dispersion not only on the cloud's size, but on the surface density as well. This scenario agrees with models presented by Elmegreen (1993); Ballesteros-Paredes et al. (1999a,b); Hartmann et al. (2001); Vázquez-Semadeni et al. (2003, 2006), and Heitsch et al. (2005, 2006), where clouds never reach a state of virial equilibrium, but instead are in a constant state of evolution and collapse.

We speculate that our results support the original hypothesis that MCs are generally collapsing suggested by Goldreich & Kwan (1974), but with a twist to the objection by Zuckerman & Palmer (1974) that the free fall collapse of all the molecular gas in the Galaxy would result in far too high a star formation rate. While the clouds are in a state of collapse, they do not collapse globally but in a hierarchical fashion. Before clouds can collapse as a whole and transform most of their mass into stars, dense regions collapse first, forming stars early in the cloud's life (Vázquez-Semadeni et al., 2006, 2007; Elmegreen, 2007). Once star formation in the cloud begins, stellar feedback can disrupt the cloud, maintaining a low star formation efficiency for the MC as a whole.

4.5 Summary and Conclusions

We present numerical simulations of a stratified, multiphase, magnetized, SN-driven, turbulent ISM. We measure the properties of the cloud population that form in this turbulent ISM at an arbitrary time in the simulation prior to including self gravity. We then include gas self-gravity, measure the properties of the cloud population at different evolutionary stages and compare them with observations, focusing in particular on the relations between velocity dispersion, radius, and column density. We find:

- SN feedback in the diffuse ISM only appears able to drive turbulent motions in dense MCs under a kilometer per second, inconsistent with observations. This is most likely because momentum conservation allows only the fast flows in the diffuse medium to drive turbulent velocities in the dense MCs slower by a factor of the density contrast (Klessen & Hennebelle, 2010).
- MCs and their major internal substructures continuously contract gravitationally. We find no evidence for static clouds or clumps in equilibrium. Our simulations include magnetic fields, but these also cannot prevent contraction.
- Gravitational contraction thus appears most likely to be the origin of the velocity dispersion-size relation, driving non-thermal motions

([Traficante et al., 2015](#)) correlated with the cloud size as observed $\sigma_{tot} \propto R^{1/2}$ ([Larson, 1981](#); [Solomon et al., 1987](#); [Falgarone et al., 2009](#)).

- Clouds are in a state of hierarchical contraction, where the velocity dispersion of a cloud or a clump depends not only on the size, but also on the column density, $\sigma^2 \propto R\Sigma$ ([Heyer et al., 2009](#); [Ballesteros-Paredes et al., 2011](#)).

Chapter 5

Gravitational Contraction vs Accretion Driven Turbulence

The co-authors of this study are Mordecai-Mark Mac Low, Ralf S. Klessen and Christian Baczynski (manuscript in preparation).

5.1 Motivation

Molecular clouds are complex, dynamical systems that interact with their environment, exchanging mass and energy through accretion flows and surface forces. Understanding how MCs evolve in a turbulent environment is of critical importance to understand what determines their properties and estimate their future evolution. Most simulations following the detailed evolution of MCs, providing the framework for star-formation models, correspond to isolated, periodic boxes, with artificially driven turbulence (Krumholz & McKee, 2005; Padoan et al., 2012; Federrath & Klessen, 2012). It remains unclear whether these idealized setups accurately capture the processes influencing the properties of MC in the Galaxy, and consequently represent real MCs and star forming environments. It is of critical importance to account for the interaction of the cloud with its turbulent environment in order to identify what are the dominant processes in a cloud's life.

In this chapter we present the study of the accretion rates, measured in a simulated cloud population and three high-resolution zoom-in clouds, developed in a kiloparsec-scale, magnetized, supernova (SN) driven, turbulent, interstellar medium (ISM). We derive a simplified derivation for the expected accretion rates powered by gas self-gravity and by a turbulent environment, and compare this with the measured mass accretion rates, the accretion velocities and the inflow of kinetic energy through the cloud's surface. We

concentrate in the question, if accretion driven turbulence is strong enough to maintain the non-thermal linewidths observed in molecular clouds.

5.2 Mass and Kinetic Energy Influx

In order to provide baseline expectations for cloud accretion, we analytically calculate the mass accretion rate expected for a cloud embedded in an ideal, uniform density environment. We consider two extreme cases. The first case is an initially stationary envelope falling onto the cloud due to its gravitational attraction, while the second case is a turbulent environment that deposits mass onto the cloud by a turbulent advective flux.

5.2.1 Gravitationally Driven Accretion

Assuming spherical symmetry for the cloud, we can express the mass accretion rate as

$$\dot{M} = 4\pi R^2 v_{in} \rho_{ism}. \quad (5.1)$$

If the infall velocity is determined by the velocity of free falling gas at the surface of the cloud, we obtain

$$v_{in}^2 = \frac{2GM}{5R}. \quad (5.2)$$

Adopting the observed empirical relation between the mass and size of molecular clouds (Falgarone et al., 2004)

$$M = 10 M_{\odot} \left(\frac{R}{1 \text{ pc}} \right)^{2.3}. \quad (5.3)$$

which implies that clouds are fractal structures, with a fractal dimension of 2.3. Combining equations 5.1, 5.2 and 5.3, we obtain a mass accretion relation as a function of the density of the environment, and the cloud mass, given by

$$\dot{M} = 8.51 \times 10^{-8} M_{\odot} \text{ yr}^{-1} \left(\frac{n_{ism}}{1 \text{ cm}^{-3}} \right) \left(\frac{M}{10 M_{\odot}} \right)^{1.15} \quad (5.4)$$

where we have assumed that the number density $n_{ism} = \rho_{ism}/\mu$, with $\mu = 1.3017m_H$.

5.2.2 Turbulence Driven Accretion

Turbulent motions carry a net mass flux of $v_{ism}\rho_{ism}$, where v_{ism} is the mean turbulent velocity and ρ_{ism} , the density of the environment. Multiplying by the cloud area yields an estimate of the total mass change. Assuming that the mean turbulent velocity of the environment is constant,

$$v_{ism} \approx 10 \text{ km s}^{-1}. \quad (5.5)$$

Combining equations 5.1, 5.3 and 5.5, we obtain a relation for the expected mass accretion rate driven by the turbulence as

$$\dot{M} = 4.1 \times 10^{-6} M_{\odot} \text{ yr}^{-1} \left(\frac{n_{ism}}{1 \text{ cm}^{-3}} \right) \left(\frac{v_{ism}}{10 \text{ km s}^{-1}} \right) \left(\frac{M}{10 M_{\odot}} \right)^{0.87}. \quad (5.6)$$

Although both relations 5.4 and 5.6 depend on the cloud density, gravitationally driven turbulence has a steeper slope, because the infall velocity is expected to increase with increasing cloud mass, while in the turbulently driven accretion scenario, the increasing mass accretion rate depends on the growth of the surface area of the cloud with mass.

5.2.3 Energy Inflow in Accretion Flows

We now calculate the amount of kinetic energy accreted by the cloud in these two cases. The influx of kinetic energy is given by:

$$\dot{E}_{in} = \frac{1}{2} \dot{M} v_{in}^2, \quad (5.7)$$

where v_{in} is the velocity of the incoming material. Substituting the gravitational mass accretion rate, equation 5.4, and the gravitational infall velocity, equation 5.2, we obtain the kinetic energy influx driven by self-gravity

$$\dot{E}_{in} = 4.61 \times 10^{26} \text{ erg s}^{-1} \left(\frac{n_{ism}}{1 \text{ cm}^{-3}} \right) \left(\frac{M}{10 M_{\odot}} \right)^{1.71}. \quad (5.8)$$

For the cloud embedded in a turbulent environment, the influx of kinetic energy is given by

$$\dot{E}_{in} = 1.32 \times 10^{32} \text{ erg s}^{-1} \left(\frac{n_{ism}}{1 \text{ cm}^{-3}} \right) \left(\frac{v_{ism}}{10 \text{ km s}^{-1}} \right)^3 \left(\frac{M}{10 M_{\odot}} \right)^{1.6}. \quad (5.9)$$

5.2.4 Accretion Turbulence Driving Efficiency

We now ask whether the expected kinetic energy accretion rates derived in the previous section are enough to maintain the turbulent motions observed in molecular clouds, either separately or together. To do this, we derive the efficiency parameter introduced by [Klessen & Hennebelle \(2010, hereafter KH10\)](#),

$$\epsilon = \left| \frac{\dot{E}_{decay}}{\dot{E}_{in}} \right|. \quad (5.10)$$

This parameter compares the decay rate of turbulence in a molecular cloud to the influx of energy through gravitational accretion or turbulent advection. The turbulent kinetic energy, $E = (1/2)M\sigma^2$, for a cloud of mass M , and size R , decays at a rate ([Mac Low, 1999](#))

$$\dot{E}_{decay} = -\frac{1}{2} \frac{M\sigma^3}{R}. \quad (5.11)$$

We estimate the velocity dispersion of a cloud to be related to the mass and size of the cloud by the virial relation

$$\sigma = \left(\frac{GM}{5R} \right)^{1/2}. \quad (5.12)$$

Finally, we assume that clouds are fractal structures with fractal dimension of 2.3 as assumed in [equation 5.3](#).

Comparing the energy decay rate with the energy influx rate for self-gravity driven turbulence, [equation 5.8](#), we obtain

$$\epsilon_g = 5.6 \left(\frac{n_{ism}}{1 \text{ cm}^{-3}} \right)^{-1} \left(\frac{M}{10 M_\odot} \right)^{-0.3}. \quad (5.13)$$

This result suggests that gravitationally driven accretion is sufficient to maintain the observed turbulent motions in molecular clouds. Accretion from a denser gas reservoir is more efficient at driving the internal turbulence as pointed out by KH10. More massive clouds are also more efficient at driving the internal turbulent motions through accretion.

Now, comparing the efficiency of accretion driven by the capture of gas from the turbulent environment, we obtain

$$\epsilon_t = 1.9 \times 10^{-5} \left(\frac{n_{ism}}{1 \text{ cm}^{-3}} \right)^{-1} \left(\frac{v_{ism}}{10 \text{ km s}^{-1}} \right)^{-3} \left(\frac{M}{10 M_\odot} \right)^{0.54}. \quad (5.14)$$

This relation suggests that in the case of a relatively dense environment, with fast turbulent motions, the influx of kinetic energy is sufficient to maintain the turbulent motions observed in MCs.

We expect that the accretion process proceeds as a combination of both turbulently driven accretion and gravitationally driven accretion.

5.3 Numerical Model

We present results from three-dimensional numerical simulations of self-gravitating, magnetized, SN-driven turbulent, multiphase ISM. The simulations use a stratified box consisting of a $1 \text{ kpc}^2 \times 40 \text{ kpc}$ vertical section of the ISM of a disk galaxy, that captures the dynamics of the gas at the midplane, the vertical stratification and the circulation of gas in a galactic fountain up to $\pm 20 \text{ kpc}$. (Joung & Mac Low, 2006; Joung et al., 2009; Hill et al., 2012; Ibáñez-Mejía et al., 2016).

The details of the simulation are described in §3, including the initial conditions and the techniques implemented to develop the turbulent initial conditions. We use those supernova-driven, non-self gravitating, turbulent initial conditions as the starting point of the simulations presented here.

We present results of running single clouds from chapter §4 at various higher resolutions. We start with the data set analyzed in chapter §4, which reaches a maximum resolution of 0.95 pc in a static, nested grid covering the Galactic midplane, $1 \text{ kpc}^2 \times 100 \text{ pc}$. We then re-simulated selected clouds using adaptive mesh refinement in zoom-in regions with varying sizes and maximum resolutions. The refinement condition in these regions requires that the local Jeans length be resolved with four cells, satisfying the Truelove et al. (1997) criterion. Outside the zoom-in region, the nested, static refinement is reduced in resolution, to a maximum resolution of 1.9 pc at the midplane, as described in Table 5.1.

Our goal is to resolve the dynamics of the clouds and their environments, concentrating on gravitationally unstable gas, while simultaneously resolving the background dynamics of the midplane and its interaction with the cloud.

We chose clouds for the high-resolution models from the cloud catalog of simulations with 0.47 pc resolution at the midplane. These simulations evolve at this resolution for 15 Myr neglecting the effects of self-gravity (after a series of successive refinements from longer-time, lower resolution models, as described in chapter §4). A cloud population is extracted for the last two megayears of the simulation and compared with the cloud catalog extracted from simulations at the same evolutionary time but with 0.95 pc resolution. New clouds appear in the high-resolution cloud catalog, forming in convergent

resolution [pc]	height	ref. type
0.06 - 0.47	Zoom-in box $L_{x,y,z}$	AMR
1.90	$z \leq 300 $ pc	static
3.80	$ 300 $ pc $< z < 1 $ kpc	static
7.60	$ 1 $ kpc $< z < 3 $ kpc	static
15.2	$ 3 $ kpc $< z < 10 $ kpc	static
30.4	$ 10 $ kpc $< z < 20 $ kpc	static

Table 5.1: Grid structure for a re-simulated zoom-in cloud. The environment maintains the nested refinement structure while the selected region increases the resolution using adaptive mesh refinement down to a resolution of 0.06–0.47 pc, depending on the cloud.

flows. We select several of these new clouds as our targets for the zoom-in re-simulations. Once a cloud is selected for zoom-in, we position a box of size $(100 \text{ pc})^3$ centered on the cloud’s center of mass. The zoom-in box has a minimum resolution of 0.47 pc and a maximum resolution in Jeans unstable regions of 0.06–0.125 pc depending on the cloud (see table 5.2). Table 5.1 shows the grid structure once a cloud has been tagged for refinement.

In order to follow the dynamics of the accreting gas we inject passive tracer particles in and around the cloud. Tracer particles are injected in a lattice with a size equal to the zoom-in region. We inject a total of 200^3 tracer particles at $t_{sg} = 0$, so that initially we have one tracer particle every $(0.5 \text{ pc})^3$. These passive tracers are evolved using a two-stage, second order, Runge-Kutta scheme.

We use a similar cloud definition to chapter §4. We define clouds in the three-dimensional, position-position-position (PPP) space as topologically connected structures above a density threshold of $n_{thr} \geq 100 \text{ cm}^{-3}$. However, due to the high resolution achieved in these new simulations, parts of the cloud connect and disconnect as material fluctuates above and below the sharp density threshold. For this reason we also define gravitationally bound fragments near the cloud to be part of the cloud. This results in a smooth change in mass as the cloud evolves.

We analyze a total of five simulations in this chapter, listed in Table 5.2. This Table includes the names, maximum resolutions, the size of the the zoom-in box, and whether or not they include gas self-gravity.

Name	Refined region	resolution	Self-Gravity
StBx_1pc_NoSG	1 kpc \times 1 kpc \times 100 pc	0.95	No
StBx_1pc_SG	1 kpc \times 1 kpc \times 100 pc	0.95	Yes
M3e3	(100 pc) ³	0.06	Yes
M4e3	(100 pc) ³	0.47	Yes
M8e3	(100 pc) ³	0.12	Yes

Table 5.2: List of the simulations analyzed in this work. The columns correspond to their names, sizes of the high-resolution box, maximum resolutions, and if self-gravity was included or not in the simulation.

5.4 Results

5.4.1 Overview

We use the evolved state of the stratified-box simulations as the turbulent initial conditions in the simulations presented here. At this point we have a well established multiphase ISM, including vertical gas stratification and a galactic fountain up to ± 20 kpc (Hill et al., 2012). So far, 7,515 SN have exploded in the simulation and they continue to be injected during the subsequent evolution presented in this work. All but one of the simulations presented here include the action of self-gravity and the analysis is performed from the moment self-gravity is turned on. The simulation neglecting gas self-gravity is used to compare the influence of self-gravity and turbulence on the mass accretion rates of the clouds.

Figure 5.1 shows a face-on projection of the box from the simulation with 0.47 pc resolution at the midplane, where the target clouds were extracted. The three target clouds are also shown in close-up windows. Clouds formed in a turbulent ISM have complex density distributions and shapes, with predominantly elongated and filamentary structures. These clouds evolve in a state of hierarchical, gravitational contraction, while simultaneously interacting with their environment, also accreting and losing material as large scale turbulence and nearby SN blast waves interact with the clouds. The shape of the clouds continuously changes due to a combination of gas self-gravity and surface forces. In every case, a large fraction of the injected tracer particles quickly disperses all over the simulation box, while a smaller fraction of the particles interact with the cloud, sometimes ending up being accreted by the clouds. Of the order of ~ 100 thousand particles end up in the clouds at the end of the simulation for all cases.

We stop the simulations at an evolutionary time of $t \approx 10$ Myr, as it

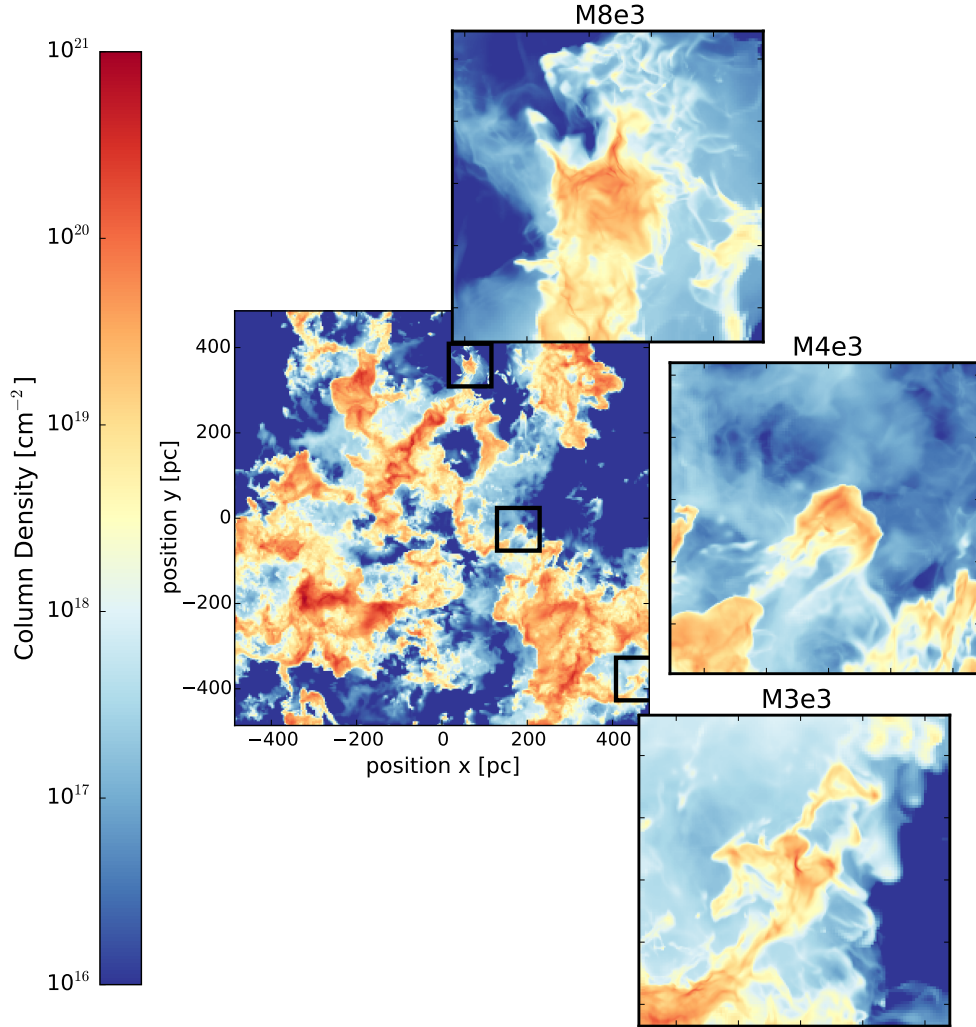


Figure 5.1: Projection of the simulation perpendicular to the Galactic mid-plane at the moment self-gravity is turned on. The zoom-in boxes around the target clouds are superposed. A close-up of each of the clouds is also shown. Separate animations of the evolution of each of the clouds can be found online.

is expected that the massive stars must be feeding back energy in the form of radiation, winds and SN explosions, which should influence not only the cloud properties but their environments. As we do not include self-consistent star-formation and feedback in our simulations, running this setup for longer would lead to un-physical results.

We want to determine the main process driving the accretion of mass onto a cloud, and whether or not the kinetic energy carried by the accreted

material can sustain the observed non-thermal linewidths in the interior of molecular clouds. To answer these questions we focus on two aspects: First, we compare the mass accretion rate for the cloud population in the global simulations with and without self-gravity, and compare the results to the predictions of mass accretion rate expected from the gravitational collapse of a uniform density, spherical envelope, and from turbulent accretion in a uniform density environment. Second, we follow the dynamics of the accreted material in the high-resolution zoom-in simulations, calculating the amount of kinetic energy entering the cloud boundary, in order to quantify the importance of this accretion to the dynamical evolution of the cloud in comparison to the kinetic energy provided by internal contraction.

A detailed analysis of the particle properties at the moment they cross the cloud boundary and the kinetic energy carried by the incoming gas, can be found in section 5.4.3.

5.4.2 Cloud Population

In this subsection we present the results of the simulations at 0.95 pc resolution in the midplane, with and without self-gravity. We concentrate on the influence of self-gravity on the mass accretion rates. For a detailed analysis of the dynamical properties of this population we refer to chapter §4.

Figure 5.2 shows the measured mass accretion rates for the cloud population over 5 Myr of evolution with and without self-gravity. The sizes of the circles correspond to the surface areas of the clouds. In both plots, a correlation between the cloud surface area and the cloud mass is observed. At first glance, it is striking how similar the mass accretion rates for clouds with and without self-gravity are for the mass range between 10^3 – $10^5 M_{\odot}$. At the high mass end, however, there is a clear difference of up to two orders of magnitude in the measured mass accretion rates with and without self-gravity.

Both panels in Figure 5.2 show the predicted mass accretion rates given by a gravitationally collapsing envelope, equation 5.4, and the mass flux rate across the cloud surface given by a uniform density, turbulent environment, equation 5.6. For the mass range between 10^2 – $10^5 M_{\odot}$, the mass accretion rates measured in the simulations lie between the predicted accretion rates driven by self-gravity and turbulence. For the high mass end, it seems like the simulation without self-gravity is unable to supply the amount of mass expected. We believe this happens because turbulent motions are randomly oriented and time dependent, where equation 5.6 assumes the turbulence is constant and pointing towards the cloud. The simulations including self-gravity accrete at the expected rates, this is because in the presence of self-

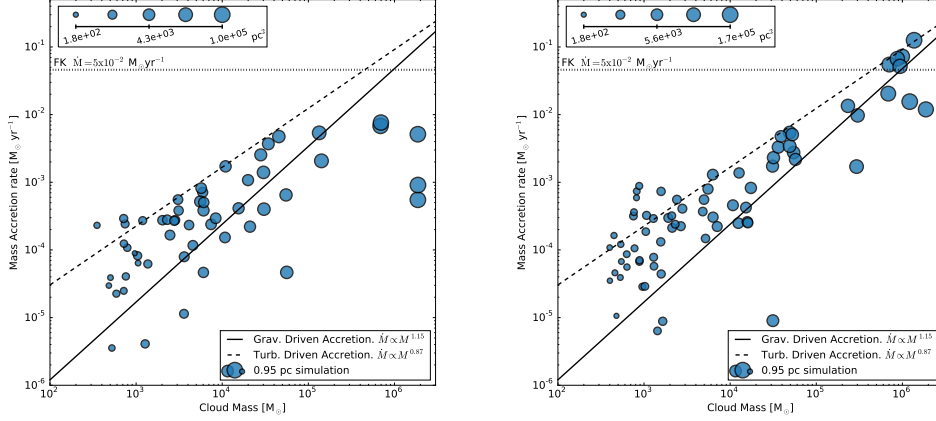


Figure 5.2: Mass accretion rates measured for a cloud population over 5 Myr of evolution without (left) and with (right) self-gravity. The simulations are listed as StBx_1pc.NoSG and StBx_1pc_SG in Table 5.2. The sizes of the circles correspond to the surface area of the clouds. A horizontal dotted line shows the mass accretion rate inferred for GMCs in the Large Magellanic Cloud by FK. The solid black line corresponds to the gravitationally driven accretion case (Eq. 5.4), and the dashed line corresponds to the turbulence driven accretion (Eq. 5.6), for an ambient density of $n_{ism} = 1 \text{ cm}^{-3}$ and ambient velocity of $v_{ism} = 10 \text{ km s}^{-1}$.

gravity, there is a preferential direction for the flows toward the cloud. Therefore, the accretion rates measured in the cloud population, are influenced by the combined action of turbulence and self-gravity.

Figure 5.2, also shows the mass accretion rates derived by Fukui et al. (2009); Kawamura et al. (2009b) and Fukui & Kawamura (2010) for the evolution of GMCs in the Large Magellanic Cloud. (We refer to this accretion rate as FK hereafter.) They measured an average accretion rate of $\dot{M} \approx 5 \times 10^{-2} M_{\odot} \text{ yr}^{-1}$ for GMCs with masses of $M > 10^5 M_{\odot}$. The observed mass accretion rates in the Large Magellanic Cloud indeed generally agree with our predicted mass accretion rates for the combined action of a gravitationally infalling envelope as well as turbulence driven accretion.

5.4.3 High Resolution Clouds

We now discuss the evolution of the individual zoomed-in clouds and their interaction with their environments.

Although the initial masses and virial parameters of the clouds are rel-

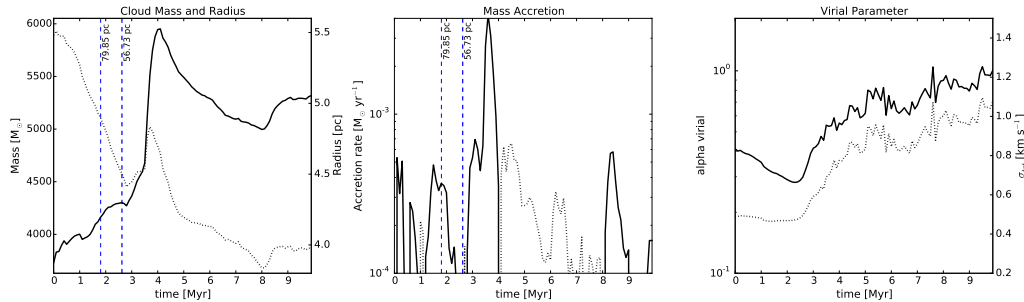


Figure 5.3: Evolution of the properties of the cloud M3e3 starting with the inclusion of self-gravity and tracer particles. *Left to right*: First: evolution of the cloud mass and radius as a function of time. Vertical dashed blue lines mark nearby SN explosions along with their distance to the cloud’s center of mass, with the thickness of these lines inversely related to this distance. Second: Mass accretion rates as a function of time. The solid black line shows positive accretion, while the dashed black line shows mass loss. Red lines correspond to the predicted accretion rates from equation 5.4 for different ISM densities. Third: Cloud virial parameter evolution.

atively similar, the three clouds show differences in the evolution of their parameters and their mass accretion histories. The evolution of the clouds is tightly coupled to the dynamics of their environments, so we present the evolution of each cloud separately. We analyze the properties of the gas immediately before it is accreted onto the cloud, the general behavior of the accreted gas over the 10 Myr of evolution and the global energetics of the cloud with respect to the influx of kinetic energy from accretion.

M3e3 Cloud

Cloud M3e3 is the cloud that gained the least amount of mass during the 10 Myr of evolution. It has an initial mass of $M = 3.6 \times 10^3 M_{\odot}$, initial virial parameter of $\alpha_{vir} = 0.4$, is located at $(x, y, z) = (458, -380, 17)$ pc in the simulation box and has a bulk velocity of $\vec{v} = (0, 3, -2)$ km s $^{-1}$ in the same coordinate system. The cloud has an elongated structure that develops into a long, dense filament of ≈ 20 pc in length as the cloud contracts. This filament then fragments as the cloud continues contracting as a whole.

The cloud is affected by two nearby SN explosions that influence its evolution. We present the location of the SN explosions with respect to the cloud center of mass

$$\vec{d} = \vec{x}_{CM} - \vec{x}_{SN}$$

The first SN occurs at $t = 1.81$ Myr, at a distance of $\vec{d} = (15, -78, -11)$ pc from the cloud. This first event does not have a major impact on the cloud, as it explodes in a big bubble of rarefied gas below the midplane and can expand freely in all directions. The second SN occurs at $t = 2.62$ Myr at $\vec{d} = (7, 51, -23)$ pc from the cloud. This explosion is not only closer, but also occurs in a more confined environment, sweeping a large amount of gas towards the cloud. Together, these explosions fulfill the double task of delivering gas and compressing the cloud, while simultaneously breaking the cloud up and detaching large fragments from it.

Figure 5.3a) shows the evolution of the cloud properties during its 10 Myr of evolution with self-gravity. Cloud M3e3 grows in mass over the initial 4 Myr of evolution, but then loses roughly 15% of its mass during the following ~ 4 Myr. During the last 2 Myr, large nearby fragments of dense gas in the environment become bound to the cloud, effectively contributing to the cloud's growth, showing up in the mass accretion rate, Figure 5.3b).

The cloud does not show a smooth accretion rate, but rather a highly chaotic one, with sudden peaks of mass growth but also periods of mass loss. This rather low mass cloud is significantly affected by the turbulence in the environment, in particular by the nearby SN event at 2.6 Myr.

Looking at the virial parameter, Figure 5.3c), we see that cloud M3e3 already starts with a low value that then continues dropping for the first 2 Myr. Then, at the moment the blast wave of the nearby SN hits the cloud, the virial parameter jumps, and then begins to steadily climb to higher values as the cloud contracts.

At the end of 10 Myr of evolution, cloud M3e3 has contracted down to unresolved structures in the simulation that appear likely to be sites for vigorous star formation.

Instantaneously Accreted Gas: The number density distribution of accreted particles (Fig. 5.4) shows that most of the particles entering the cloud, unsurprisingly, have number densities slightly lower than the number density threshold used to define the cloud. This behavior was expected as the material has to climb up a density gradient to become part of the cloud. However, there are significant variations of the mean number density of the accreting material, revealing clues about the main channels of mass accretion onto the cloud. As seen in Figures 5.3a and 5.4, cloud M3e3 accretes gas at a roughly constant rate over the first 3 Myr, until it is suddenly shocked by a nearby SN explosion.

We identify two stages of the cloud's response after being shocked by a nearby SN explosion. During the short first stage, the cloud accretes low

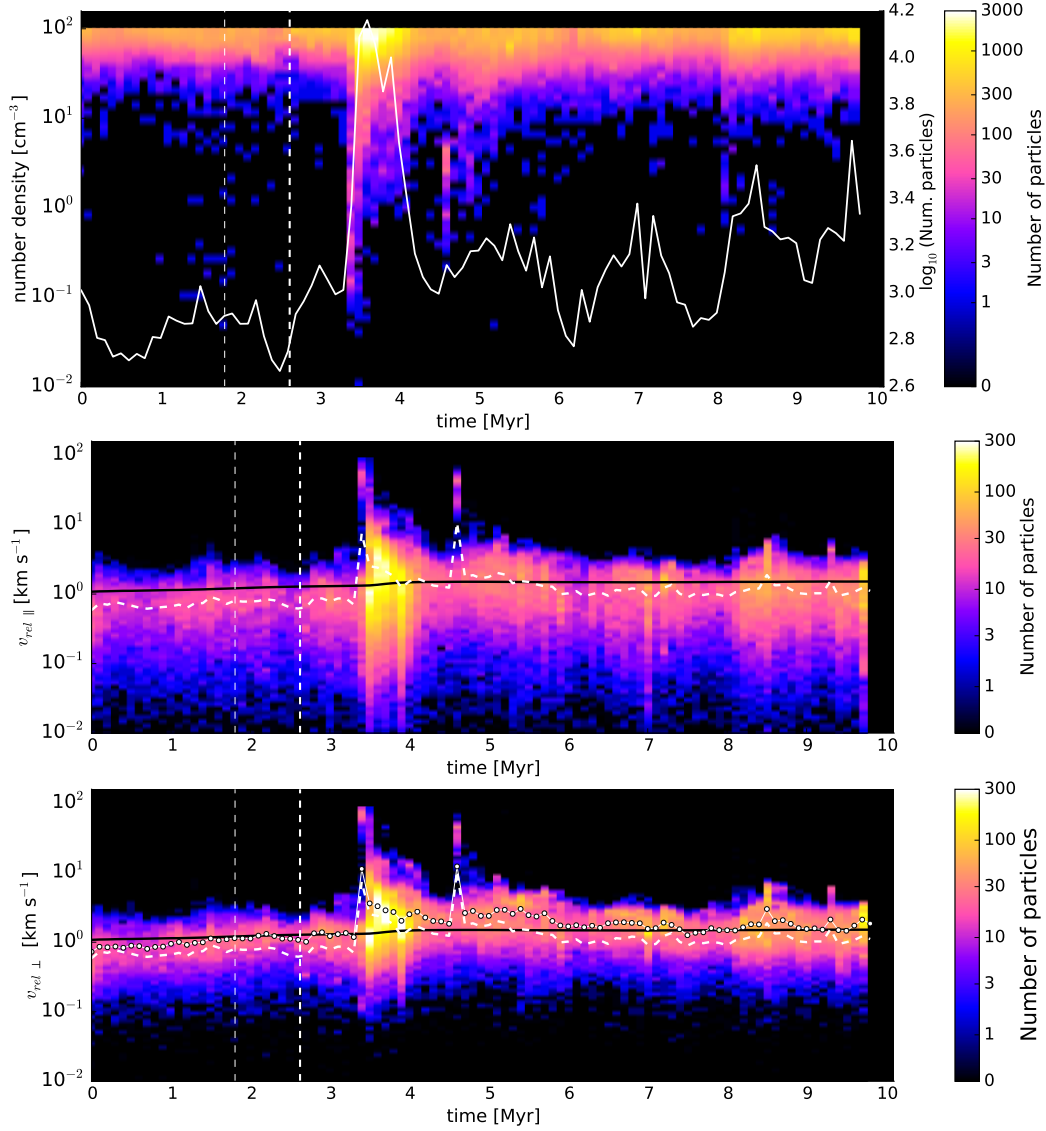


Figure 5.4: Instantaneous accretion onto cloud M3e3. Properties of the accreted gas at the snapshot before being accreted onto the cloud, snapshots are separated by 0.1 Myr in time. a) Number density at the location of the tracer particle. The solid white line shows the total number of tracer particles accreted at each snapshot. The next two panels show the local velocity of the gas relative to the cloud’s center of mass velocity, the solid black line correspond to the predicted infall velocity driven by gravitational collapse (equation 5.2): b) Relative velocity parallel to the density gradient. The dashed line in this and the next panel gives the mean parallel velocity at each bin. c) Relative velocity perpendicular to the local density gradient. The dotted line gives the mean perpendicular velocity.

density, fast moving material. Figure 5.4a) shows that there is almost a uniform distribution of gas with densities between $n_{ISM} = 0.1\text{--}90$ that climbs up the density gradient to suddenly become part of the cloud, with velocities parallel to the density gradient reaching $v_{\parallel} \approx 100 \text{ km s}^{-1}$. This rapid accretion is followed by a longer stage of enhanced accretion from the dense envelope compressed by the SN blast wave. This is seen as an enhanced clump of dense gas accreted over a timescale of $\sim 0.5 \text{ Myr}$ after the fast accretion stage. This second stage accretes material with $v_{\parallel} \approx 2\text{--}5 \text{ km s}^{-1}$, faster than expected from material falling only under the influence of the cloud's self-gravity, as seen in Figure 5.4b. This gas falling into the cloud has not only a high velocity in the direction of the density gradient but also perpendicular to it. This perpendicular velocity corresponds to random gas motions that are not expected to be driven by gravitational collapse, and thus presumably come from the turbulent environment.

The nearby SN explosion also has a negative impact on the cloud mass, as it disrupts part of the envelope and even detaches fragments of the cloud. Although the cloud has been compressed, some of its outermost shells have been puffed up and are now only marginally bound to the cloud, so that the turbulent motions in the environment can provide these regions with enough energy to detach them from the cloud. Thus, during the following 4 Myr of cloud evolution the cloud loses mass (Fig. 5.3). This is not captured in Figure 5.4, as it only displays particles flowing into the cloud, but not ones flowing out.

At the end of the evolution, comparing the mean parallel and perpendicular velocities of the accreted gas (dashed and dotted lines in Figure 5.4c), we notice that the perpendicular velocities systematically exceed the parallel velocities. This suggests that during the entire evolution of the cloud, the mass accretion rate depended strongly on the environmental turbulence. However, the facts that nearby SN explosions could not completely disrupt the cloud's envelope, and that the infalling velocities are close to the velocities expected due to gravitational infall, tell us that self-gravity remains important

Global Evolution of the Accreted Gas: Figure 5.5 shows the global evolution over 10 Myr of ten randomly selected tracer particles that end up in the cloud. The number densities traced by these particles show that particles tend to live for relatively long times in the stable phases of the ISM, and quickly jump between phases when they have the opportunity. The first group of particles lives in the dense phase, $n = 10\text{--}90 \text{ cm}^{-3}$, sampling gas densities near the density threshold used to define the cloud, but also close to the cloud surface, a group we call cold envelope particles. A second group of

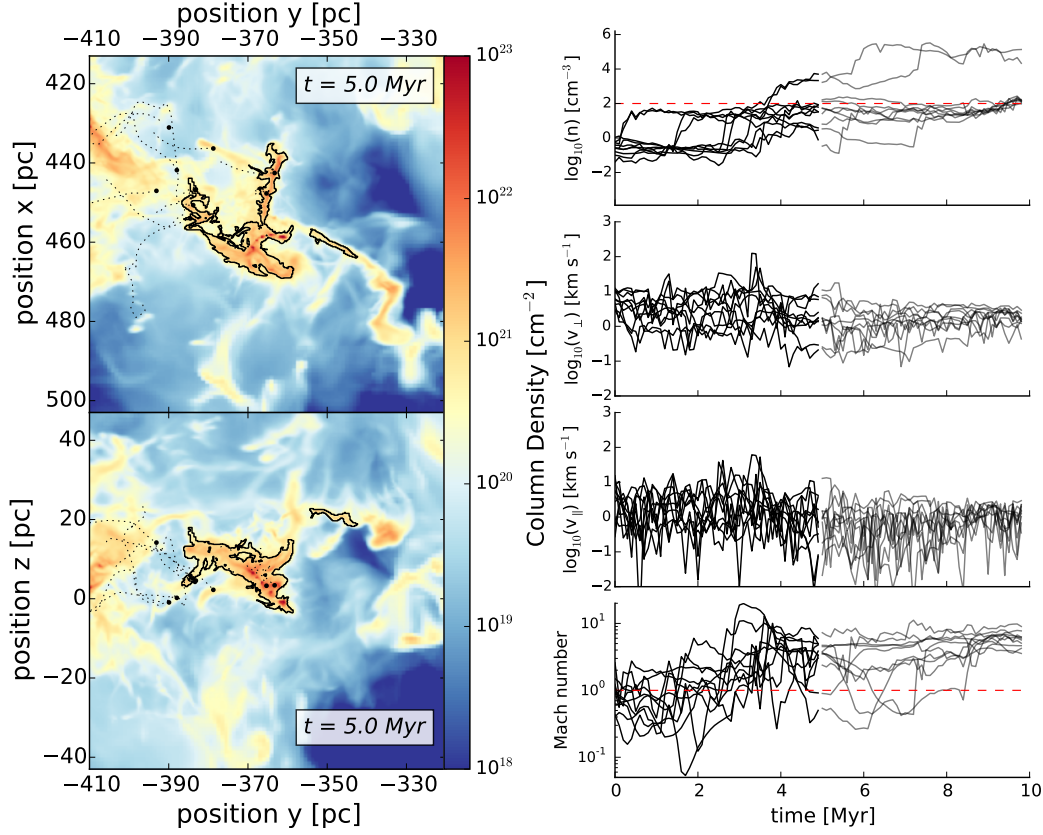


Figure 5.5: Global evolution of selected particles accreted by cloud M3e3. *Left:* Column density projection of cloud M3e3 along lines of sight (top) perpendicular and (bottom) parallel to the midplane. The solid black contour follows the projected surface of the cloud. Both panels include the location of ten randomly selected particles and their trajectories from the moment of injection up to the current time. *Right:* Four panels showing the dynamical properties sampled by each of the ten particles shown in the column density projections at each time in their evolution. Panels show (*top*) local number density traced by the particles during the ~ 10 Myr of evolution. The horizontal dashed red line indicates the density threshold defined for the cloud. (*second and third*) Velocity of the particles perpendicular and parallel to the local density gradient. (*fourth*) Mach number of the particles calculated using the local adiabatic sound speed of the gas and with respect to the center of mass of the cloud. A dashed red line shows the sound speed. An animation of the full 10 Myr evolution of this figure can be found online.

particles moves at higher velocities and traces a lower density environment with $n = 0.1\text{--}1 \text{ cm}^{-3}$, a group we call warm environment particles. The distinction between these two groups is clearly seen in Figure 5.5a at times between $t = 0\text{--}3 \text{ Myr}$. At $t \approx 1.5 \text{ Myr}$ and $t \approx 2.8 \text{ Myr}$, some of the particles in the warm environment rapidly move to the cold envelope as they quickly climb up the density gradient. This change of gas phase is preceded by peaks in both the parallel and perpendicular velocities, followed by drops in the velocities because the particles are forced to conserve momentum as they move into a denser environment.

The mean velocity of the particles perpendicular to the density gradient in the warm environment is of the order of $v_{\perp} \approx 1\text{--}10 \text{ km s}^{-1}$, and their mean parallel velocities are systematically lower almost by an order of magnitude. Once the particles become part of the cold envelope both their parallel and perpendicular velocities drop to $v_{\parallel,\perp} \approx 0.1\text{--}1 \text{ km s}^{-1}$. Due to these low velocities, particles live for long times in the cold envelope as they move to becoming part of the cloud. Sudden events, such as a nearby SN explosion, can compress the envelope, pushing the gas above the density threshold to become part of the cloud. However, there are some cases where particles already in the cold envelope are pushed back to the warm environment when the cold envelope is eroded by turbulence, as is seen to occur to two particles at $t = 5 \text{ Myr}$ and $t = 6 \text{ Myr}$.

The bottom panel of Figure 5.5d, shows the local Mach number of the gas at the position of the particles relative to the cloud center of mass. While the warm environment particle population traces Mach numbers below 1, the cold envelope population and the particles that are part of the cloud always move at locally supersonic speeds. The sudden accretion of fast-moving material pushed by the nearby SN explosion can cause the incoming gas to briefly reach Mach numbers of up to $\mathcal{M} = 20$.

Evolution of the Cloud Energetics: Figure 5.6 shows the gravitational, kinetic and magnetic contributions to the total energy of the cloud as well as the inflowing kinetic energy measured from the instantaneous accretion. The gravitational potential energy dominates over the entire evolution of the simulation. We interpret this to mean that the evolution of cloud M3e3 is dominated by self-gravity, with minor to moderate contributions from the other energy reservoirs.

The initial kinetic energy is very weak compared to the gravitational potential energy, but it is affected by both gravitational collapse and inflow of material onto the cloud. The influx of kinetic energy measured from the simulations shows large fluctuations in time, peculiar to turbulent flows. A

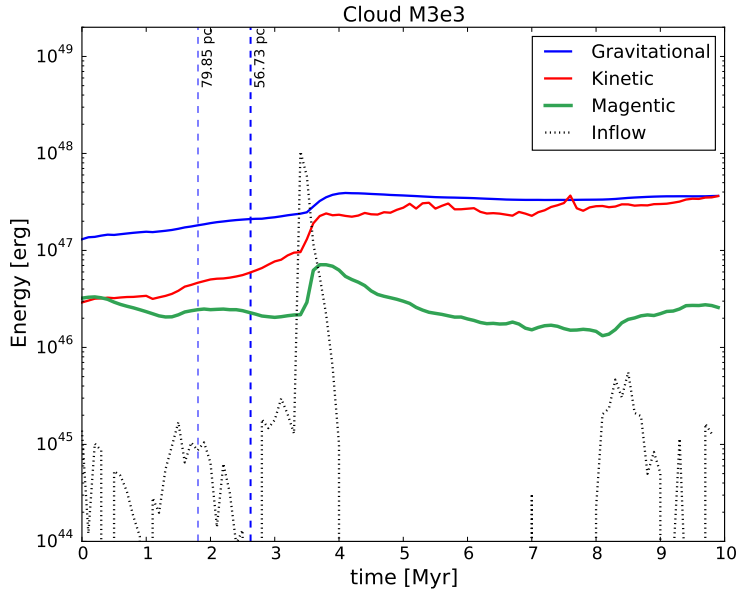


Figure 5.6: Evolution of the total (*solid blue line*) gravitational potential, (*solid red line*) kinetic and (*solid green line*) magnetic energies in the cloud. The (*dotted black line*) total amount of kinetic energy entering the cloud through the accretion flow between snapshots ($\Delta t = 0.1$ Myr) is displayed, as well as the locations of nearby SN events (*vertical dashed blue lines*) at their explosion times, the thickness of the line is related to the distance of the cloud’s center of mass to the SN.

sudden increase in the inflow of kinetic energy occurs after the second nearby SN explosion. This event triggered an enhanced burst of accretion, followed by a phase of erosion and fragmentation of the cloud’s surface. Finally the magnetic energy fluctuates following the general behavior of the other energy reservoirs, but systematically shifted an order of magnitude below. We believe that magnetic fields make little contribution to the fate of the cloud and are unable to prevent it from collapsing.

Comparing the evolution of all the available energies as a function of time, we find that while the cloud is mostly dominated by the gravitational potential energy, sudden events such as the accretion burst at $t \approx 1.5$ Myr, can trigger a chain reaction inside the cloud will have an effect on the global dynamics of the cloud. However we also see that the inflow of kinetic energy onto the cloud, compared to all the other energies, is not only not constant, but also weak compared to the total cloud energy. Another interesting feature

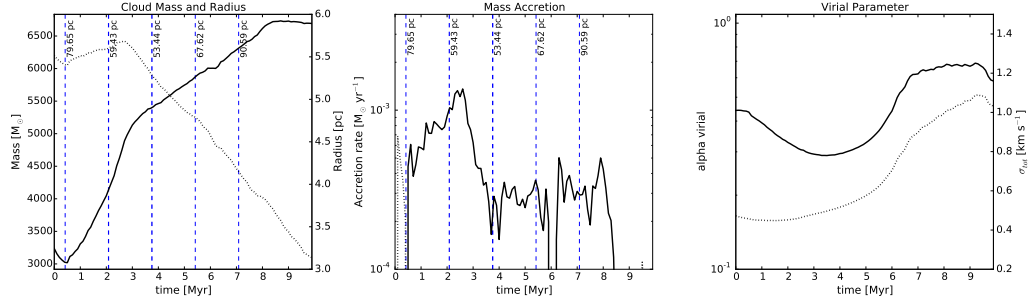


Figure 5.7: Evolution of the properties of the cloud M4e3 starting with the inclusion of self-gravity and tracer particles. *Left to right*: First: evolution of the cloud mass and radius as a function of time. Vertical dashed blue lines mark nearby SN explosions along with their distance to the cloud’s center of mass. The thickness of these lines is related to this distance. The line is thicker the closer the SN exploded. Second: Mass accretion rates as a function of time. Solid black line correspond to positive accretion rates, and dashed black line shows mass decretion rate. Red lines correspond to the predicted accretion rates given equation 5.4 for different ISM densities. Vertical blue lines show the nearby SN events. Third: Cloud virial parameter evolution.

we see here is that as the cloud contracts it converts some of its gravitational potential energy into kinetic energy. For this reason Figure 5.6 shows that the gravitational and kinetic energies are closely related to one another, especially at later times in their evolution.

M4e3 Cloud

Cloud M4e3 has an initial mass and virial parameter of $M = 3.2 \times 10^3 M_\odot$ and $\alpha_{vir} = 0.45$. The cloud is located at $(x, y, z) = (180, -30, 8)$ pc in the simulation box and has a bulk velocity of $\vec{v} = (-1, -1, -1)$ km s $^{-1}$ in the same coordinate system. Although this is the cloud with the most nearby SN explosions, it is nevertheless the cloud that is least affected by them.

The first SN near the cloud occurs at $t = 0.42$ Myr, at $\vec{d} = (-30, 72, 14)$ pc. This SN is behind a giant cloud that shields M4e3 from any influence. After 0.5 Myr, M4e3 begins to accrete gas at a rate of $\dot{M} \approx 5 \times 10^{-4} M_\odot \text{ yr}^{-1}$, which monotonically increases over time as expected from its increasing mass (see Fig. 5.7). A second SN occurs at $t = 2.09$, at $\vec{d} = (-19, 46, 33)$ pc. This SN impacts the cloud shortly after, compressing the envelope and increasing the mass accretion rate up to $\dot{M} \approx 1.3 \times 10^{-3} M_\odot \text{ yr}^{-1}$, but only for a short

period of time. The shock of the blast wave also disrupted the cloud's envelope, which resulted in a long period of low mass accretion rate. This first stage of the cloud's evolution is consistent with the expected accretion rate for a cloud with a dense gas reservoir of $n_{ISM} \approx 60 \text{ cm}^{-3}$. At the end of the first ~ 3 Myr of evolution, cloud M4e3 has gained almost 70% of its initial mass while still roughly preserving a constant size.

At later times, cloud M4e3 continues accreting gas but now at a slightly lower rate of $\dot{M} \approx 2\text{--}3 \times 10^{-4} M_{\odot} \text{ yr}^{-1}$. This lower accretion rate is a consequence of a reduced reservoir, as the cloud envelope has either been accreted onto the cloud or eroded by the turbulent environment. A third, fourth and fifth SN explode far above the midplane at times $t = 3.75, 5.42, \text{ and } 7.09$ Myr, and distances of $\vec{d} = (-3, 23, 48)$ pc, $(8, -3, 67)$ pc, and $(23, -30, 82)$ pc.

These explosions all occur far above the midplane, where they can freely expand without having a major impact on the cloud. Only a small increase in the accretion rate is observed at times between $t = 5.9\text{--}6.2$ Myr. After 8.5 Myr of evolution, there is almost no gas left in the reservoir, and the cloud continues contracting without any further accretion. At this point cloud M4e3 has already doubled its initial mass, and largely collapsed down to unresolved scales.

Instantaneously Accreted Gas: Cloud M4e3 is the cloud that shows the most uniform accretion history of the three clouds. Figure 5.8a shows that although for this cloud nearby SN events have little effect on the cloud, they do trigger some minor bursts of accretion of low density gas, like the ones observed at $t = 0.7$ Myr, 2.3 Myr, and 4.5 Myr. Some of these events also appear in the parallel velocity panel, Figure 5.8b, as sudden peaks of the velocity distribution of the particles. However, as already discussed in section 5.4.3, the overall evolution of this cloud is not significantly affected by the nearby SN explosions but rather is relatively uniform in time.

For this cloud, comparing the mean parallel and perpendicular velocity components of the accreted gas, we see that they are roughly equal during the whole evolution of the cloud. This suggests that the mass accretion into this cloud may be equally dominated by the gravitationally infall of the envelope and by the capture of turbulent material from the cloud.

Global Evolution of the Accreted Gas: The global evolution of the accreted gas onto cloud M4e3 differs from the other two clouds, because this cloud is embedded in a diffuse, hot environment. Figure 5.9 shows the global evolution of the ten randomly selected tracer particles. We identify a group of particles embedded in the third phase of the ISN, a hot, diffuse component.

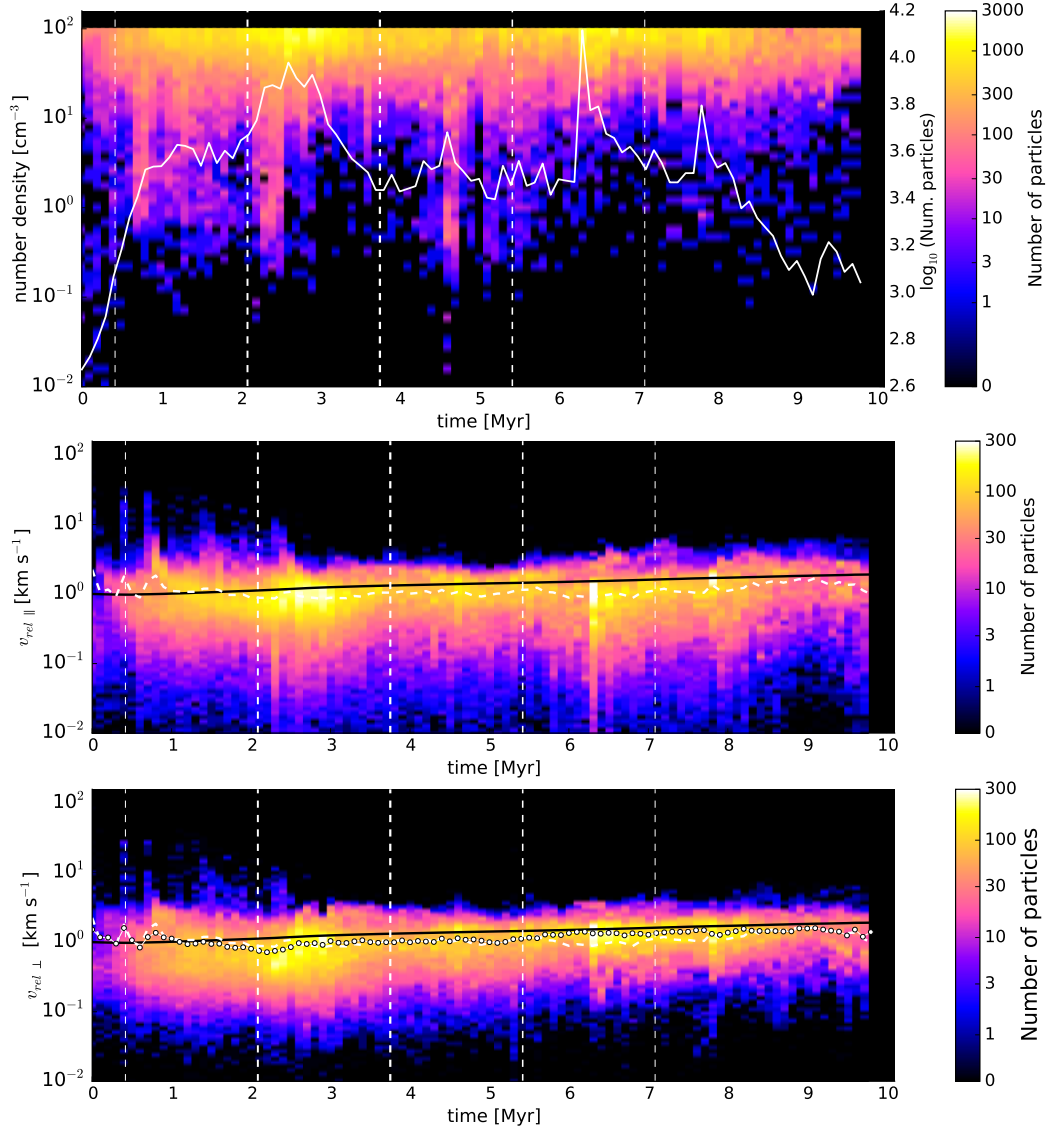


Figure 5.8: Instantaneous accretion onto cloud M4e3. Properties of the accreted gas at the snapshot before being accreted onto the cloud, snapshots are separated by 0.1 Myr in time. a) Number density at the location of the tracer particle. The solid white line shows the total number of tracer particles accreted at each snapshot. The next two panels show the local velocity of the gas relative to the cloud’s center of mass velocity, the solid black line correspond to the predicted infall velocity driven by gravitational collapse (equation 5.2): b) Relative velocity parallel to the density gradient. The dashed line in this and the next panel gives the mean parallel velocity at each bin. c) Relative velocity perpendicular to the local density gradient. The dotted line gives the mean perpendicular velocity.

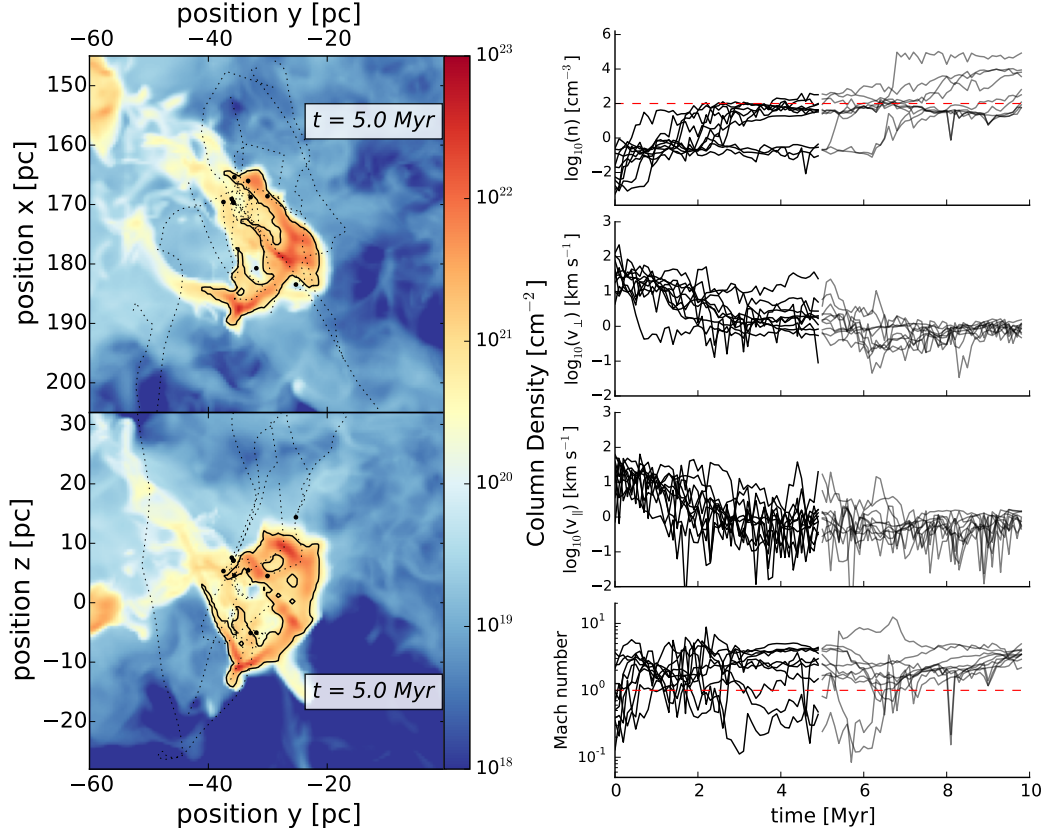


Figure 5.9: Global evolution of selected particles accreted by cloud M4e3. *Left:* Column density projection of cloud M4e3 along lines of sight (top) perpendicular and (bottom) parallel to the midplane. The solid black contour follows the projected surface of the cloud. Both panels include the location of ten randomly selected particles and their trajectories from the moment of injection up to the current time. *Right:* Four panels showing the dynamical properties sampled by each of the ten particles shown in the column density projections at each time in their evolution. Panels show (*top*) local number density traced by the particles during the ~ 10 Myr of evolution. The horizontal dashed red line indicates the density threshold defined for the cloud. (*second and third*) Velocity of the particles perpendicular and parallel to the local density gradient. (*fourth*) Mach number of the particles calculated using the local adiabatic sound speed of the gas and with respect to the center of mass of the cloud. A dashed red line shows the sound speed. An animation of the full 10 Myr evolution of this figure can be found online.

Because cloud M4e3 is surrounded and constantly shocked by hot, diffuse, rarefied gas, many of the particles that end up in the cloud start their lives in this hot, diffuse phase.

These particles have velocities of the order of $\sim 10\text{--}100 \text{ km s}^{-1}$. They quickly climb up the density gradient, reducing their velocities as they become part of the warm environment. Three distinct populations appear in Figure 5.9a at early times. Unlike cloud M3e3, the random particles selected for this cloud also trace the low density, fast moving, hot gas. During this time, warm environment particles occasionally pass through sharp transitions into the cold envelope, while particles in the cold envelope slowly move around on their way to becoming part of the cloud.

Although this cloud is the one that has the most nearby SNe, they do not impact the cloud strongly, as discussed before. For this reason, the accretion onto the cloud proceeds in a more uniform fashion, without strong fluctuations. As particles enter the cloud with velocities of $v_{\parallel} \approx 1 \text{ km s}^{-1}$, they produce only slow shocks with Mach numbers of $\mathcal{M} \approx 1\text{--}5$.

Out of these ten randomly selected particles, only one particle shows two sudden jumps in density, passing through shocks reaching Mach numbers of $\mathcal{M} \sim 10$. This particle is shocked by a SN at $t \approx 4.9 \text{ Myr}$, and is quickly pushed from the warm environment to the cold envelope. Almost immediately the particle becomes part of the cloud and is sucked in by a gravitationally collapsing density peak, maintaining high Mach numbers even in this very dense environment.

Evolution of the Cloud Energetics: Figure 5.10 shows the contribution of the different energies in the cloud. Similarly as seen before, the gravitational potential energy dominates over the entire energy budget at all times for the evolution of the cloud. Regardless of the number of nearby SN explosions, this cloud shows no sign of being affected by them, and the influx of kinetic energy is roughly constant during the 10 Myr of evolution, with small variations around the mean.

The kinetic energy is almost an order of magnitude weaker than the gravitational potential energy. However, as the cloud collapses, it converts gravitational energy into kinetic energy, seen as a steady climb of the kinetic energy from $t = 0.7\text{--}10 \text{ Myr}$. The magnetic energy is low compared to the other energy reservoirs of the cloud, unable to prevent it from collapsing. Comparing the influx of kinetic energy coming from accretion with respect to the other energies, we see that for this cloud, accretion plays only a minor role in the cloud dynamics. However, it is also important to point out that cloud M4e3 has still doubled its mass within 10 Myr of evolution, and thus

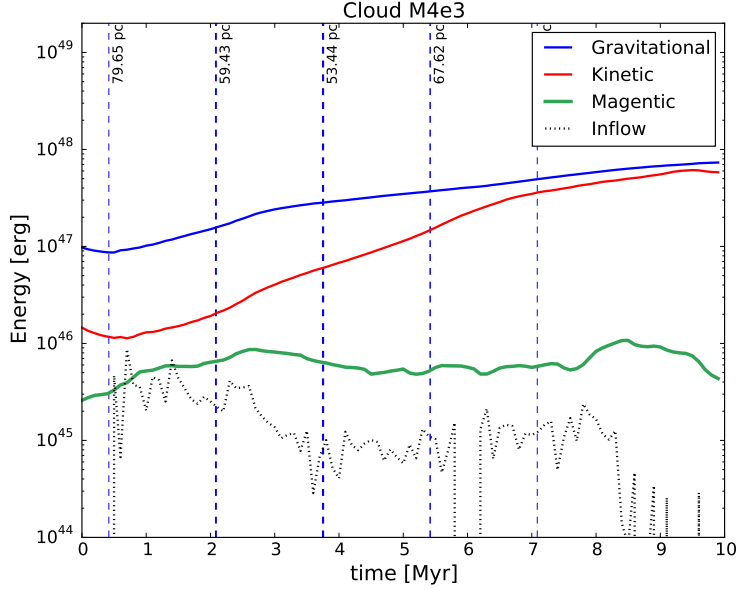


Figure 5.10: Evolution of the total (*solid blue line*) gravitational potential, (*solid red line*) kinetic and (*solid green line*) magnetic energies in the cloud. The (*dotted black line*) total amount of kinetic energy entering the cloud through the accretion flow between snapshots ($\Delta t = 0.1$ Myr) is displayed, as well as the locations of nearby SN events (*vertical dashed blue lines*) at their explosion times, the thickness of the line is related to the distance of the cloud’s center of mass to the SN.

has doubled the amount of gas available to participate in the formation of stars.

M8e3 Cloud

M8e3 has a very interesting evolutionary history, as it is shocked by several nearby SN explosions that have a major impact on the cloud and its envelope. This cloud has an initial mass of $M = 7.5 \times 10^3 M_{\odot}$ and a virial parameter of $\alpha_{vir} = 0.3$. It is initially located at $(x, y, z) = (65, 359, 21)$ pc and has a bulk velocity of $\vec{v} = (1, -1, -1)$ km s $^{-1}$ that remains roughly constant during its subsequent evolution.

The first nearby SN explodes at time $t = 0.62$ Myr at $\vec{d} = (-29, 14, -30)$ pc. This SN shocks the cloud envelope $\Delta t \approx 0.2$ Myr, later, and triggers an increased mass accretion rate that lasts for over a megayear (see Fig. 5.11).

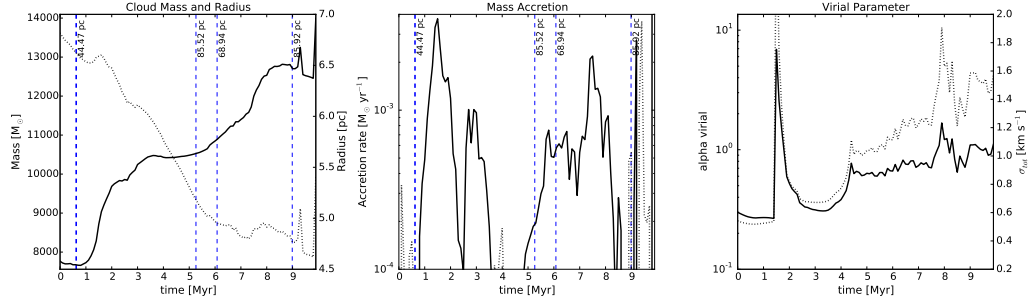


Figure 5.11: Evolution of the properties of the cloud M8e3 starting with the inclusion of self-gravity and tracer particles. *Left to right*: First: evolution of the cloud mass and radius as a function of time. Vertical dashed blue lines mark nearby SN explosions along with their distance to the cloud’s center of mass. The thickness of these lines is related to this distance. The line is thicker the closer the SN exploded. Second: Mass accretion rates as a function of time. Solid black line correspond to positive accretion rates, and dashed black line shows mass decretion rate. Red lines correspond to the predicted accretion rates given equation 5.4 for different ISM densities. Vertical blue lines show the nearby SN events. Third: Cloud virial parameter evolution.

There is a steep rise in the cloud mass between $t = 1.1$ – 2.0 Myr reaching mass accretion rates up to $\dot{M} \approx 4 \times 10^{-3} M_{\odot} \text{ yr}^{-1}$. Although the cloud continues accreting mass at times between $t = 2$ – 3.5 Myr, a lot of mass is simultaneously torn off of the cloud on the side opposite to the SN explosion. Because of the sudden accretion of fast moving material, the virial parameter of the cloud jumps to $\alpha_{vir} \approx 8$. Some of this gas becomes part of the cloud and shares its kinetic energy with the gas in the cloud, but a large fraction of material is also eroded from the cloud, and big cloud fragments break up, so, as one might expect, the high virial number leads to quick dispersion of the unbound material. Furthermore, any turbulence induced in the dense part of the cloud decays in a crossing time (Mac Low, 1999), further contributing to the fast drop of the virial parameter. This nearby explosion also plays a key role in perturbing the envelope, quickly pushing it onto the cloud or clearing it. This leads to a low accretion rate period between $t = 3.5$ – 5.5 Myr, during which the cloud just contracts gravitationally. At $t = 5.26$ Myr, a second nearby SN blows up above the cloud, at $\vec{d} = (-33, -69, 38)$ pc. While the SN shock front moves down towards the cloud, a third SN below the cloud explodes at $t = 6.02$ Myr, at $\vec{d} = (32, 3, -61)$ pc. These two subsequent SN explosions coming from opposite directions compress the cloud

and its remaining envelope, delivering another rush of mass to the cloud. At times between $t = 5.5\text{--}7$ Myr, the cloud accretes material at a rate of $\dot{M} \approx 5 \times 10^{-4} M_{\odot} \text{ yr}^{-1}$. Then a sudden jump in the cloud mass and accretion rate at $t \approx 7.4$ Myr occurs when the cloud captures a large fragment of dense gas from the infalling envelope. During the entire time, the cloud is gravitationally contracting, shrinking in size and reaching higher and higher peak densities. This contraction converts gravitational potential energy into kinetic energy, evident in the increase of the virial parameters towards values of order unity.

Instantaneously Accreted Gas: Cloud M8e3 shows large fluctuations in the accretion rate, number of accreted particles, and the densities and velocities of these accreted particles. The first blast wave shocking the cloud is at $t \approx 1$ Myr, when a burst of fast moving, low density gas is accreted onto the cloud. The mass accreted onto the cloud also shows two stages of accretion after the nearby explosion, as in cloud M3e3. There is again a short stage during which fast moving material is accreted onto the cloud, and the envelope is compressed, followed by a longer-lived phase during which the compressed, dense envelope falls onto the cloud at slightly lower velocities. However, for this cloud, in particular, the first explosion cleared the envelope on the side facing the SN, exposing the cloud surface to the low-density, turbulent environment. This results in an extended stage of accretion of low-density gas, lasting until $t \approx 1.8$ Myr.

Following this active period, the cloud goes through a period of low accretion that lasts roughly 4 Myr. During this time, cloud M8e3 mostly accretes gas that slowly climbs up the density gradient and becomes part of the cloud. This gas, however, is highly turbulent, with mean perpendicular velocities, similar to the velocity expected purely from gravitational infall and only a small dispersion around the mean.

At the end of this period, two nearby SN explosions trigger another accretion burst, compressing the cloud and its envelope, as a large fragment of dense gas joins the cloud. The captured fragment just became gravitationally bound, and moves at speeds close to the velocity expected from gravitational infall. However this event is difficult to pick up from these figures as there is no obvious signature of the parallel or perpendicular velocity components expected from such an event.

Looking at the overall behavior of the parallel and perpendicular velocities of the accreted gas, we notice that the perpendicular velocity is systematically higher than the parallel velocity throughout the evolution. This suggests that the accretion of gas onto this cloud is mostly due to gas delivered by

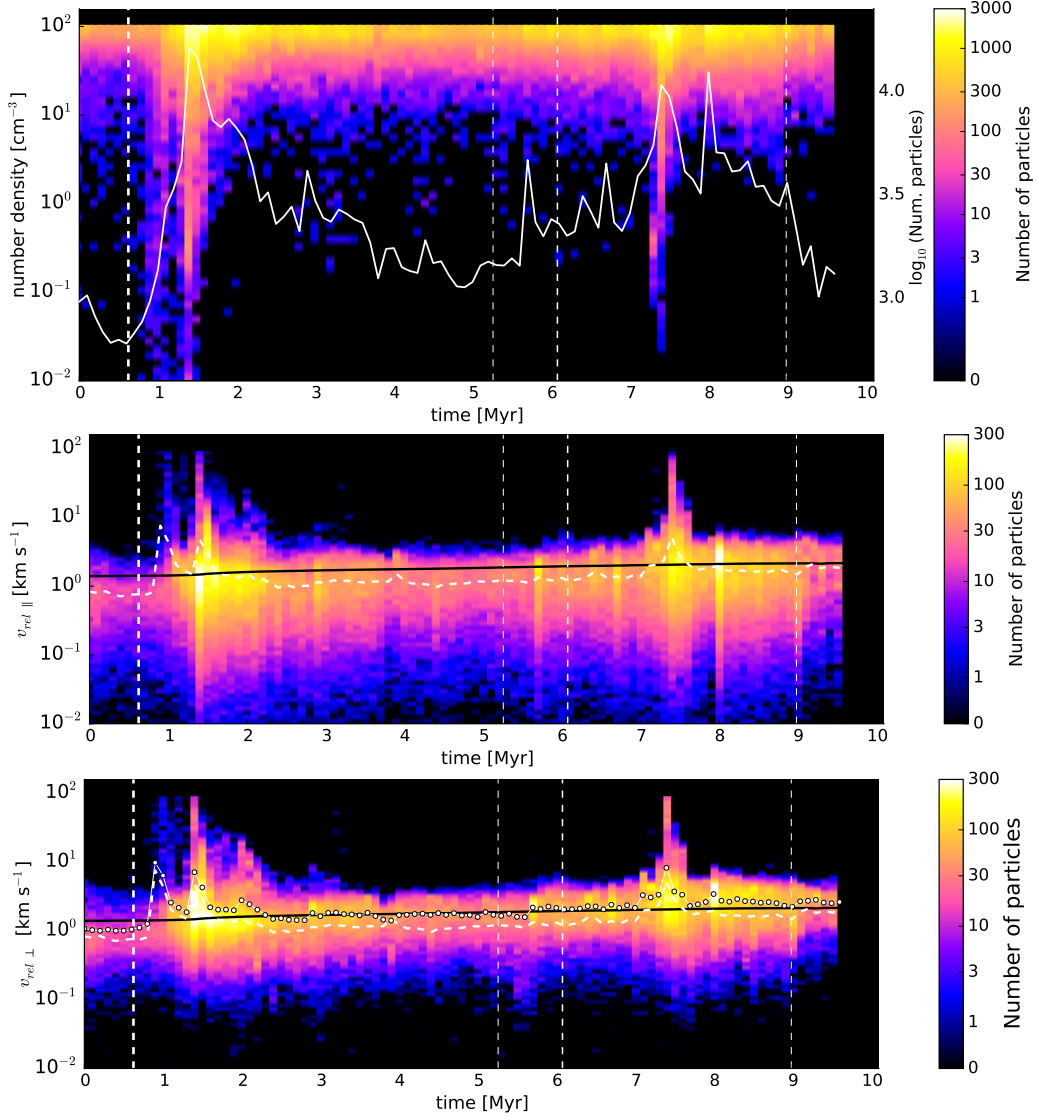


Figure 5.12: Instantaneous accretion onto cloud M8e3. Properties of the accreted gas at the snapshot before being accreted onto the cloud ($\Delta t = 0.1$ Myr). a) Number density at the location of the tracer particle. The solid white line shows the total number of tracer particles accreted at each time. The next two panels show the local velocity of the gas relative to the cloud's center of mass velocity, the solid black line shows the predicted infall velocity driven by self-gravity (eq. 5.2): b) Relative velocity parallel to the density gradient. The dashed line in this and the next panel gives the mean parallel velocity at each bin. c) Relative velocity perpendicular to the local density gradient. The dotted line gives the mean perpendicular velocity.

the turbulent environment and not only due to the gravitational collapse of the envelope. This turbulent accretion rate shows large velocity fluctuations, particularly after the explosion of a nearby SN.

Global Evolution of Accreted Gas: Figure 5.13 shows the global evolution of ten randomly selected particles from cloud M8e3. Out of the ten particles, one is already part of the cold envelope, one is part of the warm environment, and the rest of the particles are in the hot environment close to the location of the SN explosion. Although most of these particles are moving at velocities of $\sim 10\text{--}100\text{ km s}^{-1}$, their associated Mach numbers are low, $\mathcal{M} < 1$, because they are embedded in hot gas.

At the moment the nearby SN blows up at $t = 0.6\text{ Myr}$, most of the particles in the hot phase are pushed towards the cloud, quickly climbing up the density gradient. As these particles move to denser environments, both their parallel and perpendicular velocities drop to lower values, while their Mach numbers climb, reaching values of order unity.

Some of these particles continue on to quickly join the cold envelope and then become part of the cloud. However, as previously discussed, nearby SN explosions have the dual role of compressing the cloud but also eroding the envelope. For this reason, some of the particles in the cloud's envelope move back to lower density environments. As seen in Figure 5.11, following this sudden accretion phase, M8e3 goes through a low accretion phase that lasts $\sim 4\text{ Myr}$, until two new nearby SN, on opposite sides of the cloud, blow up. These nearby events compress the envelope, increasing the mass accretion rate of the cloud, characterized by the accretion of material at supersonic velocities, reaching Mach numbers of $\mathcal{M} \approx 10$.

Evolution of the Cloud Energetics: Figure 5.14 shows the global energetics of cloud M8e3 and their evolution. The gravitational potential energy dominates over most of the evolution of the cloud. However, in comparison to the other clouds, there is a major injection of kinetic energy from the accreted gas after the first nearby SN explosion. This inflow of kinetic energy is more than an order of magnitude stronger than the total binding energy of the cloud and is deposited in the cloud as this fast moving gas quickly thermalizes in the cloud. Right after the inflow of this energy, the kinetic energy rises up to values higher than the gravitational potential energy of the cloud. However, instead of breaking apart the entire cloud, the excess kinetic energy breaks up fragments of the cloud and its envelope, and quickly decays in a crossing time. At later times, the cloud continues contracting gravitationally without significant accretion. During this time the kinetic energy of

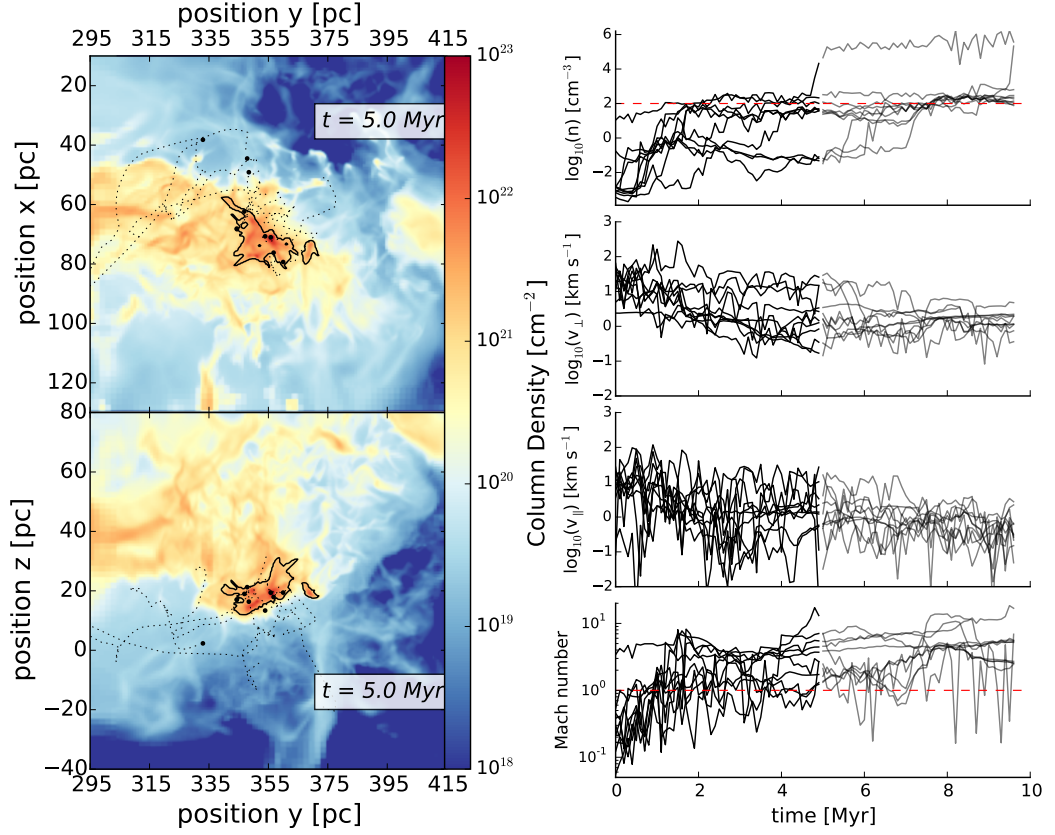


Figure 5.13: Global evolution of selected particles accreted by cloud M8e3. *Left:* Column density projection of cloud M3e3 along lines of sight (top) perpendicular and (bottom) parallel to the midplane. The solid black contour follows the projected surface of the cloud. Both panels include the location of ten randomly selected particles and their trajectories from the moment of injection up to the current time. *Right:* Four panels showing the dynamical properties sampled by each of the ten particles shown in the column density projections at each time in their evolution. Panels show (*top*) local number density traced by the particles during the ~ 10 Myr of evolution. The horizontal dashed red line indicates the density threshold defined for the cloud. (*second and third*) Velocity of the particles perpendicular and parallel to the local density gradient. (*fourth*) Mach number of the particles calculated using the local adiabatic sound speed of the gas and with respect to the center of mass of the cloud. A dashed red line shows the sound speed. An animation of the full 10 Myr evolution of this figure can be found online.

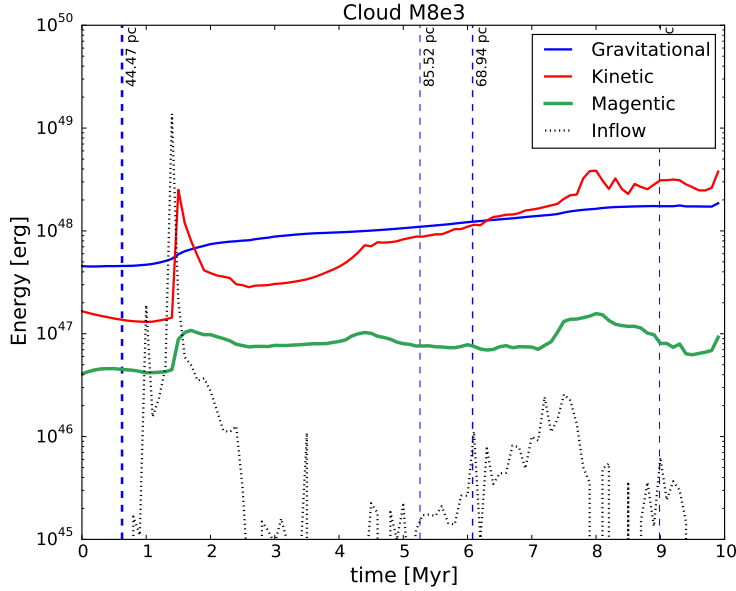


Figure 5.14: Evolution of the total (*solid blue line*) gravitational potential, (*solid red line*) kinetic and (*solid green line*) magnetic energies in the cloud. The (*dotted black line*) total amount of kinetic energy entering the cloud through the accretion flow between snapshots ($\Delta t = 0.1$ Myr) is displayed, as well as the locations of nearby SN events (*vertical dashed blue lines*) at their explosion times, the thickness of the line is related to the distance of the cloud’s center of mass to the SN.

the cloud increases steadily as the cloud converts gravitational energy into kinetic energy during this contraction. Two new nearby SN explosions cause enhanced accretion rates onto the cloud, but these new events are less dramatic and drive a much lower inflow of energy into the cloud, barely affecting the total kinetic energy of the cloud. The magnetic energy remains below both the gravitational potential and the kinetic energy of the cloud, unable to prevent the cloud from collapsing.

5.5 Interpretation and Discussion

The simulations presented here suggest that mass accretion onto molecular clouds is an essential part of a cloud’s life. These accretion flows not only increase the available mass of the clouds to form stars, but also carry a significant amount of kinetic energy that affects the cloud’s evolution.

In Section 5.2 we analytically calculated that the mass accretion rate onto molecular clouds should correlate with the cloud mass, not just because of the increase in the gravitational pull resulting from the increase in mass, but also because of the increased surface area for the gas to flow in. We then showed mass accretion rates for a simulated cloud population evolving in a realistic galactic environment and observed a correlation of the accretion rates with both the cloud mass and surface area. Comparing simulations with and without the effects of gas self-gravity, showed that for a wide range of masses the accretion rates driven by random turbulent flows and by gravitational attraction seem to be indistinguishable, but for the most massive clouds with $M > 10^5 M_{\odot}$, the infall of gravitationally bound gas onto the cloud dominates the accretion rates. This is the range where both the calculated and simulated accretion rates come in to agreement with the mass accretion rates observed for GMCs in the LMC by Fukui et al. (2009); Kawamura et al. (2009b), and Fukui & Kawamura (2010).

Simulating the evolutionary history of individual low-mass clouds with initial masses in the range $3\text{--}8 \times 10^3 M_{\odot}$, we find that the mass accretion rates fluctuate on timescales of order the crossing time or less because of the disturbance of the gas reservoir by the turbulence in the environment. As clouds accrete from a non-uniform, dynamic envelope, nearby SN explosions can simultaneously promote and prevent the inflow of mass onto the cloud by compressing and disrupting different parts of their envelope. After a nearby SN explosion, a period of high accretion rate is observed, carrying a large influx of kinetic energy into the cloud, followed by a period of low accretion as the envelope has been either deposited onto the cloud or puffed up and eroded. It appears that the gravitational collapse of the envelope, gas sweeping, and turbulent accretion have similar influence on the mass accretion rates over the entire lifetime of these low-mass clouds, where gas seems to flow in with velocities close to the free-fall velocities at the edge of the cloud.

When we try to understand what controls the global evolution of these clouds, we focus on the time variation of the fractions of energy stored in the form of gravitational potential, kinetic, and magnetic energy, compared to the influx of kinetic energy from accretion. We see that the gravitational potential energy is the dominant form of energy in the clouds during their entire evolution, ultimately determining the fates of these clouds. The Kinetic energy for all the clouds starts at low values, probably due to the lack of gas self-gravity during their initial assembly, but it climbs from the moment self-gravity is turned on, increasing the internal velocity dispersion of the clouds, as seen in Figures 5.3, 5.7 and 5.11, until it reaches values approaching that of the gravitational potential energy, as expected for gravitationally

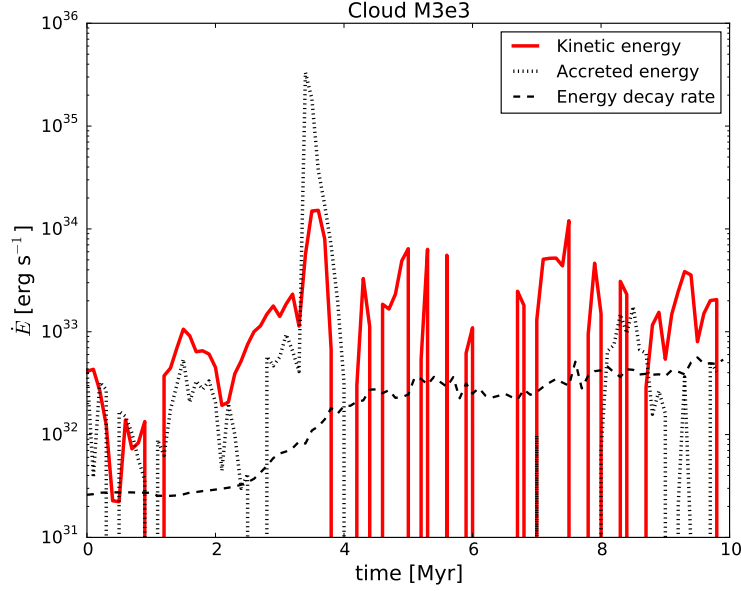


Figure 5.15: Rate of change of cloud’s M3e3 internal (*solid red line*) kinetic energy, compared to the energy influx rate from the (*dotted black line*) accretion flows, and the predicted (*dashed black line*) energy decay rate of the supersonic turbulence given by equation 5.11

dominated, out of equilibrium clouds (Vázquez-Semadeni et al., 2007, 2008; Ballesteros-Paredes et al., 2011; Naranjo-Romero et al., 2015). The influx of kinetic energy from accretion is lower than both the gravitational potential and kinetic energy, but in isolated, special cases, when there is a nearby SN explosion in a confined environment allowing it to deposit a lot of energy into the cloud, the influx of kinetic energy from the accreted material can exceed both the kinetic and gravitational binding energy of the cloud. In these cases the incoming energy is deposited into the cloud, where some of the fast-moving material detaches from the cloud, while the rest of the excess is quickly radiated away due to the short decay time for supersonically turbulent gas (Mac Low et al., 1998; Stone et al., 1998).

Figures 5.15–5.17 show the rate of increase of the kinetic energy in the cloud, compared to the inflow of kinetic energy from the accretion flow, and the predicted decay rate of energy given the cloud mass, size and velocity dispersion from equation 5.11. For all three clouds, the energy deposited onto the cloud by accretion is systematically higher than the predicted decay rate of the internal turbulence, making accretion driven turbulence a strong

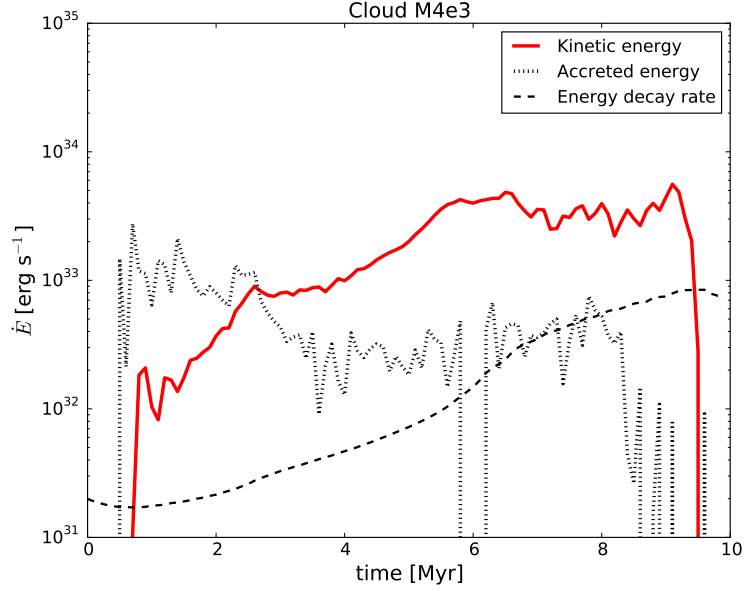


Figure 5.16: Rate of change of cloud’s M4e3 internal (*solid red line*) kinetic energy, compared to the energy influx rate from the (*dotted black line*) accretion flows, and the predicted (*dashed black line*) energy decay rate of the supersonic turbulence given by equation 5.11

candidate for maintaining the fast turbulent motions observed in MCs. Furthermore, most of the time the inflow rate of kinetic energy is comparable to the rate of change of the kinetic energy of the cloud, although systematically lower, suggesting that it can not be the only source driving this motions. Ultimately, the continued contraction and final collapsed state of the three clouds suggests that gravitational contraction dominates the evolution of these clouds during this 10 Myr of evolution.

We do not include internal feedback from star formation in collapsing regions in our simulations, which has been argued to constitute one of the main energy sources for preventing runaway cloud collapse, maintaining the clouds in a quasi virial equilibrium state (Goldbaum et al., 2011; Zamora-Avilés et al., 2012), and maintaining the level of star formation within the observed range. Instead, we stop our simulations once the majority of the mass in our cloud has collapsed to unresolved structures and should undergo fast star formation.

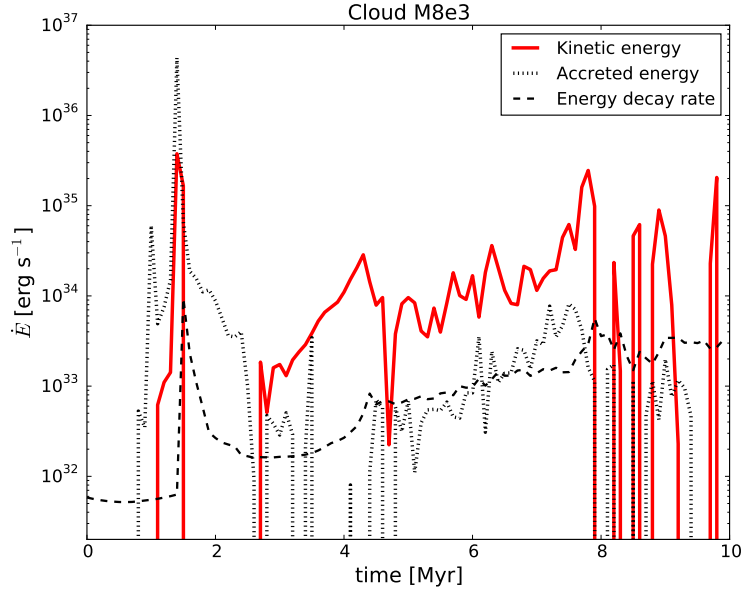


Figure 5.17: Rate of change of cloud’s M8e3 internal (*solid red line*) kinetic energy, compared to the energy influx rate from the (*dotted black line*) accretion flows, and the predicted (*dashed black line*) energy decay rate of the supersonic turbulence given by equation 5.11

5.6 Conclusions

The non-linear interplay between gravitational pull, turbulence, and magnetic fields determines the evolution and collapse of MCs (Mac Low & Klessen, 2004; Dobbs et al., 2014; Gnedin et al., 2015). The origin of the turbulent motions inside dense clouds and whether they are strong enough to prevent the clouds from collapsing remains poorly understood. Observations show that molecular clouds have supersonic internal velocity dispersions (Zuckerman & Palmer, 1974), with kinetic energies comparable to the gravitational potential energy of the clouds (Larson, 1981; Solomon et al., 1987; Heyer et al., 2009).

It has been proposed that the process of mass growth in molecular clouds can drive sufficiently strong internal motions to explain the observations (KH10). However there are few observations quantifying mass accretion rates, while theoretical studies to date have relied on semi-analytic methods using efficiency parameters tuned to reproduce the observations (Goldbaum et al., 2011). Some of the best evidence for mass growth in MCs comes

from the observations by [Fukui et al. \(2009\)](#) and [Kawamura et al. \(2009a\)](#), who matched observed GMCs in the LMC with their internal level of star-formation, deriving an evolutionary sequence for GMCs and recovering an average mass accretion rate.

We present here a set of numerical simulations of the evolution of a cloud population in a galactic environment, along with zoom-in re-simulations for three moderate-mass clouds from this population in order to resolve the interaction between the turbulent environment and such clouds as they collapse. We ask the question of what physical process drives the observed mass accretion rates and how much kinetic energy is deposited into the cloud due to the accretion flow. Finally we compare the influx of kinetic energy due to accretion to the rate of change of cloud kinetic energy and its rate of turbulent decay in order to determine what drives the turbulence in these clouds.

We find:

- Molecular clouds accrete gas from highly inhomogeneous envelopes, with accretion rates often fluctuating by several orders of magnitude over timescales shorter than a crossing time.
- Nearby SN explosions impacting clouds play a dual role in their accretion histories, on one hand compressing part of their envelopes, instantaneously increasing the accretion rates, but also disrupting other parts of the cloud and envelope, resulting in extended periods of low or even negative mass accretion rates.
- The influx rate of kinetic energy into clouds via accretion flows appears to be sufficient to balance the turbulent decay rate of kinetic energy within them ([Klessen & Hennebelle, 2010](#)).
- The more massive the clouds, the more strongly they are gravitationally dominated, with gravitational collapse ultimately responsible for the fate of massive clouds.
- The conversion of gravitational potential energy into kinetic energy through the hierarchical contraction of the cloud is responsible for driving the fast turbulent motions inside the clouds, maintaining them in a state of near balance between potential and kinetic energy but not virial equilibrium, as emphasized by [Ballesteros-Paredes et al. \(2011\)](#)

Chapter 6

Gravitational Contraction vs. Magnetic Fields

The co-authors of this study are Mordecai-Mark Mac Low and Ralf S. Klessen (manuscript in preparation).

6.1 Motivation

Understanding the relative importance of magnetic fields in the formation, evolution, and collapse of molecular clouds, as well as their envelopes, is critical for understanding star formation.

Magnetic fields have been continuously invoked in studies of the ISM in order to explain its properties. Proposals have ranged from strong organized magnetic fields on galactic scales regulating the formation of GMCs (Parker, 1979), to strong magnetic fields in the interior of MCs maintaining them as magnetically supported structures (Mouschovias & Spitzer, 1976) that collapse only under the mediation of ambipolar diffusion (Mouschovias, 1977; Shu, 1977). Zeeman splitting observations tell us the magnetic field strengths along the line of sight for density ranges depending on the observed tracer molecule (Crutcher et al., 1975; Heiles & Troland, 2004; Falgarone et al., 2008). Polarization observations give us information about the projected orientation of the field in the plane of the sky (Lazarian, 2007; Andersson et al., 2015), and, in combination with assumptions about the nature of the turbulence, also give estimates of their strength using the Chandrasekhar-Fermi (Chandrasekhar & Fermi, 1953a) method (Heitsch et al., 2001b; Padoan et al., 2001; Houde et al., 2009).

Numerical simulations can help us to determine the relative importance of magnetic fields with respect to the other dominant physical processes in

the ISM. However, most simulations until now are either restricted to small volumes around dense clouds, or do not simultaneously include magnetic fields, realistic turbulence driving from SN explosions, and gas self-gravity.

In this chapter we explore the dynamical importance of magnetic fields in the dynamics of the ISM ranging from scales of ~ 100 pc, down to ~ 0.1 pc, and densities ranging from $10^{-2} - 10^4$ cm^{-3} . We analyze the relative importance of magnetic fields for constraining gas flows inside and around dense clouds, as well as the orientation of the magnetization relative to the density distribution. We show how the gas flows transition from trans-Alfvénic to super-Alfvénic as gravity takes hold of dense structures, permitting hierarchical gravitational contraction. We find that magnetic fields can constrain flows in cloud envelopes, but cannot support dense clouds from collapsing.

6.2 Methods

We present results from the same set of simulations presented in the previous chapter, but we focus our detailed analysis on cloud M3e3, as it is the highest resolution cloud that we simulated.

The details of the simulation are described in Chapter 3, including the initial conditions and the techniques implemented to develop the turbulent initial conditions, while the details of the high-resolution, zoom-in, re-simulation and the detailed evolution of the hierarchically collapsing cloud are found in Chapter 5.

6.3 Analysis tools

In this section we describe the tools we implemented to analyze the relative importance of magnetic fields in and around the cloud. We first compare observed magnetic field strengths to the magnetic field strengths measured in the simulations in the diffuse ISM and in the interior of collapsing clouds. We then use the histogram of relative orientations (HRO) described by Soler et al. (2013), to analyze the angle between the magnetic field direction \hat{B} and the density gradient $\hat{\nabla}n$. We further measure the relative orientations between the magnetic field and the velocity of the flow \hat{v} , and between the density gradient and the velocity. Finally we calculate the total energy of the system and its partition into kinetic, magnetic, thermal, and gravitational potential energy. We pursue our analysis across the range of densities, in order to determine how strongly magnetic fields constrain the flow and prevent collapse in cloud cores and envelopes.

6.3.1 Magnetic Field-Density Relation

Observations of magnetic fields in diffuse and dense molecular clouds suggest that the magnetic fields are dynamically important for gas with $n < 300 \text{ cm}^{-3}$. This result is often interpreted as the velocity being forced to follow magnetic fields at these densities. At higher densities, $n > 300 \text{ cm}^{-3}$, dense molecular clouds seem to be predominantly gravitationally bound, with the gas dragging the magnetic fields along as the cloud contracts (Heiles & Crutcher, 2005; Heiles & Troland, 2005).

We explore a $\vec{B} - n$ scatter plot of our model that resolves the entire midplane at 0.95 pc resolution in order to understand the interplay between the turbulent ISM and the field strength. We then explore the $\vec{B} - n$ plot over time of the high resolution cloud M3e3 to investigate the correlation between the magnetic field strength and the density in a collapsing cloud.

6.3.2 Energetics

We are interested in understanding what processes dominate the evolution of a cloud and its environment at different stages of the cloud's evolution. To do this, we explore the balance between the different forms of energy in the cloud and its environment as a function of density over time. This knowledge, along with the $\vec{B} - n$ relation, reveals the dominant energies of the gas inside and around a cloud.

We calculate the total magnetic, gravitational, thermal and kinetic energies as a function of density, with respect to the cloud's center of mass and bulk velocity,

$$e_{tot}(n) = e_m(n) + e_k(n) + e_{th}(n) + e_{pot}(n). \quad (6.1)$$

By definition, the only energy density that gives a negative contribution to the total energy is the gravitational potential energy. Therefore, whenever the total energy is positive, it is dominated by some combination of kinetic, thermal, and magnetic energy, and whenever the total energy is negative, it is gravitationally dominated.

6.3.3 Characteristic Velocities

Comparing the different characteristic velocities of the system, including the sound speed, Alfvén speed, and turbulent rms velocity v_{rms} provides information about how the gas responds to perturbations. We investigate the variation of these velocities as a function of density and time, in order to gain an understanding of how the system reacts as the dense gas contracts.

We are interested in both the sonic Mach number, $\mathcal{M} = v_{rms}/c_s$, the ratio of the rms velocity to the sound speed, and the Alfvénic Mach number, $\mathcal{M}_A = v_{rms}/v_A$, the ratio of the rms velocity to the the Alfvén speed.

Supersonic turbulence with $\mathcal{M} > 1$, characteristic of the ISM ([Mac Low & Klessen, 2004](#)), leads to large density fluctuations, as isothermal shocks produce density increases $\Delta n \propto \mathcal{M}^2$. Super-Alfvénic flows have the capability of moving gas perpendicular to the magnetic fields, leading to strong fluctuations of the magnetic field strength, as the field gets compressed by the shock along with the gas.

6.3.4 Relative Orientation of Velocity and Magnetic Field

The relative orientation between the local velocity and the magnetic field is computed by measuring the angle

$$\phi_{\hat{v}\hat{B}} = \cos^{-1} \left(\frac{|\vec{v} \cdot \vec{B}|}{|v||B|} \right). \quad (6.2)$$

Measuring the relative angle between the magnetic field and the velocity together with the total energy measurements and the characteristic velocities can tell whether gas flows are restricted to follow field lines, or whether magnetic fields are just being advected by the turbulence.

6.3.5 Histogram of Relative Orientation

The HRO allows us to compare the density structure with the magnetic field morphology. It has been used to analyze observations by [Soler et al. \(2013\)](#). The HRO is computed by measuring the relative angle between the local density gradient and the magnetic field:

$$\phi_{\hat{n}\hat{B}} = \cos^{-1} \left(\frac{|\vec{\nabla}n \cdot \vec{B}|}{|\nabla n||B|} \right) \quad (6.3)$$

Note that we compute the dot product between the magnetic field and the density gradient here, as opposed to the cross product used by [Soler et al. \(2013\)](#). We make this choice in order to find the relative orientation of the field to the density gradient, instead of isochoric contours.

Once the relative angles have been computed everywhere in the model, we collect this data into a histogram to determine any preferred orientation angle. We proceed to bin the results with respect to the density, in order

to explore the behavior of these relative orientations for a wide range of environments. Density bins are chosen such that we have at least 10^3 pixels in each density bin. Given that we perform our study of the HRO for physical scales over the range 0.1–100 pc in an AMR simulation, we do not force our density bins to have equal numbers of pixels, but rather force a minimum number pixels per bins to have a well sampled distribution of angles.

Finally, as we are interested in the dynamical evolution of the cloud as it collapses, we compute the time evolution of the HRO and the variations in the relative orientation at different evolutionary stages of the cloud collapse and discuss its time variation.

6.3.6 Relative Orientation of Gas Flows and the Density Structure

The histogram is computed by measuring the relative angle between the density gradient, and the velocity field:

$$\phi_{\hat{n}\hat{v}} = \cos^{-1} \left(\frac{|\vec{\nabla}n \cdot \vec{v}|}{|\vec{\nabla}n||v|} \right) \quad (6.4)$$

Observations suggest that gas should flow preferentially along field lines (Crutcher et al., 2010b), while numerical simulations suggest that magnetic fields are preferentially aligned perpendicular to density gradients (Soler et al., 2013). These two statements imply that gas should preferentially flow perpendicular to the density gradient. However, this geometry is counter-intuitive in the context of the accreting and collapsing clouds described in Chapter 5, where gas flows aligned with density gradients would be expected. We measure the HRO in order to try to reconcile the predictions from observations and simulations for an accreting, hierarchically collapsing cloud.

6.4 Results

We use the evolved state of the stratified-box simulations as the turbulent initial conditions in the simulations presented here. At this point we have a well-established, multiphase ISM, vertical gas stratification, and a galactic fountain up to ± 20 kpc (Hill et al., 2012). So far, 7515 SN have exploded in the simulation, and they continue to be injected in the subsequent evolution presented in this work. The simulation discussed here includes the action of self-gravity, and the analysis is performed from the moment $t_{SG} = 0$ when self-gravity is turned on.

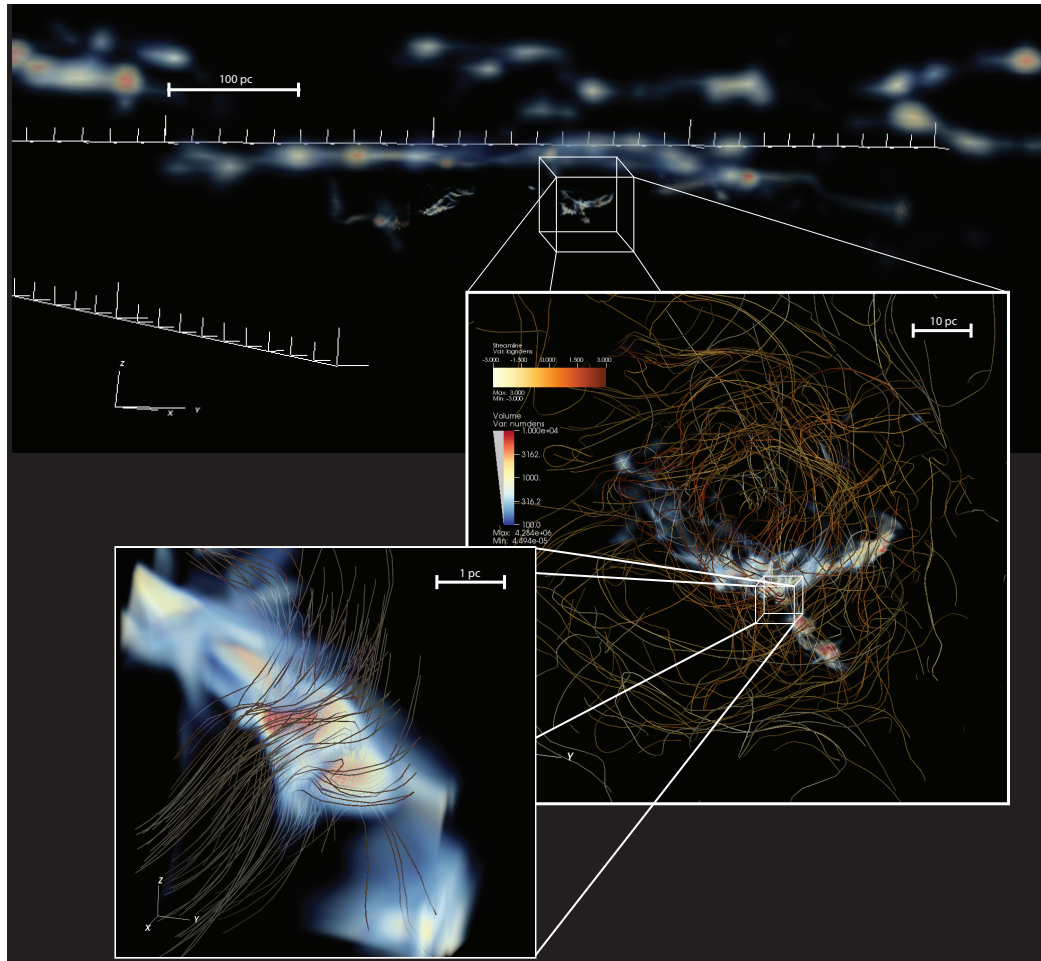


Figure 6.1: Three-dimensional rendering at $t = 5$ Myr of (*Top to bottom*) the galactic midplane for altitudes up to ± 50 pc above and below the midplane, close-up view of cloud M3e3, including with magnetic field lines for a volume of 50 pc^3 , and a second close up to a collapsing core with the magnetic field lines crossing a plane with area 2 pc^2 centered in the core center of mass.

Figure 6.1 shows a three-dimensional rendering of the all the gas above 100 cm^{-3} around the midplane, with the location of the high-resolution cloud, a close-up to the dense cloud, and a second close-up to a dense, collapsing core. The close-up view of the cloud includes 125 magnetic field lines which are highly tangled and twisted, penetrating the density structure down to the massive, collapsing cores.

We stop the simulations at an evolutionary time of $t \approx 10$ Myr, as it is expected that by this time the massive stars must already be feeding back energy in the form of radiation, winds, and SN explosions, which should influ-

ence not only the cloud properties but its environment. As we do not include self-consistent star formation and feedback in our simulations, running this setup for longer would lead to unphysical results.

In order to understand the role of the tangled magnetic fields seen in Figure 6.1 in the formation, evolution and collapse of dense molecular clouds in the ISM, we divide our analysis in four parts. In Section 6.4.1 we compare the magnetic field strength as a function of density for the diffuse and dense gas in the ISM, with and without gas self-gravity, and compare our measurements with Zeeman observations of magnetic field strengths of MCs in the Galaxy. In Section 6.4.2, we compare the distribution of the total energy of the gas in its different forms, magnetic, kinetic, thermal and gravitational, as a function of the gas density, in and around a collapsing cloud, in order to determine which physical process dominates the dynamics of the gas in a cloud and its envelope. In Section 6.4.4 we compute the relative orientation of the magnetic field to the velocity field, in order to establish how the magnetic field influences the flows of gas in the diffuse and dense phases of the ISM. Finally, in Section 6.4.5 we compare the relative orientation of the magnetic field strength and the density gradient inside the cloud in order to quantify the participation of magnetic fields in the structure and collapse of dense MCs.

6.4.1 B-n Relation

We first explore the distribution of magnetic field strength as a function of density in the diffuse ISM. We begin by examining the 0.95 pc model without self-gravity, to compare the relative role of magnetic fields with respect to the turbulence driven by SN explosions, and with respect to gas self-gravity for densities $n < 100 \text{ cm}^{-3}$. This simulation is ideal for this comparison as it resolves gas dynamics and resulting fragmentation, and the Nyquist frequency, up to densities of $n \approx 500 \text{ cm}^{-3}$.

Figure 6.2 shows mass and volume weighted plots of gas density for all zones close to the midplane versus the magnetic field strength, measured along an arbitrary line of sight. The multiphase structure of the ISM is reflected in the mass and volume concentrations at densities around $n = 10^{-3}, 10^{-1},$ and 10^2 cm^{-3} . In both the mass- and volume-weighted cases, the bulk of the gas has field strength $|\vec{B}_x|$ systematically below $10 \mu\text{G}$, the upper limit for the magnetic field strength derived from observations (Crutcher, 2012). A weak correlation between the magnetic field strength and the gas density is seen for densities below 0.1 cm^{-3} , a regime not explored by the Zeeman observations. For densities between $0.1\text{--}300 \text{ cm}^{-3}$, the magnetic field does not correlate with the gas density, in agreement with the observations.

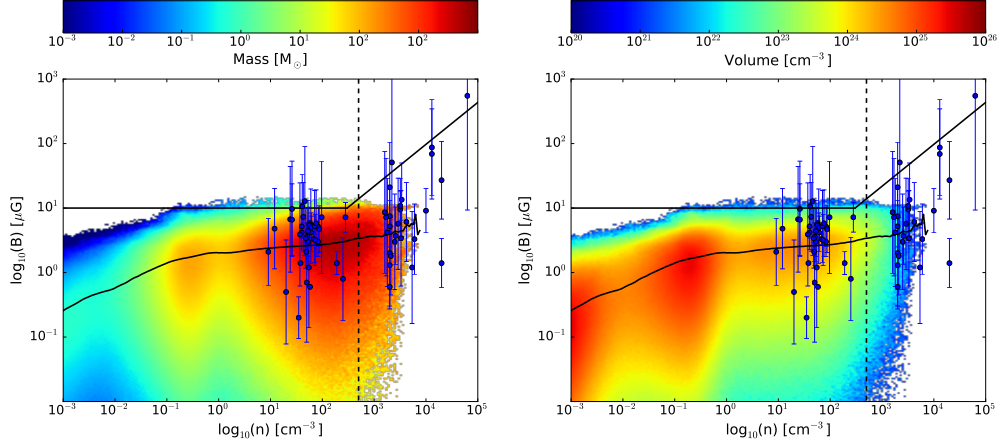


Figure 6.2: Density-magnetic field relation prior to the start of self-gravity. (*Left*) Mass-weighted and (*Right*) volume-weighted scatter plots of the line-of-sight magnetic field strength, measured along the line of sight parallel to the midplane in the x -direction, against the gas number density for gas within ± 50 pc above and below the midplane in the entire simulation. Blue points show Zeeman observations of line of sight magnetic field strengths for H I, OH and CN (Crutcher et al., 2010b, see references in). The upper solid black line shows the most probable model of the maximum field strength along a line of sight, as a function of density (Crutcher et al., 2010b). A vertical dashed line marks the maximum resolution at which we resolve the Jeans length with at least four cells. The lower solid black line gives the mean of the simulated values.

In order to analyze the magnetic field strengths in gravitationally dominated regions, we now look at the relation between field and density for our highest-resolution zoom-in re-simulation of a cloud. Figure 6.3 shows the field strength, along an arbitrary line of sight, vs the gas density for the collapsing cloud M3e3 at the moment self-gravity is turned on, and three later evolutionary times. This Figure also includes Zeeman observations towards diffuse and dense clouds compiled by Crutcher et al. (2010a) as well as the upper envelope of the magnetic field strength inferred from the observations. The observations show a notable change in behavior at $n = 300 \text{ cm}^{-3}$, where the envelope begins to climb as $|B| \propto n^{2/3}$. Although some of the gas in the simulation crosses this upper envelope, it is a small enough fraction of the gas that it appears likely to remain consistent with the limited number of observational samples.

As the cloud collapses, the gas flows towards the centers of collapse drag-

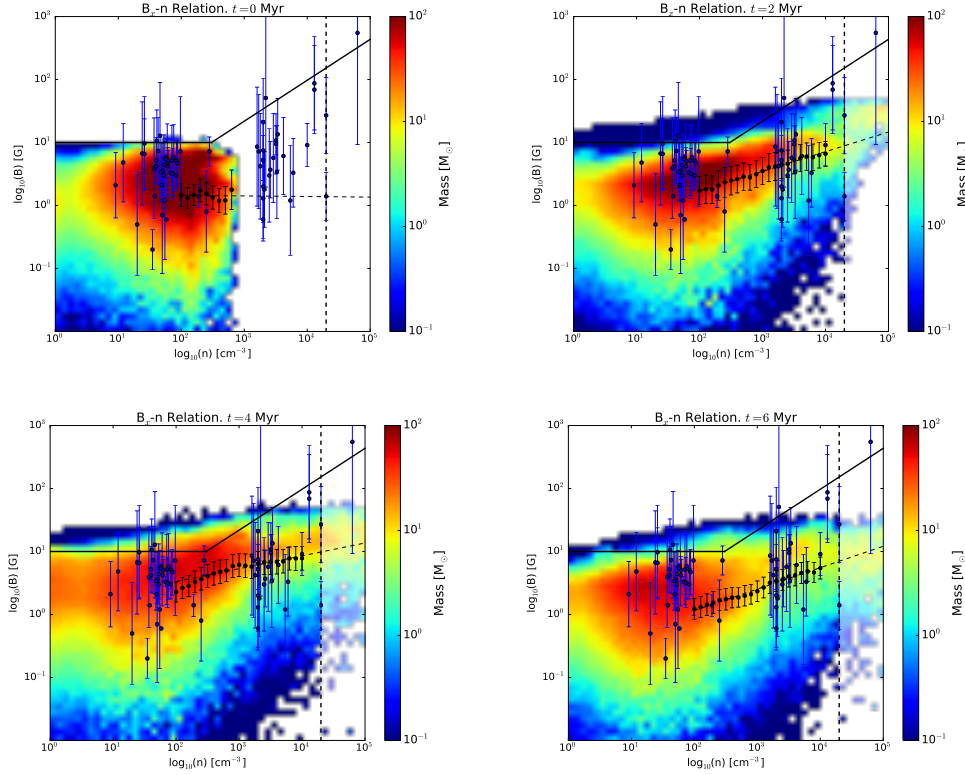


Figure 6.3: Scatter plots of the magnetic field strength along the x line of sight in the simulation versus the gas density in a 100 pc^3 volume centered in the cloud’s center of mass. The panels show evolutionary times of 0, 2, 4, and 6 Myr since the time self-gravity was included. Blue points give Zeeman observations of line of sight magnetic field strengths (observations compiled in [Crutcher et al., 2010b](#)). The solid black line shows the most probable model of the maximum field strength along a line of sight, as a function of density ([Crutcher et al., 2010b](#)). A vertical dashed line marks the maximum resolution at which we resolve the Jeans length with at least four cells. The black line with error bars gives the mean and dispersion of the simulated values.

ging the magnetic field along. A correlation between the magnetic field strength and the gas density is evident for densities above 100 cm^{-3} .

Assuming the field strength indeed behaves as described by an equation like

$$B_{los} = B_0 \left(\frac{n}{n_0} \right)^\alpha, \quad (6.5)$$

we calculate the mean magnetic field strength as a function of density, and

t	α
0	0.00
2	0.31
4	0.20
6	0.34

Table 6.1: Slopes α recovered from the magnetic field strength-density relation from the high-resolution simulation for densities of $100 - 2 \times 10^4 \text{ cm}^{-3}$ at times t in megayears from the time self-gravity was included in the simulations.

fit a power law to the field strength for densities between $100 - 2 \times 10^4 \text{ cm}^{-3}$. We measure the slope of the average field strength-density relation for the different evolutionary times, α_t .

We find that the slope of the B-n relation fluctuates with time, ranging from values as low as 0.20, to a maximum slope of 0.34. Although, we recover shallower slopes than $2/3$, it remains to be determined if the upper envelope of simulated observations of our results would be correspondingly shallower. Unfortunately, our resolution is not high enough to give us substantial dynamic range in the regime where maximum magnetic fields increase with density.

6.4.2 Energetics

In order to understand more quantitatively how the magnetic field affects the flows of diffuse and dense gas, we compute the evolution in time of the contribution of the different types of energy to the total energy of the cloud, as shown in Figure 6.4. This provides a picture of what physical processes can affect the dynamics of the dense and diffuse gas at different stages of the cloud's evolution.

At every time in the evolution of the simulation, the kinetic energy dominates the energy of gas with density below $n \approx 100 \text{ cm}^{-3}$. The thermal energy peaks at a density of $n \approx 0.1 \text{ cm}^{-3}$ and decreases at higher densities as temperatures drop. The magnetic energy is lower than the kinetic energy at all times, and is maintained at a fraction of $0.1 - 0.3$ of the total kinetic energy, probably due to the saturation of the small scale turbulent dynamo in our simulation box (Balsara et al., 2004; Meinecke et al., 2014).

As the simulation evolves, the gas above $n \approx 100 \text{ cm}^{-3}$ is dominated by gravitational potential energy, implying that the cloud is gravitationally bound and in a state of hierarchical contraction, not supported by turbulent,

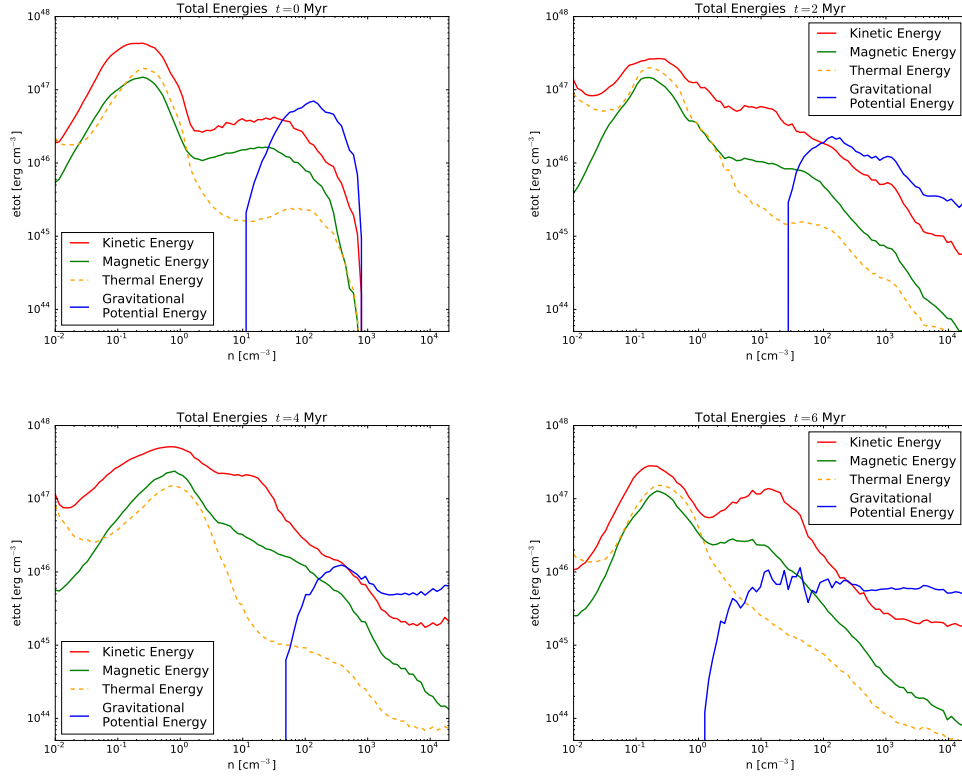


Figure 6.4: Total energy contained in the gas within a $(100 \text{ pc})^3$ box, centered in the cloud’s center of mass, along with the amount in gravitational potential, magnetic, thermal, and kinetic energy as a function of density for four snapshots at $t = 0, 2, 4$ and 6 Myr since the time self-gravity has been turned on.

magnetic, or thermal energy. As the cloud contracts (Figs. 6.4b,c,d), gas flows towards local centers of collapse. These increase in density, resulting in a rise of the gravitational potential energy at higher densities, followed by a rise of the kinetic energy as the gas gains velocity falling down the gravitational potential wells.

The kinetic energy within dense regions remains at a fraction 0.2–0.5 of the gravitational potential energy, closely following its density distribution. This supports our hypothesis (Chapter 4) that hierarchical contraction drives the fast, non-thermal, motions of the dense gas in the cloud. The magnetic field energy also increases as the cloud contracts, as field lines are compressed in local centers of collapse. However, magnetic energy does not grow as fast as kinetic energy, suggesting that a significant amount of gas moves along

field lines.

At densities corresponding to the envelope material of the cloud, $1\text{--}100\text{ cm}^{-3}$, the kinetic energy contributes the majority of the total energy followed by the magnetic energy. This suggests that the envelope should be supported against gravitational collapse and accretion onto the cloud should proceed generally preferentially along the magnetic field lines. A notable exception is if, at some time, most of the kinetic energy is oriented perpendicular to the local magnetic field, as can occur for an incoming SN blast wave, so that the field is compressed by the flow.

At low densities, $10^{-2}\text{--}1\text{ cm}^{-3}$, large variations in the kinetic and thermal energies are observed. This occurs because we perform our analysis in a 100 pc^3 box, with open boundaries to a turbulent, multiphase, ISM. The inflow and outflow of blast waves and rarefied gas from nearby SN explosions is the main cause for these large fluctuations of both kinetic and thermal energies, while the magnetic energy shows rather smaller variations around its initial configuration. The peak of the magnetic energy shifts to slightly higher and lower densities as gas is compressed and stretched. However, its relative invariance suggests that it is being maintained by the turbulent dynamo in the low-density gas.

6.4.3 Alfvénic and Sonic Mach Numbers

Figure 6.5 shows the characteristic velocities of the system as a function of the density, at four evolutionary times of the cloud. At all times, the turbulent rms velocity exceeds the sound speed of the system. The flow ranges from mildly supersonic, $\mathcal{M} \approx 1$, at low densities $n = 10^{-2}\text{--}1\text{ cm}^{-3}$, to hypersonic, $\mathcal{M} \approx 10$, for densities $n > 1\text{ cm}^{-3}$. This is the general behavior of the turbulent ISM with supersonic shocks permeating the gas at all scales and densities (Mac Low & Klessen, 2004; Padoan & Nordlund, 2011; Klessen & Glover, 2014; Vázquez-Semadeni, 2015).

On the other hand, the turbulent rms velocity shows a transition from trans-Alfvénic, $\mathcal{M}_A \approx 1$, for densities below 10^2 cm^{-3} , to super-Alfvénic, $\mathcal{M}_A > 1$, at higher densities. This behavior suggests that for densities up to 100 cm^{-2} , the magnetic field is capable of reacting to perturbations as fast as it is being bent. The magnetic field pushes back on the gas, restricting its flow across field lines. In the case of strong shocks moving perpendicular to magnetic field lines, we expect the magnetic field to be compressed with the gas. If we write the Lagrangian form of the induction equation, assuming flux freezing,

$$\frac{\partial \vec{B}}{\partial t} = -\vec{B} \nabla \cdot \vec{v}_\perp + (\vec{B} \cdot \nabla) \vec{v}_\perp, \quad (6.6)$$

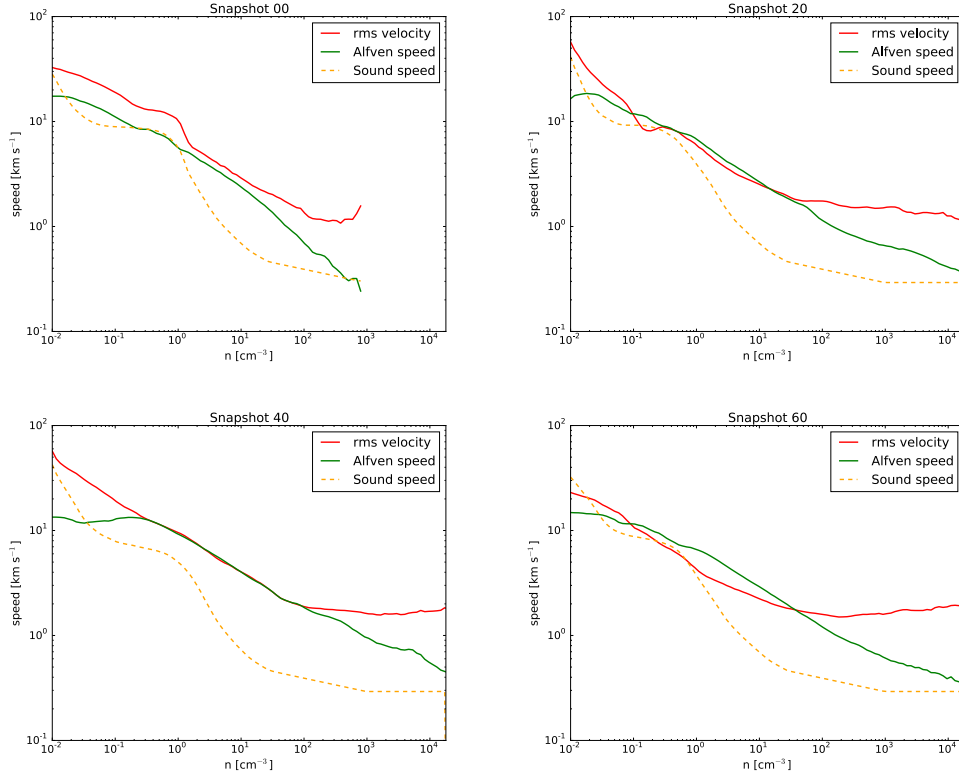


Figure 6.5: Mean characteristic velocities of the ISM within a $(100 \text{ pc})^3$ box, centered in the cloud’s center of mass, as a function of gas density. The panels correspond to evolutionary times of 0, 2, 4, and 6 Myr since the moment self-gravity was included.

where \vec{v}_\perp is the perpendicular velocity with respect to the orientation of the magnetic field. The first term on the right hand side dominates in a strong shock. Thus, we expect that the field will compress with the gas density, up to the point where the field is strong enough for the Alfvén speed to exceed the shock speed, reducing the shock to a magnetosonic wave.

For densities above 100 cm^{-3} , gravity dominates the total energy of the gas (see Fig. 6.4). As discussed before, the gas at these densities is undergoing gravitational contraction. As the collapse transforms gravitational potential energy into kinetic energy, the rms velocity grows. Although the magnetic energy also grows, as field lines are compressed together, it does not grow as fast as the kinetic energy, resulting in super-Alfvénic flows inside the cloud, as suggested by Padoan & Nordlund (1999).

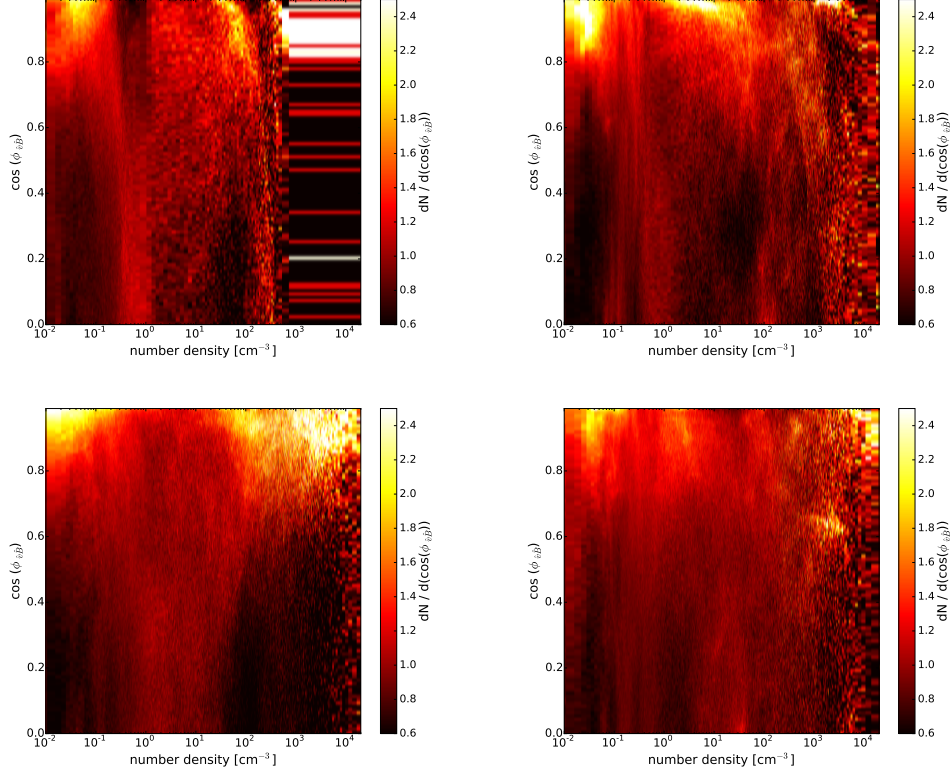


Figure 6.6: Probability density distribution of the relative orientations between the local velocity, \hat{v} , and the magnetic field, \hat{B} , as a function of gas density, within a $(100 \text{ pc})^3$ box centered on the cloud center of mass. The panels correspond to evolutionary times of 0, 2, 4, and 6 Myr since the moment self-gravity was included.

6.4.4 Velocity-Magnetic Field Relative Orientation

In order to explain the flat behavior of the magnetic field-density relation for densities below $n < 100 \text{ cm}^{-3}$, it has been suggested that gas flows preferentially along field lines. Figure 6.6 shows the distribution of the cosine of the angle between the direction of the velocity, \hat{v} , and the magnetic field, \hat{B} , as a function of density, at four different evolutionary stages.

At all stages of evolution the magnetic field indeed tends toward being oriented parallel to the flow velocity, $\cos(\phi_{\hat{v}\hat{B}}) = 0$, for densities below 100 cm^{-3} . Note, however, that configurations with the field perpendicular to the flow still constitute a substantial fraction of the volume, as the lowest probability densities exceed 0.6, a quarter of the maximum value. The probability distribution of relative orientations is almost flat for number densities

$0.5 < n < 50$. This density range corresponds to transition gas in a thermally unstable phase of the ISM. Gas remains in this density range for only a short time, as it consists mostly of shocked gas, rapidly cooling towards the cold, dense phase of the ISM.

Large fluctuations in the relative distribution of the orientations are observed at $t = 4$ Myr. This is likely caused by the explosion of a SN within the analyzed volume at $t = 2.62$ Myr. The SN remnant expands into an inhomogeneous density distribution, producing turbulent motions both parallel and perpendicular to the magnetic field, resulting in the predominantly flat behavior of the probability seen.

The alignment between the velocity and the magnetic field might not only be caused by strong magnetic fields. As discussed by Padoan & Nordlund (1999) there are two opposite processes that can cause alignment. 1) *Dynamical alignment*, occurring when the field is strong enough to restrict the gas flows along field lines, and 2) *Kinematic alignment*, occurring when the field is swept up by the gas flows, forcing alignment.

It is likely that for densities $n < 100 \text{ cm}^{-3}$, the velocity and magnetic field are *dynamically aligned*, as the flows are trans-Alfvénic (see Sect. 6.4.3), at least when the system has not been recently perturbed by a nearby SN explosion. In this regime, the magnetic tension can restrict gas flows perpendicular to the magnetic field.

For densities $n > 100 \text{ cm}^{-3}$, the angle $\phi_{\hat{v}\hat{B}}$ shows large fluctuations as a function of time and density. This regime is less likely to be affected by random turbulence in the environment, but on the other hand is most likely to be affected by gravitational contraction, as gravity is the dominant form of energy here (see Sect. 6.4.2). As the cloud contracts, it can compress the magnetic field. At $t = 2$ Myr, $\phi_{\hat{v}\hat{B}}$ transitions at these densities from a preferentially aligned flow into a random distribution of the alignment. At $t = 4$ Myr, $\phi_{\hat{v}\hat{B}}$ shows some alignment between the velocity and the magnetic field, which is most certainly caused by *kinematic alignment* of the collapsing gas, as the flow here is super-Alfvénic. Later, at $t = 6$ Myr, the relative distribution of the angles is very random, with most of the flows aligned with the fields, but with large fractions of the gas having oblique relative orientations. This erratic behavior of the relative angles shows that when gravity takes hold of the dynamics of the gas, the magnetic field is carried along with the contraction.

6.4.5 Histogram of Relative Orientation

We now analyze the relative orientation of the magnetic field with respect to the density gradients in and around the cloud.

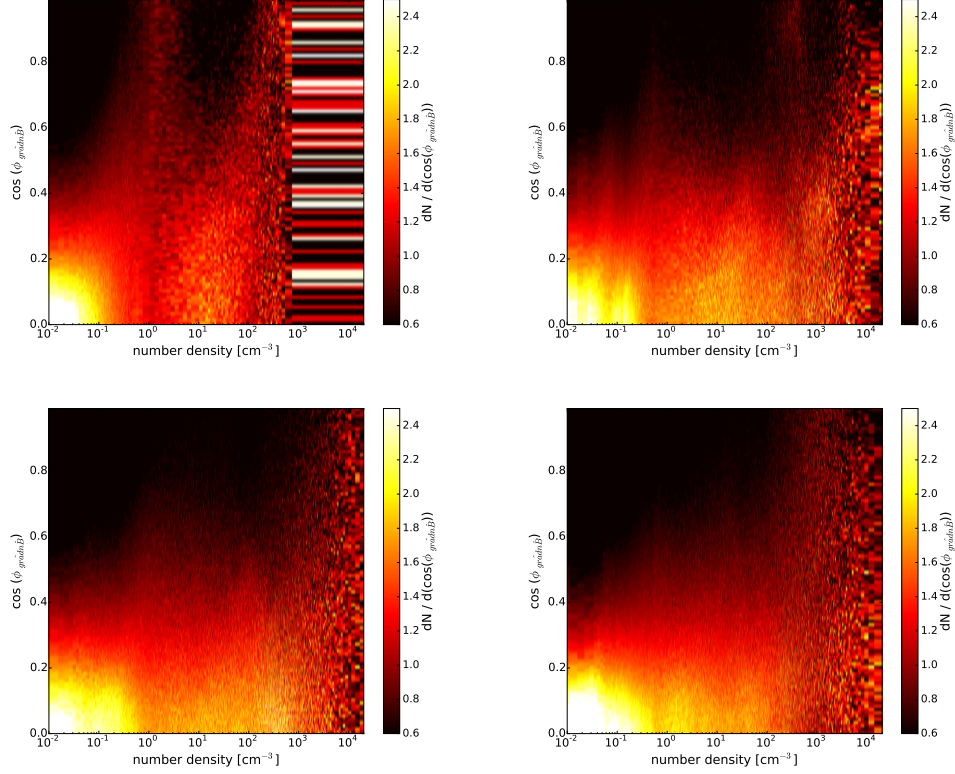


Figure 6.7: Probability density distribution of the relative orientations between the local density gradient, ∇n , and the magnetic field, \hat{B} , as a function of gas density, within a $(100 \text{ pc})^3$ box centered on the cloud center of mass. The panels correspond to evolutionary times of 0, 2, 4, and 6 Myr since the time self-gravity was included.

Figure 6.7 shows the histogram of relative orientation as a function of gas density for different evolutionary times of the simulation. For $n < 100 \text{ cm}^{-3}$, the magnetic field is predominantly perpendicular to the local direction of the density gradient, $\cos(\phi_{\hat{n}\hat{B}}) \approx 0$, although again with substantial variation, as the lowest probability densities are still 0.6. In this regime, the gas is trans-Alfvénic and also preferentially flowing along field lines.

This raises the question of how a magnetic field perpendicularly aligned to the density gradient can produce little to no correlation between the field strength and the density in the $\vec{B} - n$ relation. As we will discuss in more detail in the following section (§6.4.6), there is almost an equal fraction of gas flowing parallel and perpendicular to the density gradient, so that gas flows can still cause compression along the field lines, but tend to maintain

the relative orientations of the velocity, magnetic field and density gradient.

For densities $n > 100 \text{ cm}^{-3}$ the gas is gravitationally dominated and the flows are super-Alfvénic. As the cloud contracts, the relative orientation shows a transition from predominantly perpendicular to random, consistent with isotropic collapse and in agreement with the calculations performed by [Soler et al. \(2013\)](#).

6.4.6 Density Gradient-Velocity Relative Orientation

As discussed in the previous section, it is not intuitive how a gas flow aligned with the magnetic field can produce density fluctuations that remain perpendicular to the density gradient, in order to retain the lack of correlation between field and density seen.

Although the magnetic field is indeed preferentially aligned to the density gradient, the dispersion of the alignments is also significant. Similarly, the dispersion of the relative orientation between the velocity and the magnetic fields is also large. It is at the intersection of these two probability distributions that there is a compression of mass towards higher densities, while maintaining the preferential alignments discussed in the previous two sections.

Figure 6.8 shows the relative orientation between the velocities with respect to the density gradient. There is almost no preferential orientation between these two vectors as a function of time and density, as expected for chaotic, turbulent motions.

6.5 Conclusions

Magnetic fields have been argued to play an important role in the formation, evolution, and collapse of molecular clouds and to maintain the envelopes of the clouds supported against gravitational collapse ([Elmegreen, 2007](#)). Observations suggest that magnetic fields constrain the dynamics of the flow for densities below 300 cm^{-3} , but are isotropically advected in gravitationally contracting clouds for densities above 300 cm^{-3} , giving rise to the two regimes of the B-n relation ([Crutcher et al., 2010a](#); [Crutcher, 2012](#)).

We present in this chapter, three-dimensional MHD simulations dense, molecular clouds formed in a turbulent environment, collapsing under the action of their own self-gravity. We investigate the dynamical influence of magnetic fields and their connection over four orders of magnitude in spatial scales, and seven orders of magnitude in density scales. We find that:

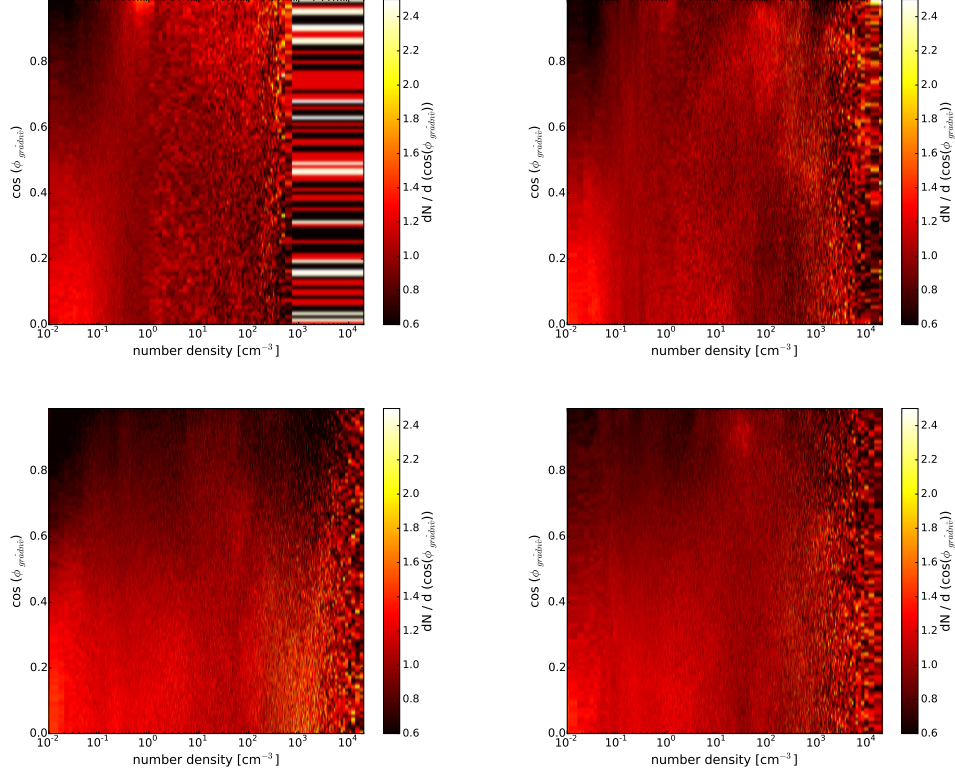


Figure 6.8: Probability density distribution of the relative orientations between the local gradient of the density, \hat{n} , and the local direction of the velocity, \hat{v} , within a $(100 \text{ pc})^3$ box centered on the cloud center of mass. The panels correspond to evolutionary times of 0, 2, 4, and 6 Myr since the time self-gravity was included. The orientations are almost random.

- Random turbulent motions in the diffuse ISM and gravitational contraction of dense structures maintain the magnetic field strength at magnitudes consistent with those reported in observations (Crutcher, 2012). The behavior of the magnetic field strength in relation to density also appears generally consistent, with no correlation between the field strength and gas density for densities $n < 100 \text{ cm}^{-3}$, and a positive correlation above that density. However, the average $\vec{B} - n$ relation in our model has a significantly shallower slope than the observed relation between the maximum line-of-sight field strength and the derived density.
- Dense clouds with $n > 100 \text{ cm}^{-3}$ have super-Alfvénic rms velocity dispersions, caused by fast turbulent motions driven by hierarchical

gravitational contraction, suggesting that the fields are not dynamically important in this regime.

- In contrast, diffuse gas with $n < 100 \text{ cm}^{-3}$ in the envelopes of MCs and the diffuse ISM has trans-Alfvénic (Boulares & Cox, 1990) velocity dispersion, suggesting that it is magnetically supported against gravitational collapse (Elmegreen, 2007), and its flow is generally constrained to follow field lines (Padoan & Nordlund, 1999), although substantial deviations are still seen in the simulations.
- While gas flows are *dynamically aligned* along the magnetic field at low densities, oblique supersonic shocks produce strong density fluctuations, while still maintaining the moderate bias found towards perpendicular relative orientation between magnetic fields and density gradients.

Chapter 7

Summary and Outlook

7.1 Summary

Molecular clouds are the main sites of star formation in the Galaxy, and constitute the intermediate scales between cosmological galaxy evolution models and star and planet formation environments. Understanding how molecular clouds form, evolve and collapse in a realistic, turbulent environment is key for understanding how large-scale structure growth manifests in the properties of observable galaxies, and what the initial conditions are for the formation of planetary systems. However, it remains unclear how long molecular clouds live in the ISM, how fast they grow in mass, what physical processes dominate their dynamics, and why they seem to be so inefficient at forming stars.

In this thesis I have presented a detailed analysis of the properties of molecular clouds formed in a realistic, turbulent, galactic environment. I divided the analysis in three parts where I compared the relative importance of three major processes previously postulated as capable of influencing the lifetimes of self-gravitating molecular clouds in galaxies. At each point in this analysis, I compared basic properties of the simulations with observations in order to check the consistency of the approximations.

I first studied the interaction between SN explosions and dense molecular clouds. Concentrating on the velocity dispersion-size relation $\sigma_{tot} \propto R^{1/2}$ observed in MCs in the Galaxy (Larson, 1981; Solomon et al., 1987; Falgarone et al., 2009; Heyer et al., 2009), I measured the properties of a cloud population formed in a turbulent, stratified ISM with and without the effects of gas self-gravity while continuously driving turbulence with SN explosions, (Chapter 4). I find that SN feedback in the diffuse ISM appear unable to drive turbulent motions with velocities exceeding one kilometer per second

within clouds, but instead predict values that are up to a factor of five lower than the observed velocities; in contrast, gravitational contraction appears able to reproduce the observed values. This suggests that contraction is likely to be the origin of the velocity dispersion-size relation, driving non-thermal motions (Traficante et al., 2015) correlated with the cloud size as observed.

I continued to analyze the mass accretion rates and histories of MCs in the turbulent environment, focusing my attention on the efficiency with which accretion can drive turbulence (Chapter 5). I find that mass accretion rates onto molecular clouds of moderate mass do depend on a combination of the gravitational pull from the cloud and the intermittency of the turbulence in the environment. Nearby SN explosions have a strong impact on the mass accretion histories of MCs, as they can simultaneously promote and prevent accretion by compressing and disrupting different parts of the cloud's envelope. Although MCs accrete kinetic energy at a sufficient rate to compensate for the decay of supersonic turbulence within them, accretion flows are weak compared to the total rate of change of the cloud's kinetic energy. The energy source for these non-thermal motions must instead come from the gravitational contraction of the cloud converting gravitational potential energy to kinetic energy.

Finally I investigated the strength and morphology of magnetic fields in and around the cloud, and their effects on the cloud collapse and its environment (Chapter 6). I find that only after gas self-gravity has been included and the cloud has began contracting, I can recover magnetic field strengths and their dependence with gas density, comparable to those observed inside MCs in the Galaxy. However, these magnetic fields are unable to prevent the clouds from collapsing, a result that is consistent with observational estimates by Crutcher (1999, 2012) and Crutcher et al. (2010b). Nonetheless, their envelopes do appear to be magnetically dominated, consistent with the proposals of Padoan & Nordlund (1999) and Elmegreen (2007).

Together, these results strongly suggest that molecular clouds are highly dynamical objects, quickly evolving, beginning to hierarchically collapse shortly after their formation, even as they continue to grow in mass. However, the picture I present here remains biased towards runaway collapsing clouds because the models presented here do not include self-consistent star formation and correlated stellar feedback within the clouds. Newborn massive stars strongly influence their parent clouds through ionizing radiation, winds and SN feedback. Their combined action should be able to prevent further star formation and maintain star formation efficiencies close to those observed, something that I will examine in the future as I describe in the next section.

7.2 Outlook

The models presented here represent a novel study of molecular cloud formation and evolution including the dominant physical processes in the interstellar medium, capturing its dynamics over tens of megayears of evolution, and over four and a half orders of magnitude in spatial resolution. I provide a series of high-resolution models of molecular clouds in their galactic context, representing an excellent set of models that can be used for comparison with observations of molecular clouds, or initial conditions for re-simulations attempting to resolve the formation of individual stars and stellar clusters.

Recent multi-scale observations of molecular clouds follow the connection between the large scale filamentary structures of a cloud down to sub-pc resolution, at the fragmentation scales of the protostars, inside the “coherent core” region (Pineda et al., 2015). The clouds simulated in this thesis provide a useful set of models to be compared with these observations, offering similar dynamic ranges, and tracing the morphology and the dynamics of non-isothermal gas, embedded in a realistic turbulent environment, to follow the formation and fragmentation of these filaments. Observations of self-absorption of optically thick molecular tracers towards massive filaments show the presence of accretion flows (Peretto et al., 2013). The models of accreting molecular clouds presented in chapter §5 may allow to constrain models of the temperatures and densities around these molecular filaments, to better understand these accretion flows.

On the simulations side, including self-consistent star formation and stellar feedback is a crucial development necessary in these models to close the cycle of gas and stars. Fortunately, there has already been a lot of progress in this area. A sink particle module that replaces indefinitely collapsing gas with a gravitationally interacting particle to allow continued computation has been developed by Federrath et al. (2010). A radiative feedback module including both ionizing and non-ionizing radiation, using the sink particles as stellar sources, has been developed by Baczynski et al. (2015), while a stellar wind module, also taking the sink particles as the sources, has been developed and included in FLASH by Gatto (private communication). It is now a matter of time until we can link all these processes together in self-consistent simulations of molecular cloud formation and evolution in a galactic environment. These updates will represent a significant improvement to the currently existing models, as they will allow the history of star formation to be captured as molecular clouds form and evolve. This will in turn allow us to explore the interaction of stellar feedback with the parent clouds and their turbulent environments, and address the important question of star-formation self-regulation and its linkages with the evolution of

molecular clouds.

So far, in this thesis, I have presented a picture of rapidly evolving molecular clouds, quickly collapsing and forming stars shortly after their formation. However, the question of how the rate of star-formation per free fall time in these clouds still remains an open question. Given our results, it appears most likely that stellar feedback is responsible for preventing the conversion of all the cloud mass into stars by halting the cloud's contraction, and dissipating the bulk of the cloud mass back into the diffuse ISM. However, if stellar feedback is as efficient as I expect at destroying the parent clouds, all of the observed clouds in the Galaxy should be destroyed within a couple of global free fall times. As I do not expect the present day molecular mass fraction to be very different than the fraction at any other time, I finally must ask the question of what process could form new molecular clouds fast enough to match the destruction rate expected from the quickly evolving cloud model presented here. [Toomre \(1964\)](#) gravitational instability and sweeping of gas by supernovae both appear worthy of study to answer this question.

Bibliography

- Ade, P. A. R., Aghanim, N., Alves, M. I. R., et al. 2016, *Astronomy & Astrophysics*, 586, A138
- Andersson, B.-G., Lazarian, A., & Vaillancourt, J. E. 2015, *Annual Review of Astronomy and Astrophysics*, 53, 501
- Baczynski, C., Glover, S. C. O., & Klessen, R. S. 2015, 32
- Bakes, E. L. O., & Tielens, A. G. G. M. 1994, *The Astrophysical Journal*, 427, 822
- Ballesteros-Paredes, J. 2006, *Monthly Notices of the Royal Astronomical Society*, 372, 443
- Ballesteros-Paredes, J., Hartmann, L., & Vázquez-Semadeni, E. 1999a, *The Astrophysical Journal*, 527, 285
- Ballesteros-Paredes, J., Hartmann, L. W., Vázquez-Semadeni, E., Heitsch, F., & Zamora-Avilés, M. A. 2011, *Monthly Notices of the Royal Astronomical Society*, 411, 65
- Ballesteros-Paredes, J., & Mac Low, M. M. 2002, *The Astrophysical Journal*, 570, 734
- Ballesteros-Paredes, J., Vázquez-Semadeni, E., & Scalo, J. 1999b, *The Astrophysical Journal*, 515, 286
- Balsara, D. S., Kim, J., Mac Low, M. M., & Mathews, G. J. 2004, *The Astrophysical Journal*, 617, 339
- Banerjee, R., Vázquez-Semadeni, E., Hennebelle, P., & Klessen, R. S. 2009, *Monthly Notices of the Royal Astronomical Society*, 398, 1082
- Beaumont, C. N., S. R. Offner, S., Shetty, R., Glover, S. C. O., & Goodman, A. A. 2013, *The Astrophysical Journal*, 777, 173

- Bergin, E. A., Goldsmith, P. F., Snell, R. L., & Langer, W. D. 1997, *The Astrophysical Journal*, 482, 285
- Bergin, E. A., & Langer, W. D. 1997, *The Astrophysical Journal*, 486, 316
- Bertoldi, F., & McKee, C. F. 1992, *The Astrophysical Journal*, 395, 140
- Bihl, S., Beuther, H., Linz, H., et al. 2015, *Astronomy & Astrophysics*, 579, A51
- Boulares, A., & Cox, D. P. 1990, *The Astrophysical Journal*, 365, 544
- Bregman, J. N. 1980, *The Astrophysical Journal*, 236, 577
- Brunt, C. M. 2003, *The Astrophysical Journal*, 583, 280
- Brunt, C. M., Heyer, M. H., & Mac Low, M. M. 2009, *Astronomy and Astrophysics*, 504, 883
- Burkhart, B., Collins, D. C., & Lazarian, A. 2015, *The Astrophysical Journal*, 808, 48
- Burstein, P., Borken, R. J., Kraushaar, W. L., & Sanders, W. T. 1977, *The Astrophysical Journal*, 213, 405
- Carrasco-González, C., Torrelles, J. M., Cantó, J., et al. 2015, *Science (New York, N.Y.)*, 348, 114
- Caselli, P., & Myers, P. C. 1995, *The Astrophysical Journal*, 446, 665
- Chandrasekhar, S. 1951, *Proceedings of the Royal Society A: Mathematical, Physical and Engineering Sciences*, 210, 26
- Chandrasekhar, S., & Fermi, E. 1953a, *The Astrophysical Journal*, 118, 113
- . 1953b, *The Astrophysical Journal*, 118, 116
- Cheung, A. C., Rank, D. M., Townes, C. H., Thornton, D. D., & Welch, W. J. 1968, *Physical Review Letters*, 21, 1701
- Churchwell, E. 2002, *Annual Review of Astronomy and Astrophysics*, 40, 27
- Clark, P. C., & Glover, S. C. O. 2014, *Monthly Notices of the Royal Astronomical Society*, 444, 2396
- Clark, P. C., Glover, S. C. O., Klessen, R. S., & Bonnell, I. a. 2012, *Monthly Notices of the Royal Astronomical Society*, 424, 2599

- Clarke, S. D., & Whitworth, A. P. 2015, *Monthly Notices of the Royal Astronomical Society*, 449, 1819
- Clausius, R. J. E. 1870, *Philosophical Magazine*, 40, 122
- Clemens, D. P., Sanders, D. B., & Scoville, N. Z. 1988, *The Astrophysical Journal*, 327, 139
- Clemens, D. P., Sanders, D. B., Scoville, N. Z., & Solomon, P. M. 1986, *The Astrophysical Journal Supplement Series*, 60, 297
- Colombo, D., Meidt, S. E., Schinnerer, E., et al. 2014, *The Astrophysical Journal*, 784, 4
- Cox, D. P., & Smith, B. W. 1974, *The Astrophysical Journal*, 189, L105
- Crutcher, R. M. 1999, *The Astrophysical Journal*, 520, 706
- . 2012, *Annual Review of Astronomy and Astrophysics*, 50, 29
- Crutcher, R. M., Evans, N. J., I., Troland, T., & Heiles, C. 1975, *The Astrophysical Journal*, 198, 91
- Crutcher, R. M., Hakobian, N., & Troland, T. H. 2010a, *Monthly Notices of the Royal Astronomical Society: Letters*, 402, L64
- Crutcher, R. M., Troland, T. H., Goodman, A. A., et al. 1993, *The Astrophysical Journal*, 407, 175
- Crutcher, R. M., Wandelt, B., Heiles, C., Falgarone, E., & Troland, T. H. 2010b, *The Astrophysical Journal*, 725, 466
- Dale, J. E., Bonnell, I. A., Clarke, C. J., & Bate, M. R. 2005, *Monthly Notices of the Royal Astronomical Society*, 358, 291
- Dale, J. E., Ercolano, B., & Bonnell, I. A. 2012, *Monthly Notices of the Royal Astronomical Society*, 424, 377
- . 2013a, *Monthly Notices of the Royal Astronomical Society*, 427, 2852
- . 2013b, *Monthly Notices of the Royal Astronomical Society*, 430, 234
- Dale, J. E., Ngoumou, J., Ercolano, B., & Bonnell, I. A. 2014, *Monthly Notices of the Royal Astronomical Society*, 442, 694
- Dalgarno, A., & McCray, R. A. 1972, *Annual Review of Astronomy and Astrophysics*, 10, 375

- Dalgarno, A., Yan, M., & Liu, W. 1999, *The Astrophysical Journal Supplement Series*, 125, 237
- Dame, T. M., Hartmann, D., & Thaddeus, P. 2001, *The Astrophysical Journal*, 547, 792
- Dame, T. M., Ungerechts, H., Cohen, R. S., et al. 1987, *The Astrophysical Journal*, 322, 706
- de Avillez, M. A., & Mac Low, M. M. 2002, *The Astrophysical Journal*, 581, 1047
- De Pree, C. G., Peters, T., Mac Low, M. M., et al. 2014, *The Astrophysical Journal*, 781, L36
- Dehnen, W., & Binney, J. 1998, *Monthly Notices of the Royal Astronomical Society*, 294, 429
- Dib, S., Kim, J., Vázquez-Semadeni, E., Burkert, A., & Shadmehri, M. 2007, *The Astrophysical Journal*, 661, 262
- Dobbs, C. L., Krumholz, M. R., Ballesteros-Paredes, J., et al. 2014, in *Protostars and Planets VI*, ed. H. Beuther, R. S. Klessen, C. P. Dullemond, & T. Henning (Tucson: University of Arizona Press), 3–26
- Draine, B. T. 1978, *The Astrophysical Journal Supplement Series*, 36, 595
- Draine, . 2011, *Physics of the Interstellar and Intergalactic Medium* by Bruce T. Draine. Princeton University Press
- Einstein, A. 1912, *Annalen der Physik*, 343, 881
- Elmegreen, B. G. 1993, *The Astrophysical Journal*, 419, L29
- . 2007, *The Astrophysical Journal*, 668, 1064
- Evans II, N. J. 1999, *Annual Review of Astronomy and Astrophysics*, 37, 311
- Falgarone, E., Hily-Blant, P., & Levrier, F. 2004, *Astrophysics and Space Science*, 292, 89
- Falgarone, E., Pety, J., & Hily-Blant, P. 2009, *Astronomy and Astrophysics*, 507, 355
- Falgarone, E., Troland, T. H., Crutcher, R. M., & Paubert, G. 2008, *Astronomy and Astrophysics*, 487, 247

- Federrath, C. 2013, *Monthly Notices of the Royal Astronomical Society*, 436, 1245
- Federrath, C., Banerjee, R., Clark, P. C., & Klessen, R. S. 2010, *The Astrophysical Journal*, 713, 269
- Federrath, C., & Klessen, R. S. 2012, *The Astrophysical Journal*, 761, 156
- Ferriere, K. M. 2001, *Reviews of Modern Physics*, 73, 1031
- Field, G. B., Goldsmith, D. W., & Habing, H. J. 1969, *The Astrophysical Journal*, 155, L149
- Froebrich, D., Makin, S. V., Davis, C. J., et al. 2015, *Monthly Notices of the Royal Astronomical Society*, 454, 2586
- Fryxell, B., Olson, K., Ricker, P., et al. 2000, *The Astrophysical Journal Supplement Series*, 131, 273
- Fukui, Y., & Kawamura, A. 2010, *Annual Review of Astronomy and Astrophysics*, 48, 547
- Fukui, Y., Mizuno, N., Yamaguchi, R., et al. 1999, *Publications of the Astronomical Society of Japan*, 51, 745
- Fukui, Y., Kawamura, A., Wong, T., et al. 2009, *The Astrophysical Journal*, 705, 144
- Gatto, A., Walch, S., Mac Low, M. M., et al. 2015, *Monthly Notices of the Royal Astronomical Society*, 449, 1057
- Gibson, D., Plume, R., Bergin, E., Ragan, S., & Evans, N. 2009, *The Astrophysical Journal*, 705, 123
- Girichidis, P., Naab, T., Walch, S., et al. 2016a, *The Astrophysical Journal*, 816, L19
- Girichidis, P., Walch, S., Naab, T., et al. 2016b, *Monthly Notices of the Royal Astronomical Society*, 456, 3432
- Glassgold, A. E., Galli, D., & Padovani, M. 2012, *The Astrophysical Journal*, 756, 157
- Gnat, O., & Ferland, G. J. 2012, *The Astrophysical Journal Supplement Series*, 199, 20

- Gnedin, N. Y., Glover, S. C. O., Klessen, R. S., & Springel, V. 2015, *Star Formation in Galaxy Evolution: Connecting Numerical Models to Reality*, 1st edn., ed. Y. Revaz, P. Jablonka, R. Teyssier, & L. Mayer (Springer-Verlag Berlin Heidelberg), 85–249
- Goldbaum, N. J., Krumholz, M. R., Matzner, C. D., & McKee, C. F. 2011, *The Astrophysical Journal*, 738, 101
- Goldreich, P., & Kwan, J. 1974, *The Astrophysical Journal*, 189, 441
- Habing, H. J. 1968, *Bulletin of the Astronomical Institutes of the Netherlands*, 19
- Hartmann, L., Ballesteros-Paredes, J., & Bergin, E. A. 2001, *The Astrophysical Journal*, 562, 852
- Hartquist, T. W., Black, J. H., & Dalgarno, A. 1978a, *Monthly Notices of the Royal Astronomical Society*, 185, 643
- Hartquist, T. W., Doyle, H. T., & Dalgarno, A. 1978b, *Astronomy and Astrophysics*, 68, 65
- Heiles, C. 1987, *The Astrophysical Journal*, 315, 555
- Heiles, C., & Troland, T. H. 2004, *The Astrophysical Journal Supplement Series*, 151, 271
- . 2005, *The Astrophysical Journal*, 624, 773
- Heiles, C., & Crutcher, S. 2005, *Lecture Notes in Physics*, Vol. 664, *Cosmic Magnetic Fields*, ed. R. Wiełebinski & R. Beck (Berlin/Heidelberg: Springer-Verlag), doi:10.1007/b104621
- Heitsch, F., Burkert, A., Hartmann, L. W., Slyz, A. D., & Devriendt, J. E. G. 2005, *The Astrophysical Journal*, 633, L113
- Heitsch, F., Mac Low, M. M., & Klessen, R. S. 2001a, *The Astrophysical Journal*, 547, 280
- Heitsch, F., Slyz, A. D., Devriendt, J. E. G., Hartmann, L. W., & Burkert, A. 2006, *The Astrophysical Journal*, 648, 1052
- Heitsch, F., Zweibel, E. G., Mac Low, M., Li, P., & Norman, M. L. 2001b, *The Astrophysical Journal*, 561, 800
- Hennebelle, P., & Iffrig, O. 2014, *Astronomy & Astrophysics*, 570, A81

- Hewitt, J. W., Yusef-Zadeh, F., & Wardle, M. 2009, *The Astrophysical Journal*, 706, L270
- Heyer, M., Krawczyk, C., Duval, J., & Jackson, J. M. 2009, *The Astrophysical Journal*, 699, 1092
- Heyer, M. H., Carpenter, J. M., & Snell, R. L. 2001, *The Astrophysical Journal*, 551, 852
- Hill, A. S., Joungh, M. K. R., Mac Low, M. M., et al. 2012, *The Astrophysical Journal*, 750, 104
- Hopkins, P. F. 2014, *Astrophysics Source Code Library*
- Houde, M., Vaillancourt, J. E., Hildebrand, R. H., Chitsazzadeh, S., & Kirby, L. 2009, *The Astrophysical Journal*, 706, 1504
- Hughes, A., Meidt, S. E., Colombo, D., et al. 2013, *The Astrophysical Journal*, 779, 46
- Ibáñez-Mejía, J. C., Mac Low, M. M., Klessen, R. S., & Baczynski, C. 2016, *ApJ*, in Press
- Jackson, J. M., Rathborne, J. M., Shah, R. Y., et al. 2006, *The Astrophysical Journal Supplement Series*, 163, 145
- Jeans, J. H. 1902, *Philosophical Transactions of the Royal Society A: Mathematical, Physical and Engineering Sciences*, 199, 1
- Jenkins, E. B., & Meloy, D. A. 1974, *The Astrophysical Journal*, 193, L121
- Joungh, M. K. R., & Mac Low, M. M. 2006, *The Astrophysical Journal*, 653, 1266
- Joungh, M. K. R., Mac Low, M. M., & Bryan, G. L. 2009, *The Astrophysical Journal*, 704, 137
- Kauffmann, J., Pillai, T., & Goldsmith, P. F. 2013, *The Astrophysical Journal*, 779, 185
- Kawamura, A., Minamidani, T., Mizuno, Y., et al. 2009a, *Globular Clusters - Guides to Galaxies*, ed. T. Richtler & S. Larsen, *Eso Astrophysics Symposia* (Berlin, Heidelberg: Springer Berlin Heidelberg), doi:10.1007/978-3-540-76961-3

- Kawamura, A., Mizuno, Y., Minamidani, T., et al. 2009b, *The Astrophysical Journal Supplement Series*, 184, 1
- Kim, C.-G., Ostriker, E. C., & Kim, W.-T. 2013, *The Astrophysical Journal*, 776, 1
- Klessen, R. S. 2011, *EAS Publications Series*, 51, 133
- Klessen, R. S., & Glover, S. C. O. 2014, eprint arXiv:1412.5182
- Klessen, R. S., Heitsch, F., & Mac Low, M. M. 2000, *The Astrophysical Journal*, 535, 887
- Klessen, R. S., & Hennebelle, P. 2010, *Astronomy and Astrophysics*, 520, A17
- Klessen, R. S., Krumholz, M. R., & Heitsch, F. 2011, *Advanced Science Letters*, 4, 258
- Kolmogorov, A. 1941, *Doklady Akademii Nauk SSSR*
- Konstandin, L., Shetty, R., Girichidis, P., & Klessen, R. S. 2014, *Monthly Notices of the Royal Astronomical Society*, 446, 1775
- Kritsuk, A. G., Lee, C. T., & Norman, M. L. 2013, *Monthly Notices of the Royal Astronomical Society*, 436, 3247
- Kritsuk, A. G., Norman, M. L., & Padoan, P. 2006, *The Astrophysical Journal*, 638, L25
- Kritsuk, A. G., Norman, M. L., & Wagner, R. 2011, *The Astrophysical Journal*, 727, L20
- Krumholz, M. R., & McKee, C. F. 2005, *The Astrophysical Journal*, 630, 250
- Kuijken, K., & Gilmore, G. 1989, *Monthly Notices of the Royal Astronomical Society*, 239, 605
- Langer, W. D., & Penzias, A. A. 1990, *The Astrophysical Journal*, 357, 477
- Larson, R. 1981, *Monthly Notices of the Royal Astronomical Society*
- Lazarian, A. 2007, *Journal of Quantitative Spectroscopy and Radiative Transfer*, 106, 225

- Lee, E. J., Chang, P., & Murray, N. 2015, *The Astrophysical Journal*, 800, 49
- Li, M., Ostriker, J. P., Cen, R., Bryan, G. L., & Naab, T. 2015, *The Astrophysical Journal*, 814, 4
- Mac Low, M. M. 1999, *The Astrophysical Journal*, 524, 169
- Mac Low, M. M., & Klessen, R. S. 2004, *Reviews of Modern Physics*, 76, 125
- Mac Low, M. M., Klessen, R. S., Burkert, A., & Smith, M. D. 1998, *Physical Review Letters*, 80, 2754
- Mac Low, M. M., & Ossenkopf, V. 2000, *Astronomy and Astrophysics*, 353, 339
- Mathis, J. S., Rumpl, W., & Nordsieck, K. H. 1977, *The Astrophysical Journal*, 217, 425
- McKee, C. F., & Ostriker, J. P. 1977, *The Astrophysical Journal*, 218, 148
- McKee, C. F., & Williams, J. P. 1997, *The Astrophysical Journal*, 476, 144
- McKee, C. F., & Zweibel, E. G. 1992, *The Astrophysical Journal*, 399, 551
- Meidt, S. E., Hughes, A., Dobbs, C. L., et al. 2015, *The Astrophysical Journal*, 806, 72
- Meinecke, J., Doyle, H. W., Miniati, F., et al. 2014, *Nat Phys*, 10, 520
- Mestel, L., & Spitzer, L. 1956, *Monthly Notices of the Royal Astronomical Society*, 116, 503
- Miller, G. E., & Scalo, J. M. 1979, *The Astrophysical Journal Supplement Series*, 41, 513
- Mizuno, N., Yamaguchi, R., Mizuno, A., et al. 2001, *Publications of the Astronomical Society of Japan*, 53, 971
- Mouschovias, T. C. 1977, *The Astrophysical Journal*, 211, 147
- . 1991, *The Astrophysical Journal*, 373, 169
- Mouschovias, T. C., & Spitzer, L., J. 1976, *The Astrophysical Journal*, 210, 326
- Myers, P. C., & Goodman, A. A. 1988, *The Astrophysical Journal*, 326, L27

- Naranjo-Romero, R., Vázquez-Semadeni, E., & Loughnane, R. M. 2015, *The Astrophysical Journal*, 814, 48
- Narayanan, G., Heyer, M. H., Brunt, C., et al. 2008, *The Astrophysical Journal Supplement Series*, 177, 341
- Navarro, J. F., Frenk, C. S., & White, S. D. M. 1996, *The Astrophysical Journal*, 462, 563
- Olling, R. P., & Merrifield, M. R. 2001, *Monthly Notices of the Royal Astronomical Society*, 326, 164
- Ossenkopf, V., & Mac Low, M. M. 2002, *Astronomy and Astrophysics*, 390, 307
- Ostriker, E. C., McKee, C. F., & Leroy, A. K. 2010, *The Astrophysical Journal*, 721, 975
- Ostriker, J. P., & McKee, C. F. 1988, *Reviews of Modern Physics*, 60, 1
- Padoan, P., Goodman, A., Draine, B. T., et al. 2001, *The Astrophysical Journal*, 559, 1005
- Padoan, P., Haugbølle, T., & Nordlund, . 2012, *The Astrophysical Journal*, 759, L27
- Padoan, P., & Nordlund, A. 1999, *The Astrophysical Journal*, 526, 279
- Padoan, P., & Nordlund, . 2011, *The Astrophysical Journal*, 730, 40
- Padoan, P., Pan, L., Haugbølle, T., & Nordlund, . 2016, *The Astrophysical Journal*, 822, 11
- Palmeirim, P., André, P., Kirk, J., et al. 2013, *Astronomy & Astrophysics*, 550, A38
- Pan, H.-A., Fujimoto, Y., Tasker, E. J., et al. 2015, *Monthly Notices of the Royal Astronomical Society*, 453, 3083
- Parker, . 1979, Oxford
- Peretto, N., Fuller, G. A., Duarte-Cabral, A., et al. 2013, *Astronomy & Astrophysics*, 555, A112
- Pineda, J. E., Offner, S. S. R., Parker, R. J., et al. 2015, *Nature*, 518, 213

- Plume, R., Jaffe, D. T., Evans, Neal J., I., Martín-Pintado, J., & Gómez-González, J. 1997, *The Astrophysical Journal*, 476, 730
- Reipurth, B., & Bally, J. 2001, *Annual Review of Astronomy and Astrophysics*, 39, 403
- Reissl, S., Wolf, S., & Seifried, D. 2014, *Astronomy & Astrophysics*, 566, A65
- Ricker, P. M. 2008, *The Astrophysical Journal Supplement Series*, 176, 293
- Rogers, H., & Pittard, J. M. 2013, *Monthly Notices of the Royal Astronomical Society*, 431, 1337
- Roman-Duval, J., Federrath, C., Brunt, C., et al. 2011, *The Astrophysical Journal*, 740, 120
- Roman-Duval, J., Jackson, J. M., Heyer, M., Rathborne, J., & Simon, R. 2010, *The Astrophysical Journal*, 723, 492
- Sanders, D. B., Clemens, D. P., Scoville, N. Z., & Solomon, P. M. 1986, *The Astrophysical Journal Supplement Series*, 60, 1
- Schinnerer, E., Meidt, S. E., Pety, J., et al. 2013, *The Astrophysical Journal*, 779, 42
- Shapiro, P. R., & Field, G. B. 1976, *The Astrophysical Journal*, 205, 762
- Shetty, R., Collins, D. C., Kauffmann, J., et al. 2010, *The Astrophysical Journal*, 712, 1049
- Shetty, R., Glover, S. C., Dullemond, C. P., et al. 2011, *Monthly Notices of the Royal Astronomical Society*, 415, 3253
- Shetty, R., & Ostriker, E. C. 2012, *The Astrophysical Journal*, 754, 2
- Shields, G. A. 1990, *Annual Review of Astronomy and Astrophysics*, 28, 525
- Shirley, Y. L. 2015, *Publications of the Astronomical Society of the Pacific*, 127, 299
- Shirley, Y. L., Evans II, N. J., Young, K. E., Knez, C., & Jaffe, D. T. 2003, *The Astrophysical Journal Supplement Series*, 149, 375
- Shu, F. H. 1977, *The Astrophysical Journal*, 214, 488
- Soler, J. D., Hennebelle, P., Martin, P. G., et al. 2013, *The Astrophysical Journal*, 774, 128

- Solomon, P. M., Rivolo, A. R., Barrett, J., & Yahil, A. 1987, *The Astrophysical Journal*, 319, 730
- Springel, V. 2010, *Monthly Notices of the Royal Astronomical Society*, 401, 791
- Stone, J. M., Ostriker, E. C., & Gammie, C. F. 1998, *The Astrophysical Journal*, 508, L99
- Sutherland, R. S., & Dopita, M. A. 1993, *The Astrophysical Journal Supplement Series*, 88, 253
- Tamburro, D., Rix, H.-W., Leroy, A. K., et al. 2009, *The Astronomical Journal*, 137, 4424
- Tammann, G. A., Loeffler, W., & Schroeder, A. 1994, *The Astrophysical Journal Supplement Series*, 92, 487
- Toomre, A. 1964, *The Astrophysical Journal*, 139, 1217
- Traficante, A., Fuller, G. A., Smith, R., et al. 2015, eprint arXiv:1511.03670
- Truelove, J. K., Klein, R. I., McKee, C. F., et al. 1997, *The Astrophysical Journal*, 489, L179
- van der Kruit, P. C. 1988, *Astronomy and Astrophysics* (ISSN 0004-6361), 192, 117
- van der Tak, F. F. S., & van Dishoeck, E. F. 2000, *Astronomy and Astrophysics*
- Vázquez-Semadeni, E., Ballesteros-Paredes, J., & Klessen, R. S. 2003, *The Astrophysical Journal*, 585, L131
- Vázquez-Semadeni, E., Gomez, G. C., Jappsen, A. K., et al. 2007, *The Astrophysical Journal*, 657, 870
- Vázquez-Semadeni, E., González, R. F., Ballesteros-Paredes, J., Gazol, A., & Kim, J. 2008, *Monthly Notices of the Royal Astronomical Society*, 390, 769
- Vázquez-Semadeni, E., Kim, J., & Ballesteros-Paredes, J. 2005, *The Astrophysical Journal*, 630, L49
- Vázquez-Semadeni, E., Ryu, D., Passot, T., Gonzalez, R. F., & Gazol, A. 2006, *The Astrophysical Journal*, 643, 245

- Vázquez-Semadeni, . 2015, *Astrophysics and Space Science Library*, Vol. 407, *Magnetic Fields in Diffuse Media*, ed. A. Lazarian, E. M. de Gouveia Dal Pino, & C. Melioli (Berlin, Heidelberg: Springer Berlin Heidelberg), doi:10.1007/978-3-662-44625-6
- Von Weizsäcker, C. F. 1951a, *Problems of Cosmical Aerodynamics; Proceedings of a Symposium on the Motion of Gaseous Masses of Cosmical Dimensions held at Paris*
- . 1951b, *Problems of Cosmical Aerodynamics; Proceedings of a Symposium on the Motion of Gaseous Masses of Cosmical Dimensions held at Paris*
- Walch, S., & Naab, T. 2015, *Monthly Notices of the Royal Astronomical Society*, 451, 2757
- Walch, S., Girichidis, P., Naab, T., et al. 2015, *Monthly Notices of the Royal Astronomical Society*, 454, 246
- Walch, S. K., Whitworth, A. P., Bisbas, T., Wünsch, R., & Hubber, D. 2012, *Monthly Notices of the Royal Astronomical Society*, 427, 625
- Williams, J. P., Bergin, E. A., Caselli, P., Myers, P. C., & Plume, R. 1998, *The Astrophysical Journal*, 503, 689
- Wilson, R. W., Jefferts, K. B., & Penzias, A. A. 1970, *The Astrophysical Journal*, 161, L43
- Wolfire, M. G., Hollenbach, D., McKee, C. F., Tielens, A. G. G. M., & Bakes, E. L. O. 1995, *The Astrophysical Journal*, 443, 152
- Wolfire, M. G., McKee, C. F., Hollenbach, D., & Tielens, A. G. G. M. 2003, *The Astrophysical Journal*, 587, 278
- Wu, J., Evans, N. J., Shirley, Y. L., & Knez, C. 2010, *The Astrophysical Journal Supplement Series*, 188, 313
- Yamaguchi, R., Mizuno, N., Mizuno, A., et al. 2001, *Publications of the Astronomical Society of Japan*, 53, 985
- York, D. G. 1974, *The Astrophysical Journal*, 193, L127
- Zamora-Avilés, M., Vázquez-Semadeni, E., & Colín, P. 2012, *The Astrophysical Journal*, 751, 77
- Zinnecker, H., & Yorke, H. W. 2007, *Annual Review of Astronomy and Astrophysics*, 45, 481

Zuckerman, B., & Palmer, P. 1974, Annual Review of Astronomy and Astrophysics, 12, 279

Acknowledgements

This is it, my thesis, and it is finalized. However, it would be foolish to think I did it alone and there is, indeed, a large list of people I have to thank for making this possible. This has been a journey of many hands, hearts and minds over the last three and a half years, and for that I am filled with joy.

First I want to thank my fiancée Laura Aguado and my brother Mauricio Ibáñez-Mejía, whose care and support has been invaluable; you give me the strength and the motivation to work in becoming better day by day. I would like to express my most sincere gratitude to my advisor Mordecai-Mark Mac Low; his guidance, patience and tireless support constantly helped me shape my instinct for research and his input was essential for the outcome of this thesis. I also want to thank my second advisor Ralf Klessen for his great scientific insight and his advice, always working on directing me along the course of this research and never letting me lose sight of the final goal.

I had the fortune to divide my time between two great institutions and interact with amazing people. I want to thank everyone at ITA, specially Anna, Maria, Daniel H., Eric, Christian, Simon, Sebastian, Lukas, Faviola, Rahul, Jenni, Paul, Rowan, Robin, Paola, Daniel R., Daniel C. and Sacha. In my second institution, the American Museum of Natural History, I got the opportunity to live in New York, renew a forgotten passion about dinosaurs and interact with other natural sciences both in research and outreach. Special thanks to Gwen, Dave, Ashley, Or, Jana, Alex, Aaron, Statia, Nathan, Rebecca, Kelle, Jillian and Brian.

This project wouldn't have been the same without the interaction with a great number of colleagues, in particular: Javier Ballesteros-Paredes, Alex Hill, Cara Battersby, Andreas Küpper, Alejandro Nuñez, Jonathan Mackey, Stephanie Walch, Andrea Gatto, Juan-Diego Soler, Jonathan Tan, Joshua Wall, Andrew Emerick, Ralph Pudritz, Jorge Abreu-Vicente and Alex Yep.

Finally I want to thank my friends and family, in particular my parents, Jorge and Cristina, for their care and support over the years. To everyone else who opened their doors to me in my constant migrations between USA and Germany. To Dr. Härtle for fixing my dorsal spine, and to Onix, you've

made this past years a lot more fun.